Quantitative Analysis of the Deposition of Nonvolatile Species on Planar Solid Substrates from Evaporative Thin Films

vorgelegt von
Dipl.-Ing.
José Angel Danglad Flores
ORCID: 0000-0002-5671-6089

von der Fakultät II - Mathematik und Naturwissenschaften
der Technischen Universität Berlin
zur Erlangung des akademischen Grades

Doktor der Naturwissenschaften
-Dr.-rer.nat.-

genehmigte Dissertation

Promotionsausschuss:

Vorsitzender:	Prof. Dr. Karola Rück-Braun
Gutachter:	Dr. Hans Riegler
Gutachter:	Prof. Dr. Michael Gradzielski

Tag der wissenschaftlichen Aussprache: 13. Dezember 2018

Berlin 2019

„Why do you do science? Understanding the nature of the universe gives me peace.“

Anonymous

Technische Universität Berlin

Zusammenfassung

Fakultät II Mathematik und Naturwissenschaften
Institut für Chemie

Dr. nat. rer

Quantitative Analysis of the Deposition of Nonvolatile Species on Planar Solid Substrates from Evaporative Thin Films

von José Angel DANGLAD FLORES

Dünne Schichten aus Flüssigkeiten auf festen Substraten sind allgegenwärtig in der Natur und in vielen technischen Anwendungen. Das Verhalten von Flüssigkeiten während des Aufschleuderns („Spin Casting“) wird untersucht. Diese formen dabei infolge hydrodynamisch - viskoser Kräfte einen planaren, kontinuierlich dünner werdenden Film. Bei flüchtigen Flüssigkeiten nimmt die Filmdicke zusätzlich infolge Verdunstung ab. Anfänglich dominiert dabei der hydrodynamisch-viskose Beitrag. Später bestimmt die Verdunstung die Schichtdickenabnahme. Der Prozess wird mittlerweile quantitativ recht gut verstanden. Dies gilt auch für Fälle von Flüssigkeiten mit einem geringen nichtflüchtigen Anteil. Dieser beschichtet letztlich das Substrat. Für höhere nichtflüchtige Anteile war der Prozess bislang qualitatitiv und quantitativ nicht gut verstanden. Dieser Fall wurde hier untersucht. Dazu wurden Filme direkt in Echtzeit mikroskop-optisch während der Dickenabnahme abgebildet. Dies ergab neue Einblicke in das Verdunstungs/Trocknungs-Verhalten während des ganzen Prozesses in Abhängigkeit von der Konzentration und Art der nichtflüchtigen Komponenten. Erstmals kann damit nun die finale Beschichtung mit diversen nichtflüchtigen Komponenten, wie Polymeren oder (Nano-)Partikeln quantitativ vorhergesagt werden. Die Partikel-Ablagerung wurde bezüglich des Beitrags von Sedimendation genauer analysiert. Erstmals wurde auch die Verformung der Filmoberfläche (Meniskus) durch partiell herausragende Nanopartikel gemessen und analysiert. Weiterhin wurde gezeigt, wie Nanopartikel mit Hilfe kapillar-induzierter Anreicherung von nichtflüchtigen Adsorbaten im ringförmigen Hohlraum zwischen.

Technische Universität Berlin

Abstract

Fakultät II Mathematik und Naturwissenschaften
Institut für Chemie

Dr. nat. rer

Quantitative Analysis of the Deposition of Nonvolatile Species on Planar Solid Substrates from Evaporative Thin Films

by José Angel DANGLAD FLORES

Thin layers of liquids on solid substrates are ubiquitous in nature and in many technical applications. The behaviour of liquids during spin casting is investigated. As a result of hydrodynamic - viscous forces, these form a planar film that continuously becomes thinner. With volatile liquids, the film thickness also decreases as a result of evaporation. Initially, the hydrodynamic-viscosity contribution dominates. Later, evaporation determines the film thinning. The process is now well understood in quantitative terms. This also applies to liquids with a low content of non-volatile species. These ultimately coats the substrate. For higher concentrations of non-volatile compound the process was not well understood qualitatively and quantitatively. This case was investigated here. For this purpose,the film thinning was measured and imaged online by interferometry and optical microscopy. This provided new insights into the evaporation/drying behavior during the entire process depending on the concentration and type of non-volatile components. The final coating with various non-volatile species such as polymers or (nano)particles can now be quantitatively predicted. The particle deposition has been analysed in more detail with regard to the contribution of sedimentation. For the first time, the deformation of the film surface (meniscus) by partially protruding nanoparticles was measured and analyzed. Furthermore, it was shown how nanoparticles can be enriched by capillary-induced enrichment of non-volatile adsorbates in the ring-shaped cavity between the film surface (meniscus) and the film surface (meniscus).

Acknowledgements

Thanks to:

God for everything.

Venezuela and Germany for sponsor my education.

My mother, father and brother for their love and believe on me.

Prof. Shirley Marfisi my first mentor, and Prof. Alexis Cova my dear friend, you helped me to get here. Prof. Regine von Klitzing and Dr. Klaus Tauer for giving me the opportunity to start my doctoral studies.

The IRTG 1524 for the institutional and organizational framework, sponsored by the DFG and DAAD.

Thanks to Hans Riegler my mentor, father and brother. And all those people who listen to me complain about you.

My Venezuelan sisters Maylen, Zulivis and Zorimar; no matter the time or distance, you are always there for me.

My family in Germany. Melis for honestly shows me when I am wrong. Sonja for rescuing me on that train platform. Eddie for caring about me.

Marie Jehannin for opening the door to the heart of her family (now my family too).

Sthepan Eickelmann, even though, we have different personal opinions, in science we make a good team.

Sasha Alexandra, I find in your trust a source of comforting strength.

Tom, Eleonor and Eliot, my friends, the best British people I know.

Agnese Codutti, Afroditi Doriti, and Justin Ryan for helping with the prove reading and being such great friends.

Guoxiang Chen, Karaneh Eftekhari, Xiao Cheng and Jason Miles for the productive collaboration.

Last but no least, "Gente Bien" my friends from High School, you are always with me.

Contents

Zusammenfassung **v**

Abstract **vii**

Acknowledgements **ix**

1 Introduction **1**

2 Theoretical Background **3**
- 2.1 Interfacial energies . . . 3
- 2.2 Thin films . . . 3
  - 2.2.1 Van der Waals and disjoining pressure . . . 3
  - 2.2.2 Laplace pressure and capillary length . . . 4
    - Laplace pressure . . . 4
    - Capillary length . . . 5
    - Distorted film . . . 5
- 2.3 Evaporation rate . . . 6
  - 2.3.1 Spin casting . . . 7
    - Spin casting of a pure liquid - zero order approach . . . 8
    - Spin casting of a dilute solution - zero order approach . . . 9
  - 2.3.2 Spin casting concentration profile . . . 10
- 2.4 Interference-enhanced imaging of ultra-thin films . . . 10

3 Materials and Methods **13**
- 3.1 Material and sample preparation . . . 13
  - 3.1.1 Polymers . . . 13
  - 3.1.2 Chemicals . . . 13
  - 3.1.3 Particles . . . 13
  - 3.1.4 Substrates and substrate preparation . . . 14
- 3.2 Experiment methods and equipment . . . 14
  - 3.2.1 Static evaporation rate . . . 14
  - 3.2.2 Spin casting . . . 14
  - 3.2.3 Optical on-line observation of the film thinning . . . 14
    - Height reconstruction by interference pattern . . . 15
    - Height reconstruction from the gray variation . . . 16
  - 3.2.4 Rheology . . . 16
  - 3.2.5 Ellipsometry . . . 17
  - 3.2.6 Measurement of final particles coverage . . . 17
  - 3.2.7 AFM image and nano-manipulation . . . 17
- 3.3 Analytic expression and numerical approximations . . . 17
  - 3.3.1 Numerical Analysis of the Meniscus Profile . . . 17

4 Evaporation of a Pure Liquid Thin Film in a Spin Cast Configuration 19
4.1 Introduction 19
4.2 Results 20
4.2.1 Evaporation from a planar liquid surface under static conditions . . . 20
4.2.2 Evaporation of liquid films in a rotating plate 20
4.3 Discussion 24

5 Deposition of Molecules from an Evaporative Thin Film 27
5.1 Introduction 27
5.2 Results 28
5.2.1 Evaporative process 31
5.2.2 Initial hydrodynamic influence 33
5.2.3 General deposition theory from evaporative films 34
5.3 Discussion 36
5.4 Summary and Conclusion 38

6 Deposition of Particles from an Evaporative Thin Film 39
6.1 Introduction 39
6.2 Results 40
6.2.1 Particle coverages 40
6.2.2 Particle coverages as function of concentrations and sizes 42
6.2.3 Universal plot of Γ as function of the particle sizes 42
6.3 Discussion 42
6.3.1 Limits of the zero-order approach: Rheology 42
6.3.2 Limits of the zero-order approach: Sedimentation 46
6.4 Summary and Conclusion 49

7 Liquid Thin Film Shape Around Nanoparticles 51
7.1 Introduction 51
7.2 Results 54
7.2.1 Optical footprints of NPs and their menisci in liquid films 54
7.2.2 Optical footprints as a function of the far-field film thickness for different liquids 55
7.2.3 Meniscus profiles derived from the local gray levels 57
7.2.4 NPs embedded in solid polymer films 58
7.2.5 Meniscus geometries 60
Surface Shape 60
Contact to the particle 61
7.2.6 Universal meniscus profile and distortion length L 62

8 Capillary-Enhanced Immobilization of Nanoparticles 65
8.1 Introduction 65
8.2 Results 66
8.2.1 Enhanced adhesion 67
8.2.2 Capillary condensation underneath of nano-particle 68
8.3 Discussion 70
8.4 Summary and Conclusion 72

9 Summary and Conclusions 73

10 Outlook and On Going Work **75**
10.1 What is the minimum volume needed to create a film? 75
10.2 Thin Films with Lateral Surface Tension Gradients 76

A Chemical and Physical Properties **79**
A.1 Liquid Physicochemical Properties 79

B Final deposit **81**

C Analytics and Calculations **85**
C.1 Reflective Value according to Fresnel Equations 85

D Reprinting license **87**

Bibliography **89**

Declaration of Authorship **101**

List of Figures

2.1 Disjoning pressure 4
2.2 Meniscus geometry 5
2.3 Mass transport from planar films 6
2.4 Spin casting process 7
2.5 Film height evolution 9
2.6 Concentration profile 11
2.7 Interference enhanced optical reflection 11

3.1 Spin casting setup 15
3.2 Interferogram 16

4.1 Pure solvent evaporation 19
4.2 Static evaporation 21
4.3 Thinning curve of typical solvents 22
4.4 Evaporation rate as function of ω 23
4.5 Approximation of the reduce evaporation rate e 24

5.1 Deposition of polymers 27
5.2 Final film thicknesses as function of x_0 29
5.3 Thinning curve of polymer solutions 30
5.4 Thinning curves first derivate as function of the time 31
5.5 Evaporation rates E as function of x 32
5.6 Hydrodynamic parameter as as function of x_0 33
5.7 Time evolution of the polymer concentration x 34
5.8 Universal plot of final film polymer thicknesses 35

6.1 Deposition of particles 39
6.2 Particles as deposited 41
6.3 Final particle coverage Γ 43
6.4 Rescaled particle coverage in terms of R^3 44
6.5 Particles during the film thinning 45
6.6 Threshold for the particle deposition prediction 48

7.1 Meniscus distortion 51
7.2 Snapshots of particle optical footprints 54
7.3 Region of particle visualization 55
7.4 Translation of optical data into meniscus geometries 57
7.5 Optical versus the AFM particle signatures 59
7.6 Resolved experimental meniscus geometry 60
7.7 Universal plot for meniscus geometry 62
7.8 Distortion length L versus NP radius R 63

8.1 Capillary-enhanced Immobilization 65
8.2 Nanoparticles Immobilization 67

8.3 Particle immobilization test 69
8.4 Particles molecular footprint 70
8.5 Meniscus footprint 71

10.1 Film topography of binary solvent mixtures 77
10.2 Stabilization/destabilization of evaporative thinning films 77

B.1 Platinum Nanoparticles 81
B.2 Deposit at the center and edges 82
B.3 $CaCO_3$ particle distribution 83
B.4 Immobilization of Au nanoparticles 83

D.1 Reprinting license Karpitschka et al. 2015 87
D.2 Reprinting license Köhler et al. 2006 88

List of Tables

4.1 Experimental and predicted $e = f(\omega)$ 25
A.1 Solvent physicochemical properties 79

Dedicated to my parents Pequi and Rene…

Chapter 1

Introduction

Evaporative liquid thin films are recurrent in nature. The reader might be aware of the preocular tear film covering her/his eyes. Every time the eye blinks the film is recovered, in part to compensate the evaporative loss [1–3]. The mucous membrane in the lungs clears the alveoli walls and prevents the cells from drying [4]. The number of relevant examples in nature is surprising, considering the energetic cost of creating interfacial area [5]. Apparently, the natural advantages of liquid films pay off, e.g., the transport properties are homogeneous over relatively large areas (this is a significant difference to the droplet case [6, 7]). Fick's law predicts a more efficient diffusive transport through the film; when the film becomes thinner [8]. Therefore, the rapid communication through the film is translated as a quick response to physical stimuli such as: compressions[9, 10], extension [11], confinement [12], disruption [13, 14], etc.

In applications, the deposition of nonvolatile species (monomers, polymers, and particles) from films of mixtures of volatile solvents and nonvolatile compounds is widely used as coating technique. From painting walls [15, 16] to bottom-up microchip construction [17–23]; thin evaporative films bridge the nano-scale and meso-scale technologies.

Ultra thin films are extensively produced from evaporative films via *spin casting* [24–28]. From a *zero-order* approximation, this process could be described in two separate regimes [29]. At first, a hydrodynamic thinning allows to form a homogeneous flat thin film (i.e. due to the outward flow) [30]. With the decreasing of the film thickness, the shear flow slows down rapidly. Then, a purely evaporative solvent loss controls the final film thinning and solute enrichment [29, 31–33]. Recently the experimental techniques have been improved significantly, enabling to observe (surface film topography) and record dynamic data (time resolved film thinning) [34–39] during the hydrodynamic-evaporative thinning of the liquid film [40, 41].

Understanding and providing a general description of the deposition process via spin casting is crucial in terms of, a) a transparent and accessible approach, b) well described basic physical properties of the compound and the system parameters, d) and topological scenarios (such as planar, smooth and structured substrates). The aim of this work is to provide theoretical tools to predict the final deposition from a spin cast configuration, by understanding the process of hydrodynamic-evaporative film thinning.

Here, the available theoretical descriptions will be reviewed and tested from the perspective of the new experimental insights. The study will be based on the following hypothesis:

If the hydrodynamic-evaporative thinning of a liquid film could be described in term of the system parameters. Therefore the outcome deposit from films loaded with nonvolatile species could be predicted based on such system parameters.

The deposition of nonvolatile species on planar, smooth and structured substrates from an evaporative thin film will be analyzed. Also, relevant mass and momentum transport phenomena within thin liquid films will be investigated. The work structure is as followed:

- **Chapter 1** offers an introduction to the topic and the scientific motivation.

- **Chapter 2** presents basic concepts of thin film hydrodynamic and physico-chemistry.
- **Chapter 3** describes in detail the material and methods used for the experimental and theoretical investigation of the systems.
- **Chapter 4** presents the most simple case, the evaporation of pure solvent thin film. The solvent molecular transport from a planar liquid film to the vapor phase is examined for the static and the rotating substrate scenario. The theoretical expression to calculate the evaporation rate is experimentally tested.
- **Chapter 5** discloses the question; does a solutions behave as a pure solvent? Mixtures of nonvolatile molecules (polymers) and evaporative solvents are studied, the spatio-temporal film dynamic is analyzed. A *zero-order* approximation (solvent like) to estimate the final deposit is evaluated. A first order correction is developed. Moreover, is the molecular description extensible to particle in dispersion?
- **Chapter 6** introduces a complete new description of the particles deposition from dispersion of particles in a volatile liquid. Thus, a general formula is provided to estimated the coverage for particles up to nano/micrometer size.
- **Chapter 7** analyzes the distortion of the liquid-vapor interface by the embedded nanoparticles. Shape and length of the menisci in proximity of to the particle are resolved analytically.
- **Chapter 8** explores a new nanoparticle immobilization method. The annular cavity between the spherical particles and the plane is found to be preferential for the deposition of molecules. The enhanced immobilization of the particle is explained in terms of the capillary condensation effect.
- **Chapter 9** summarizes and concludes on the main results.
- **Chapter 10** briefly presents the open questions and the current studies addressing them.

Chapter 2

Theoretical Background

In the following Chapter from a reviewing of the literature, some basic prerequisites are presented.

2.1 Interfacial energies

If one visualizes a unit (an atom or molecule) of a substance in a bulk phase, it can be seen that, on average, the unit experiences a uniform force field due to its interaction with neighboring units. The unit will "feel"the presence of the adjacent units in the adjoining bulk phase. If the bulk phase is cleaved along a plane that just touches the unit in question will be in a different energetic environment relative to its nearest neighbors. Therefore its total free energy must change. In this case, since the interactions in the bulk phase produce a net lowering of the free energy of the units, the removal of those interactions by the formation of new surface results in an increase in the free energy of the units at or near the interface [42]. The *additional* energy is called the surface free energy or more accurately the excess surface free energy [43]. The result will be a state of lateral tension along the surface, giving rise to the concept of *surface tension*. The specific thermodynamic definition of surface tension is given by [42]:

$$\Delta H = \Delta W = 2\gamma A. \tag{2.1}$$

Where H is the Helmholtz free energy of the system, W is the amount of reversible work necessary to overcome the attractive forces between the units at the new surface, and A is the area of new surface formed. Then, the proportionality constant γ termed the *surface tension*, is numerically equal to the specific excess surface free energy for pure liquids at equilibrium.

2.2 Thin films

A liquid thin film is a layer ranging from fractions of a nanometer (monolayer) to several micrometers in thickness. It falls into the lubrication theory, which describes the flow of fluids in a geometry in which one dimension (the thickness for this case) is significantly smaller than the others. For ultra thin films (thickness $\leq 200\,\mathrm{nm}$), additional intermolecular forces, such as Van der Waals forces or disjoining forces, may become significant.

2.2.1 Van der Waals and disjoining pressure

The cartoon in Figure 2.1 depicts a thin liquid film that is intervening between a solid and a vapor phase. The liquid/vapor interfaces (surface) with surface tension γ_{LV} is separated from the solid/liquid interfaces (with interfacial tension γ_{SL}) by the film thickness h. In such a case, the free energy of the system is described in terms of h and the free energy W per unit of iterfacial area A is [44]:

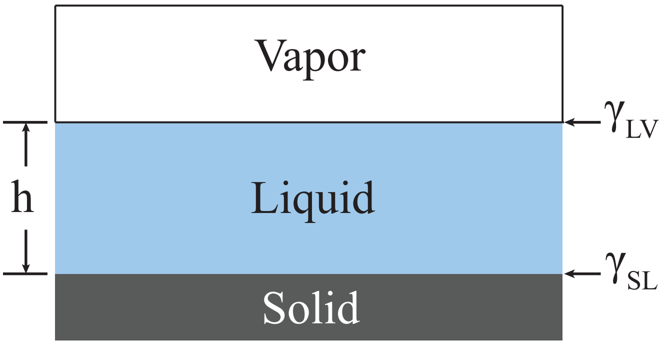

FIGURE 2.1: A liquid film between a solid and a vapor phase. The liquid/vapor interfaces (surface) with surface tension γ_{LV} is separated from the solid/liquid interfaces (with interfacial tension γ_{SL}) by the film thickness h.

$$\frac{W}{A} = \gamma_{SL} + \gamma_{LV} + P(h) = \Delta\gamma + P(h). \tag{2.2}$$

$P(h)$ arises from the molecular interactions, like van der Waals, electrostatic, ionic, and/or metallic interactions [45]. $P(h)$ becomes more important as the film thickness h approaches the length scales of the respective interactions.

The disjoining pressure Π results from the overlap of the molecular interactions from both L/V and SL interfaces [46].

$$\Pi(h) = -\frac{dP(h)}{dh}. \tag{2.3}$$

This pressure may have either positive or negative values. If the disjoining pressure is positive, thin film is stable and it will not de-wet. If the disjoining pressure is negative, the system becomes unstable, and de-wetting can occur for a thin film. Van der Waals interactions between the two interfaces are described with the Hamaker coefficient A_{ij}. For films that satisfy $A_{ij} > 0$, $\Pi(h)$ becomes larger as the film thickness goes smaller [47, 48],

$$P(h) = -\frac{A_{ij}}{12\pi h^2}. \tag{2.4}$$

2.2.2 Laplace pressure and capillary length

Laplace pressure

In addition to the static pressure, the surface tension creates an extra pressure in the case of a curved interface (e.g. the interior of drops and bubbles). This is the so called *Laplace Pressure*. For a spherical droplet under an external pressure p_{out} and an inner pressure p_{in}, the following term is obtained for the pressure difference:

$$\Delta p = p_{in} - p_{out} = \frac{2\gamma}{R}, \tag{2.5}$$

where R is the radius of the droplet. The increase in the hydrostatic pressure Δp that occurs upon traversing the boundary between two fluids is equal to the product of the surface tension γ and the curvature of the surface (with curvatures R_1 and R_2). The general expression is given by [49]:

$$\Delta p = \gamma \left(\frac{1}{R_1} + \frac{1}{R_2} \right), \tag{2.6}$$

Capillary length

To define the scale where gravitational forces becomes significant, a length κ^{-1} is defined by comparing the *Laplace Pressure* and the *Hydrostatic Pressure*. This length is called *Capillary length* [49].

$$\kappa^{-1} = \sqrt{\frac{\gamma_{LV}}{\rho_L \cdot \mathrm{g}}}; \tag{2.7}$$

where g is gravity constant, ρ_L the density of the liquid and γ_{LV} its liquid/vapor surface tension. E.g. for water with $\gamma_{LV} = 72.8\,\mathrm{mN}$ at $293.15\,\mathrm{K}$ [50], $\kappa^{-1} \simeq 2.7$ mm.

Distorted film

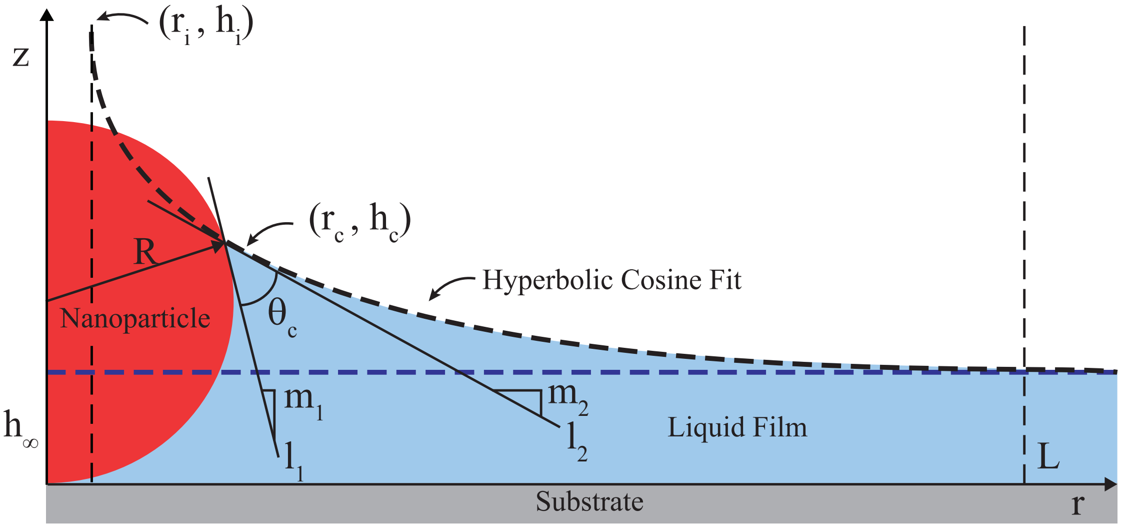

FIGURE 2.2: Theoretically assumed meniscus geometry and boundary conditions used to fit the experimentally measured liquid profiles. Assuming a perfectly spherical nanoparticle (NP) with a radius $R = d_{\mathrm{NP}}/2$ attached to the substrate at $z = 0$ and embedded in a liquid film of a given (measured by interferometry) far-field thickness, h_∞. The meniscus adopts a minimal surface shape close to the NP. The meniscus contacts the NP at a circle at height relative to the substrate surface of $z = h_c$ and a distance from the z-axis of $r = r_c$. The contact angle of the liquid with the NP surface is Θ_c. The minimal surface profile with these specifications is equivalent to the liquid profile contacting a vertical round cylinder (e.g. a fiber) of radius $r = r_i$ at a height $z = h_i$ with Θ_c = 0.

Figure 2.2 shows the theoretically assumed meniscus profile, parameters and boundary conditions that will be used in Chapter 7 to fit the experimentally measured liquid-vapor interface profiles next to a nanoparticle (NP) of radius R. This nanoparticle is attached to the substrate and embedded in the liquid film. The film has a given (interferometrically measured) far-field thickness, h_∞. Near to the particle, it is assumed that the meniscus has a hyperbolic cosine profile [**degennes2004**]. It is assumed further that the meniscus contacts the NP at a circle at height relative to the substrate surface of $z = h_c$ and a distance from the z-axis of $r = r_c$. The contact angle of the liquid with the NP surface is Θ_c. At a distance of $r = L$ from the z-axis the hyperbolic cosine curve reaches the liquid film surface plane. The angle of intersection of distance L between the meniscus and the h_∞ and the is rather small (with $L < \infty$ it cannot be zero). Hyperbolic cosine curves with these specifications are equivalent to meniscus profiles, which contact a vertical round cylinder (e.g. a fiber) of radius $r = r_i$ at a height $z = h_i$ with $\Theta_c = 0$. As it was described just above, if the hydrostatic force is significant, basically L should be equal to κ^{-1} (zero order approximation).

2.3 Evaporation rate

The sketch of Figure 2.3 describes the mass transport scenario during the evaporative regimen in the case of a solid, planar rotating plate; the two characteristic lengths of the system are the film thickness h and the radial distance L_{plate} [51]. For a purely evaporative film thinning, the liquid mass flux j_L (given as massive flow per unit area) of the volatile compound i.e. the *evaporative thinning*, is equal to the vapor mass flux j_V [52].

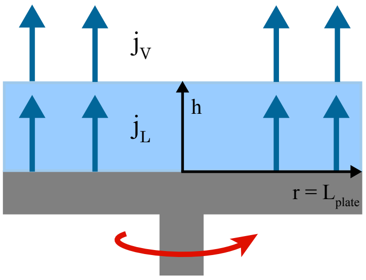

FIGURE 2.3: Mass transport scenario during the evaporative regime. The liquid mass flux j_L of the volatile compound (i.e. evaporating thinning) should be equal to the vapor mass flux j_V.

Under this premise Bornside, Macosko, and Scriven BMS derive E as[53]

$$\rho_L E = k \rho_V (x_a - x_{a\infty}). \tag{2.8}$$

Where ρ_L is the solvent liquid density, ρ_V is the vapor phase density and k is the mass transfer coefficient in the gas phase. x_a and $x_{a\infty}$ are the solvent mass fraction in the liquid and faraway in the vapor phase [1] respectively. Assuming Raoult's law to describe the vapour-liquid equilibrium of the solvent and the ideal gas law to estimate its density [53, 54], Eq. 2.8 is rearranged as,

$$E = k \left(\frac{P^* M_a (x_a - x_{a\infty})}{\rho_L R_g T} \right), \tag{2.9}$$

where P^* is the vapour pressure of the pure solvent and M_a is its molecular weight; R_g is the ideal gas constant and T is the temperature, which is assumed constant for both phases

---

[1] In most of the cases the term $x_{a\infty}$ is considered equal to zero, especially for organic solvents. But with water as solvent, the humidity of the environment should be taken into account, also in the case of controlled vapour atmospheres.

during the process.

A laminar flow with an uniform mass transport coefficient is theoretically predicted towards the surfaces of the rotating plane [55]. For such a condition the Sherwood number of the vapor phase above the liquid film Sh$_V$ is given in terms of the rotational Reynolds number $Re = \omega L_{plate}^2/\nu_b$ [51], where ω is the rotational speed of the solid plane and ν_b is the air kinematic viscosity at normal conditions.

$$Sh_V = \sigma Re^{1/2} = k\left(\frac{L_{plate}}{D_{ab}}\right), \tag{2.10}$$

were L_{plate} is the characteristic length (the plate radio), D_{ab} is the diffusion coefficient of the solvent (a) in air (b), and the constant σ is a function of the Schmidt number given by Ref. [51] as Sc$= \nu_b/D_{ab}$; $\sigma = 0.386 \cdot \text{Sc}^{0.462}$ (ν_b is the air kinematic viscosity). From Eq.2.10 one obtains k as;

$$k = \sigma D_{ab}\left(\frac{\omega}{\nu_b}\right)^{1/2}. \tag{2.11}$$

Combining Eq. 2.9 and Eq. 2.11, an expression for E is given by [54, 56]:

$$E = \left(\frac{\sigma(x_a - x_{a\infty})}{R_g T \nu_b^{1/2}}\right)\left(\frac{P^* M_a D_{ab}}{\rho_L}\right)\omega^{1/2}. \tag{2.12}$$

Eq. 2.12 describes E in terms of a) a constant factor given by the properties of the surrounding atmosphere; b) a second factor given by the solvent properties and c) as function of the square root of the ω.

2.3.1 Spin casting

Spin casting (spin coating) is a widely used technique to deposit films of uniform thickness on planar solid substrates [24, 57, 58]. In this process, a liquid that could be a melts or a solution is deposited on a rotating substrate. As Figure 2.4 depicts, after the liquid is dropped on a rotating plate, it is flattened by a combination of wetting, spreading and centripetal forces. After the film is formed, its thinning will be dominated initially by hydrodynamics.

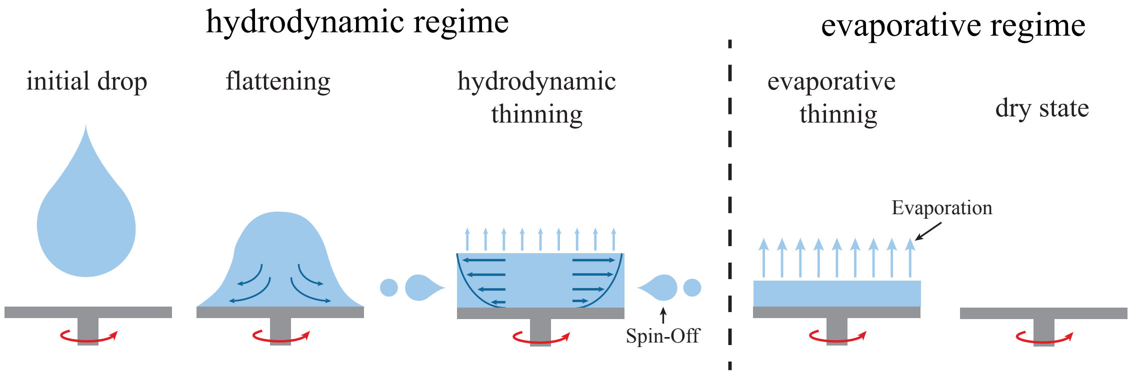

FIGURE 2.4: Schematic of the spin cast process for a completely evaporating liquid.

With on-going rotation this planar film will continuously become thinner [30, 59] (due to the liquid spin-off, Figure 2.4). If the liquid consists of a nonvolatile solute and a volatile solvent, film thinning also occurs due to solvent evaporation in addition to the hydrodynamic thinning. At the last stage (Figure 2.4), evaporation will dominate the film thinning process. Hence, spin casting of volatile liquids can be considered as a sequence of hydrodynamic planar film formation and thinning followed by evaporative thinning/drying of this film [31, 56, 60–69]. If the liquid consists of a mixture of a nonvolatile solute and a volatile solvent, the solvent evaporation causes a continuous enrichment of the nonvolatile solution components. In the end, the solute will be deposited as a dry film.

Spin casting of a pure liquid - zero order approach

The thinning of a Newtonian, volatile liquid film of thickness h on a rotating support was described by [31]:

$$dh/dt = -2K\,h^3 - E\,. \tag{2.13}$$

Eq. 2.13 assumes no slip at the liquid/substrate interface (lubrication approximation) and a free liquid surface. The film thinning due to contributions from surface tension and gravity is neglected [29–31]. E is the evaporation rate. The parameter,

$$K = \omega^2/(3\nu), \tag{2.14}$$

describes the hydrodynamic behavior (ω = rotational speed, ν = kinematic viscosity). The parameters characterizing the process according to Eq. 2.13 are K and E. For the case of a pure liquid, Kapitschka et al. [29] solved Eq. 2.13 by a change of variables.

$$\frac{d\xi}{d\tau} = -\xi^3 - 1, \tag{2.15}$$

which is obtained by rescaling, with $\xi = h/h_{tr}$ and $\tau = t/t^*_{sc}$, where:

$$h_{tr} = (E/2K)^{1/3}, \tag{2.16}$$

$$t^*_{sc} = (2E^2K)^{-1/3}, \tag{2.17}$$

are the natural scales. h_{tr} is the transition height, at this film height the film fluid evaporation and hydrodynamic thinning are equal. Below the h_{tr} the film thinning is dominated by the volatile component evaporation.

t^*_{sc} represents the *reduced* process duration, it is the absolute time from h_{tr} to $h = 0$. This leads to an ordinary linear differential equation, whose solution $\tau(\xi)$ is [29]:

$$\tau(\xi) = \frac{\sqrt{3}}{6}\left\{\pi + 2\arctan\frac{1-2\xi}{\sqrt{3}} + \frac{1}{\sqrt{3}}\log\frac{1-\xi-\xi^2}{(1+\xi)^2}\right\}. \tag{2.18}$$

t_{sc} is the duration of the process (starting at $h \to \infty$, ending $h = 0$). It is found that hydrodynamic film thinning dominates always 30% of the spin cast time in the beginning and then 70% of the film thinning is driven by evaporation. In this zero-order approximation, t_{sc} is the total spin cast time (film thinning from $h \to \infty$ to $h = 0$) [29]:

$$t_{sc} = \frac{2\pi}{3^{3/2}}(2E^2K)^{-1/3} = \frac{2\pi}{3^{3/2}} \cdot t^*_{sc} \tag{2.19}$$

In general terms, the thinning process of pure liquid by spin casting is described by: a) the parameters E and K, b) the scales h_{tr} and t_{sc}. In the *zero order* approach such parameters are assumed constant during the whole process, and they given by the pure solvent-systems properties.

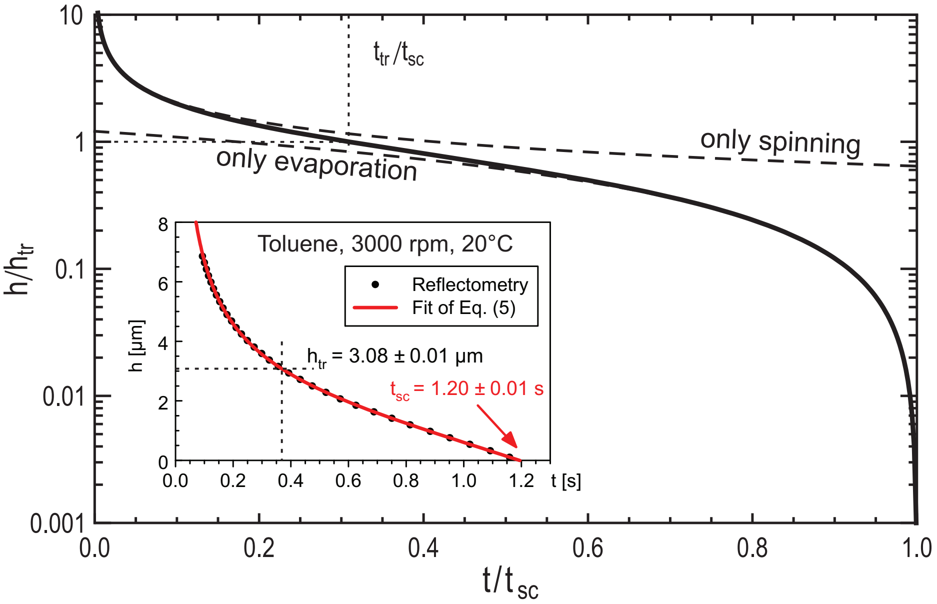

FIGURE 2.5: The solid line indicates the fit of equation 2.18. It shows the universal thinning behavior. The inset presents typical thinning data for toluene at $\omega = 3000\,\mathrm{rpm}$; such plot could be rescaled with the transition height h_{tr} and process time t_{sc}; the result is the main of Figure. Adapted from Chem. Eng. Sci., 129., S. Karpitschka, C. M. Weber, and H Riegler, Spin casting of dilute solutions: Vertical composition profile during hydrodynamic-evaporative film thinning, 243-248., Copyright (2015), with permission from Elsevier. Ref. [29].

Spin casting of a dilute solution - zero order approach

At film thicknesses below h_{tr}, the film thinning due to evaporation. Therefore, most of the solute, which is contained in the film of thickness h_{tr} is finally deposited on the substrate (with a solute concentration approximately equal to the weighing in concentration c_0), the coverage Γ expressed in number of molecules N deposited per area A, is (Eq. 2.20):

$$\Gamma = \frac{N(h \to 0)}{A} \approx c_0 \cdot h_{tr}, \tag{2.20}$$

Γ is analogous to the final film thins of the solute h_f (typical mean in the case of polymer deposition). The translation in the total volume from the h_{tr} to the dry film is proportional to the solute volume fraction; because the area is constant, this proportionality can be translated to the film height. It is practical in most of the cases to assume that the volume fraction is equal to the mass fraction (x_0) when the solution and the solute density are approximately the same $\rho_L \approx \rho_S$. According to Meyerhofer [31]:

$$h_f = x_0\,\frac{\rho_L}{\rho_S} h_{tr} = x_0 \left(\frac{3E\nu}{2\omega^2}\right)^{1/3} \approx 0.8\, x_0\, (K/E)^{-\frac{1}{3}}. \tag{2.21}$$

The *zero-order* approach [29] takes the assumptions from the pure liquid description mentioned above and neglects the presence of the nonvolatile component. For initially low concentrations, it is presumed that K and E are basically solvent like. Thus, the parameters at Eq.2.21 are the pure solvent ones.

2.3.2 Spin casting concentration profile

The nonvolatile solute might be enriched on the vapor/liquid interface due to evaporation of the volatile compound. This could lead to a vertical concentration profile [70, 71] through the film. Nevertheless, a gradient in the nonvolatile compounds will drive the diffusive transport of the molecules through the film. The spatio-temporal evolution of the solute concentration c is described by [29]:

$$\partial_t c = \frac{d\tau}{dt} \cdot \frac{d\xi}{d\tau} \cdot \partial_\xi c = -(2E^2K)^{1/3}(\xi^3 + 1)\partial_\xi c \tag{2.22}$$

In order to avoid the moving boundary, the system is rescaled (between substrate and surface) with $y = z/h \in [0, 1]$. This leads to:

$$\partial_\xi c = -\frac{\partial_y^2 c}{Sh_{tr}\xi^2(\xi^3 + 1)} - \{\frac{(\xi y)^2(3 - y)}{2(\xi^3 + 1) - \frac{y}{\xi}}\}\partial_y c, \tag{2.23}$$

$$\partial_y c|_{y=1} = Sh_{tr}\xi c|_{y=1}, \partial_y c|_{y=0} = 0, \tag{2.24}$$

where the Sherwood number Sh_{tr} at $h = h_{tr}$ parameterizes in the liquid film the ratio of evaporation to diffusive mass transport at the characteristic length scale of the system, the transition height.

$$Sh_{tr} = (E \cdot h_{tr})D^{-1} = E^{4/3}(2K)^{-1/3}D^{-1} \tag{2.25}$$

By scaling c with the initial solute concentration c_0, the initial condition is $c|_{\xi \to \infty} = 1$, and the system is parameterized completely by Sh_{tr}. With ξ as independent variable, equation 2.23 can be solved numerically. Together with equation 2.18, it provides τ as function of ξ, thus finally providing $c(t, z)$.

The Sherwood number Sh_{tr} reveals the competition between solute enrichment due to evaporation, solvent/solute loss due to spin-off, and diffusive dilution. In general, larger Sh_{tr} means a larger gradient in the concentration c.

Figure 2.6 A shows that, if $h >> h_{tr}$ (hydrodynamic stage), the solute enrichment occurs only locally near the free surface and $c = c_0$ near to the substrate. If $h << h_{tr}$ (evaporative stage), c also increases near the substrate. $Sh_{tr} = 1$ and $h = h_{tr}$ mark the transitions. The Figure 2.6B upper illustrates the scenario of $Sh_{tr} \gg 1$, where the local concentration at the surfaces leads a marked c profile. For $Sh_{tr} << 1$ (lower Figure 2.6B) diffusion dominates and c close to the substrate and the surface are mostly the same (Figure 2.6 A). The final solute coverage/film thickness for $Sh_{tr} < 1$ is given by Eq 2.21/ 2.20.

2.4 Interference-enhanced imaging of ultra-thin films

Using an auxiliary layer thickness the interference contrast between film sections of different heights is maximize [41]. The design is particularly well suited for the imaging of the topology of films deposited on silicon wafers with artificially grown SiO_2. An appropriate substrate with h_{off} will shift the interference pattern by a fourth period length to the range of maximum contrast-change. The silicon-oxide layer has almost the same optical properties as an organic solvent films like toluene. The thickness of this oxide layer can be used to achieve an optimum "h_{off}". The physics of the system has been in detail describe by Köhler[72] and Jin [73] as follows.

In the system of a silicon/silica substrate and a film on top (illustrated in Figure 2.7 A), the reflections from the various interfaces are:

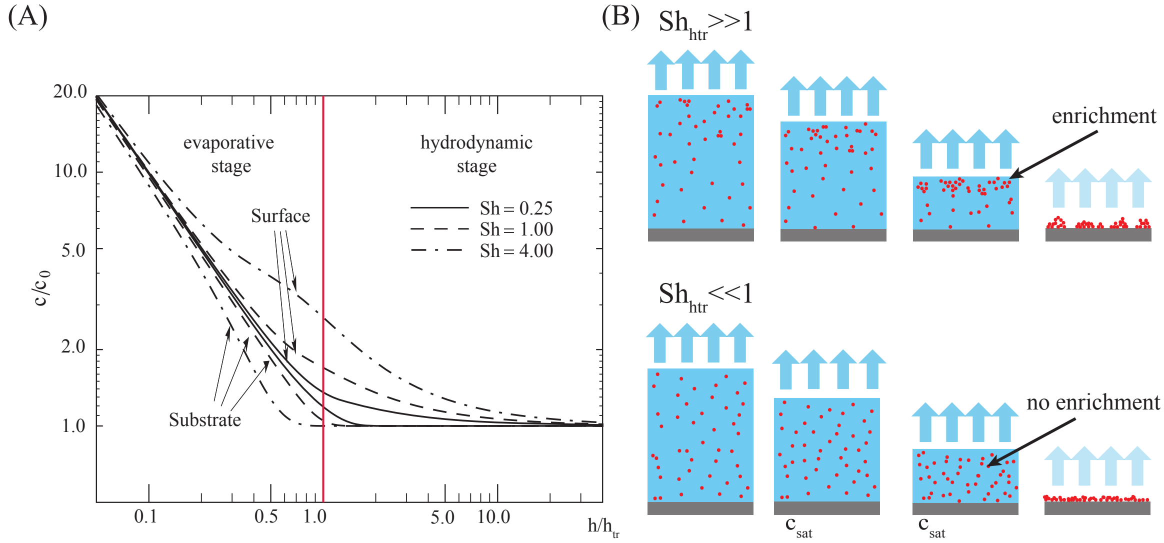

FIGURE 2.6: (A) concentrations c at the surface respectively film/substrate interface (scaled by c_0) Adapted from Chem. Eng. Sci., 129., S. Karpitschka, C. M. Weber, and H Riegler, Spin casting of dilute solutions: Vertical composition profile during hydrodynamic-evaporative film thinning, 243-248., Copyright (2015), with permission from Elsevier. Ref. [29]. (B) The influence of diffusion speed on the solute distribution inside a thinning film.

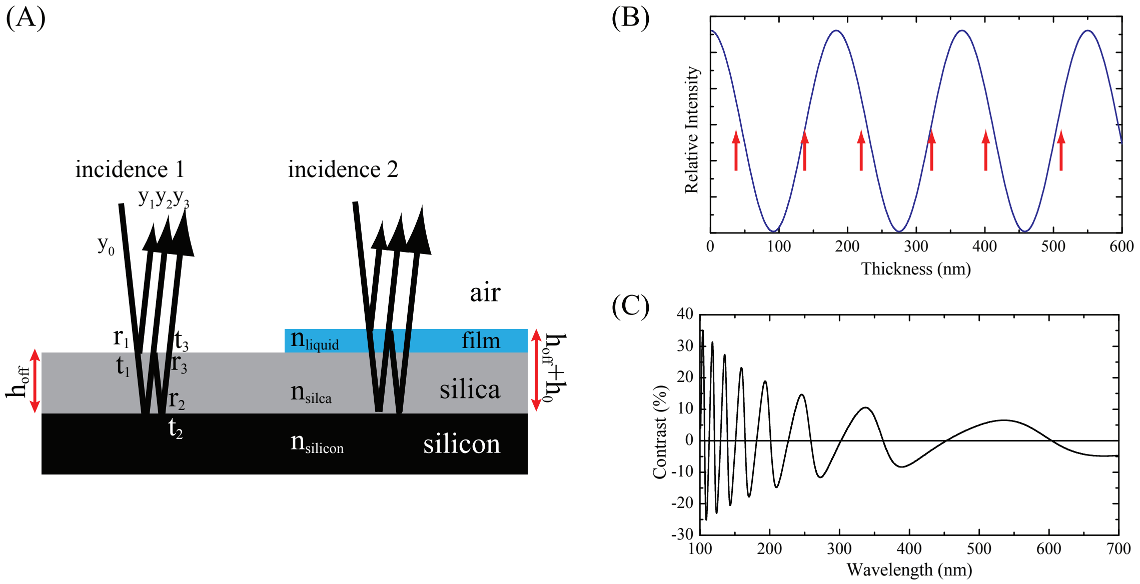

FIGURE 2.7: (A) Reflection from various surfaces. (B) Relative intensity depending on film thickness. (C) Contrast enhancement depending on illumination wavelength. Adapted from Appl. Phys. Lett., 89(24).,R. Köhler, P. Lazar, and H. Riegler, Optical imaging of thin films with molecular depth resolution, 241906., Copyright (2006), with permission from AIP Publishing. Ref. [72]

$$\Psi_1 = r_1\Psi_0 e^{i\pi}, \Psi_2 = t_1 r_2 t_3 \Psi_0 e^{i\varphi}, \Psi_3 = t_1 r_2 r_3 r_2 t_3 \Psi_0 e^{2i\varphi} \tag{2.26}$$

Where Ψ_i is the complex amplitude, and r_i and t_i are reflectance and transmittance, which are given by the Fresnel relations [74]:

$$\begin{aligned} r_1 =&(1-t_1) = r_{vapor/film} = \left(\frac{n_1-1}{n_1+1}\right)^2 \\ r_2 =&(1-t_2) = r_{film/solid} = \left(\frac{n_2-n_1}{n_2+n_1}\right)^2 \\ r_3 =&(1-t_3) = r_{film/vapor} = \left(\frac{1-n_1}{1+n_1}\right)^2 \end{aligned} \tag{2.27}$$

For a film characterized by thickness h and refractive index n, illuminated by monochromatic light of wavelength λ, the phase shift φ for normal incidences is:

$$\Psi = \frac{2\pi 2 n_1 h}{\lambda} + \pi \tag{2.28}$$

The sum of all reflected waves is:

$$\Psi_r = \sum \Psi_i \tag{2.29}$$

Hence the reflected intensity I_r is given by:

$$I_r = \| \frac{r_1 r_2 t_3}{e^{-i\phi} - r_2 r_3} \|^2 \|\Psi_0\|^2 \tag{2.30}$$

The $I_r / \parallel \Psi_0 \parallel^2$ as function of film thickness h is shown in Figure 2.7 B. The goal is to have the highest contrast for small film thickness changes, thus to maximize $(dI_r)/dh$. The easiest way is to shift the thickness to the range around the maxim of dI_r/dh, indicated by the arrows in Figure 2.7 B. The silica layer acts as an auxiliary layer interlaced between the film under investigation and the silicon substrate. It increases the overall thickness to the range around the maxim of dI/dh. As a result the image contrast for the thin film is improved (illustrated in Figure 2.7 C). Vertically the resolution is increased to nano-meter scale. Thickness variations in the range of molecular thin films (4nm per layer) can easily be distinguished [72].

Chapter 3

Materials and Methods

3.1 Material and sample preparation

3.1.1 Polymers

The following polymers were obtained in analytic grade from Polymer Source Inc: Diblock copolymers of polystyrene and polymethylmethacrylate (PS-b-PMMA) Mnx 10^3 = 55-b-22 $\rho = 945 kg/m^3$; polystyrene ("PS") Mn x 10^3= 25, 50 and 195; polymethylmethacrylate ("PMMA") Mn x 10^3= 996 Mn x 10^3= 45. All used as recived without further purification

3.1.2 Chemicals

Toluene ("TO", 99.9%) was from Sigma Aldrich, ethylacetate ("EA", 99.5%;) was from Chemsolute. Tetrahydrofuran ("THF", 99%) was from VWR. Dimethylformamide ("DMF", 99%), chloroform ("CHL", 99%) was from VWR. Anhydrous ethanol ("ETH" $\geq$99.8 %, max. H_2O 0.003 %) was from VWR. Water assigned as "W" was obtained from obtained a Milli-Q purification system (resistivity $18\,\mathrm{M\Omega cm}$). Methylcyclohexane ("MCH", 99.9%) was from Sigma Aldrich. N-decane ("D", $\geq$ 99%) was from Alfa Aesar. N-nonane ("NON", $\geq$ 99.8%) was from Sigma-Aldrich. N-octane ("O", $\geq$ 99%) was from Merk. N-heptane ("H", $\geq$ 99%) was from Fluka. The following chemicals were for particle synthesis. Hexachloroplatinic acid hydrate ($H_2PtCl_6 \cdot 6H_2O \geq$ 99%) was from Sigma-Aldrich. L-ascorbic acid ($C_6H_8O_6$, 99%) was from Sigma-Aldric. Trisodium citrate dihydrate ($C_6H_5Na_3O_6 \cdot 2H_2O \geq$ 99 %) was from Sigma-Aldric. Sodium borohydride ($NaBH_4$, $\geq$ 96 %) was from Sigma-Aldric. Sodium citrate was from Sigma-Aldric. Citric acid was from Sigma-Aldric. Sodium borohydride was from Sigma-Aldric. 3-(aminopropyl) triethoxysilane designed as APTES was from Sigma-Aldric too. Fullerene (C_{60}, $\geq$ 99.9 %) was purchased from Alfa Aesar.

3.1.3 Particles

Spherical silica particles ($\rho = 2400\,\mathrm{kg\,m^{-3}}$) with diameters of 50 and 200 nm (x_0 = 10 %(w/w) in ethanol) and 1 µm (aqueous dispersion, x_0 = 5 %(w/w)) where obtained from Aldrich. Silica particles with diameters of 550 nm (dry powder) were from Geltec. All silica particles had fairly uniform sizes (±10 % in diameter).

Spherical calcium carbonate particles (vaterite, $\rho = 1600\,\mathrm{kg\,m^{-3}}$) were synthesized in aqueous media [75], transferred to ethanol, decanted by centrifugation, and finally dried for storage. Their diameters varied considerable with a mean size of $\approx 2.6\,\mu\mathrm{m}$ (see in appendix Figure B.3).

Spherical polystyrene particles ($\rho = 1040\,\mathrm{kg\,m^{-3}}$), with sizes of 0.52, and 1 µm (aqueous suspensions $x_0 \approx 1\,\%(\mathrm{w/w})$) were obtained from Duke Scientific. Particles with diameters of 6, 8 (dry powder) and 25 µm (in aqueous suspension $x_0 \approx 1\,\%(\mathrm{w/w})$) were purchased from Thermo Scientific. The size distribution was fairly uniform (±10 %). Pt-NPs of different diameters d_{NP} were synthesized according to Bigall et *al* [76] (typical size variation of ± 20 %

(SEM) within batches of the same nanoparticle size sorted by centrifugation, see in appendix Figure B.1). They were suspended in water. Gold colloids were prepared according to Ref. [77]. $30\,\mathrm{ml}$ of an aqueous solution of $0.5\,\mathrm{mM}$ $HAuCl_4$ solution was poured into a $100\,\mathrm{ml}$ Erlenmeyer flask on a stirring hot plate and brought to a rolling boil. To the rapidly-stirred boiling solution, quickly $3\,\mathrm{ml}$ of a $0.25\,\mathrm{w/w}$ aqueous solution of sodium citrate dehydrates were added. As a result gold colloids form as the citrate reduces the gold ions. The total reaction time is about $10\,\mathrm{min}$. The dispersion was cooled to room temperature. The Au-NPs were collected by centrifugation and washed three times with MilliQ water and then stored.

3.1.4 Substrates and substrate preparation

As substrates served silicon wafer pieces of $\approx 2x2cm^2$ with natural oxide surfaces (oxide layer thickness $\approx 2\,\mathrm{nm}$) or with artificial oxide layers of ($50 \pm 1\,\mathrm{nm}$) thickness (Siegert Wafer), with surface roughness of $\approx 0.5\,\mathrm{nm}$. The substrates were first cleaned in an ultrasonic bath by a sequence of immersions (for 10 min each) in: 1.) Milli-Q water, 2.) ethanol ($96.9\,\%$, VWR Chemistry and Chemicals), 3.) acetone ($99.3\,\%$, J.T. Baker), 4.) ethanol, and 5.) Milli-Q water. In a second cleaning step they were immersed in piranha solution (H_2O_2 aqueous solution ($30\,\%$, Merck) and H_2SO_4 ($96\,\%$, ROTH), 1:3 volume ratio) for 30 min. Finally they were again immersed and sonicated for 10 min in Milli-Q water and stored therein no longer than $8\,\mathrm{h}$ before use. Just before use they were dried by blowing with dry N_2 (purity: 5.0).

3.2 Experiment methods and equipment

3.2.1 Static evaporation rate

Static evaporation rate were derived from the solvent loss of weight per time in several diameter Φ petri dishes: $12\,\mathrm{mm}$, $23\,\mathrm{mm}$, $34\,\mathrm{mm}$, $70\,\mathrm{mm}$, $96\,\mathrm{mm}$ (in general about $1\,\mathrm{mm}$ deep) filled with pure solvent or polymer solutions. The experiments were performed in the scale compartment closed on the sides and open on the top. The compartment volume was $185\,\mathrm{mm} \times 185\,\mathrm{mm} \times 245\,\mathrm{mm}$ cabin of the scale (OHaus Adventurer, AX224). The data (sample weight at intervals of $1\,\mathrm{s}$) was recorded automatically my the scale software.

3.2.2 Spin casting

Aliquots of $\approx 0.2\,\mathrm{ml}$ of the solutions/dispersions were deposited on the center of the substrate, which was already rotating at constant speed. A home-build spin cast set-up with the substrate exposed to the lab environment was used (see also Fig 3.1). To assure a rather homogeneous particle distribution and reproducible x_0 the dispersions were sonicated right before the aliquot for the spin cast deposition was taken.

3.2.3 Optical on-line observation of the film thinning

An optical microscope (Axio Scope A1 from Zeiss, long working distance objectives, e.g. SLMPLN50x OLYMPUS, NA=0.35) with a home-made mechanical stand was used for the in-situ observation of the spin coating process from the top (Fig 3.1). A blue diode laser served as illumination light source (6 W, 445 nm, LDM-445-6000, LASERTACK), despeckled by a combination of liquid light guide and a rotating diffusor [14]. The spin coater was mounted on a X-Y table to enable variable observation spots. Optical imaging was improved by interference enhanced reflection [41] and image processing [78]. Imaging was performed with a high speed camera EoSense®CL MC1362, Mikrotron GmbH, up to 1000 fps. The film thinning behavior was derived by interferometry from the brightness variations during film thinning [14, 29, 32, 78, 79].

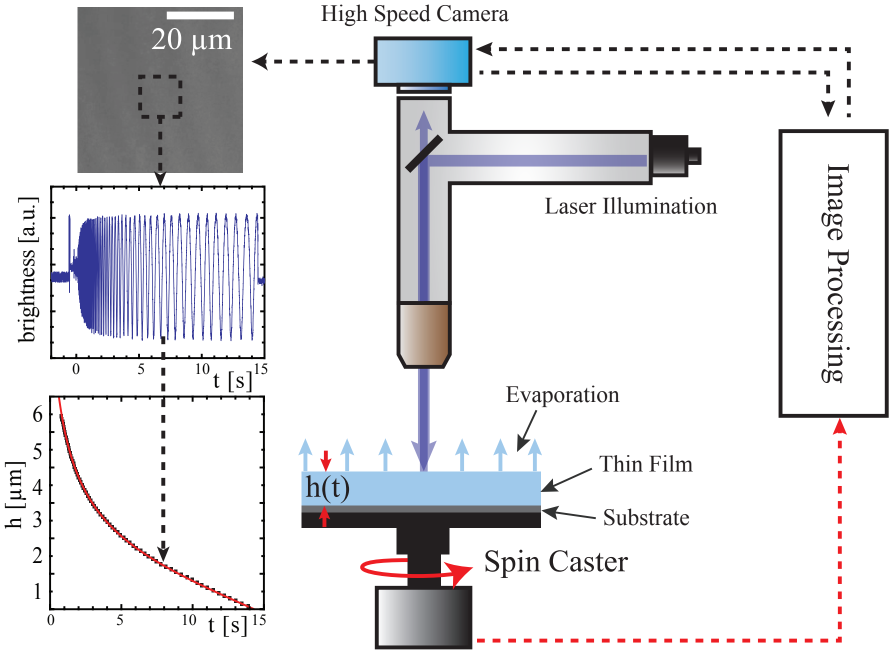

FIGURE 3.1: Experimental setup. The spin caster is synchronized with the image recording/processing. The vertical sequence on the left (from the top: optical image → interference pattern → film thinning) indicates how the online film thinning is derived from the optical images.

Height reconstruction by interference pattern

The Figure 3.2 shows the typical toluene film brightness variation (interference) versus time at $\omega = 1000\,\mathrm{rpm}$. The series of peaks and troughs that correspond to constructive and destructive interference conditions of the reflected light as the film thickness decreases during spin-coating. With knowledge of the final thickness ($h_f = 0$ in the case of pure evaporative solvents, and measured afterworlds for the polymer cases); it can be counted back the positions of the maxima and minima to use the standard condition for constructive interference to deduce the time dependence of the film thickness [80].

The variation of the gray level during the film thinning allows precise height reconstructions with a resolution of nanometers. Choosing a homogeneously drying area in the measurement the change in intensity is analyzed. According to the Bragg equation[1] for perpendicular incidence every peak in the curve corresponds to a certain interference maximum or minimum. The thickness change between two extrema for a given λ is the wavelength and liquid refractive index (n_{liquid}) is:

$$\Delta h = \frac{\lambda}{4 \cdot n_{liquid}} \tag{3.1}$$

Additionally, the contribution of the auxiliary silica layer thickness (h_{off}) has to be taken into account:

$$h_{off} = \frac{n_{SiO_2}}{n_{liquid}} d_{SiO_2} \tag{3.2}$$

---

[1] Bragg relation equation $i\lambda = 2d \sin\vartheta$[81]; where λ is the wavelength, i is a positive integer, d is the interplanar distance and ϑ is the scattering angle.

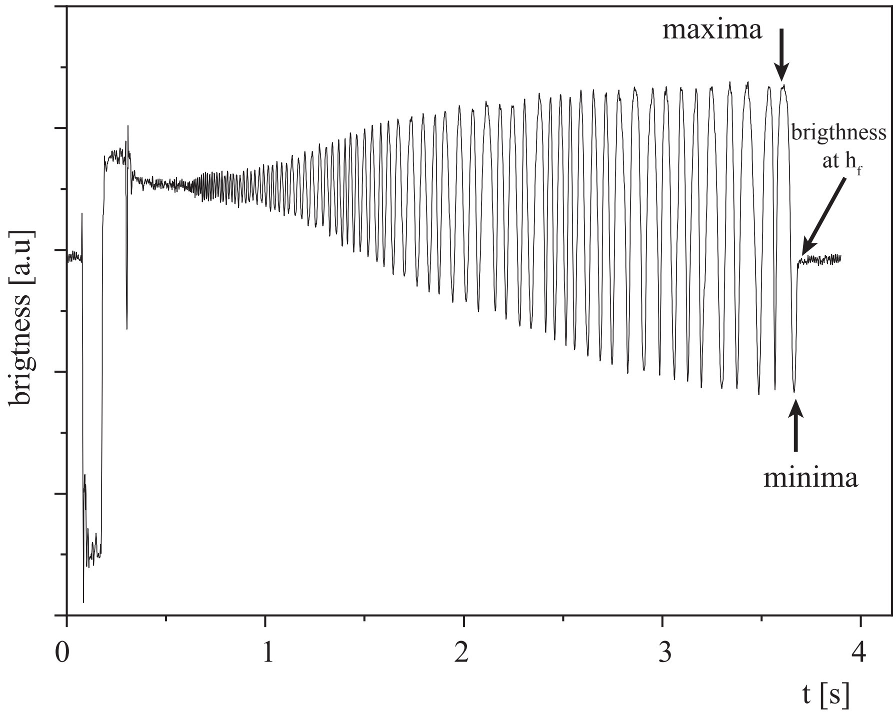

FIGURE 3.2: Film brightness variation versus time. Recorded for toluene at $\omega = 1000\,\mathrm{rpm}$.

With this, the absolute film thickness can be reconstructed.

$$h_i = \Delta h \cdot i - h_{off} \tag{3.3}$$

with thickness h_i at peak i. Additional data can be gained by linear extrapolation between the fringes.

Height reconstruction from the gray variation

For a precise analysis of the film thickness (also of static films) the gray variation between interference fringes is analyzed. The reflectivity response of a thin film system can be calculated with the help of the fresnel equations. To solve these relations, calculations where done, using the Mathematica version of the program code[2] by Steve Byrnes[83]. The absolute brightness measured by the camera under fixed illumination conditions can be calibrated via a homogeneous thinning liquid film (parameter for this calculation are shown in the appendix C.1). Assuming a linear evaporation in the last steps of drying, constant change of thickness. The gray value of each individual pixel can be translated into thickness. This can be done both by hand and by applying a polynomial fit to the thickness/reflective data[3] to automatically translate the gray value of each pixel into thickness.

3.2.4 Rheology

The rheological properties of polymer solution were measured with a Shear Rheometer Anton Paar MCR 301 in the cone-plate mode rotating between $1000 - 3000 rpm$ at $25°C$.

---

[2] The program is available at his website[82].

[3] between the Bragg reflections i and $i + 1$ order

3.2.5 Ellipsometry

The thicknesses, h_f, of the dry polymer films (equivalent: coverages Γ) were determined by ellipsometry for thickness up to 150nm; The index of refraction of the uncoated silicon substrate was measured as 3.86 (silicon), the one of the silica layer as 1.46. The index of refraction for PMMA was considered as 1.49 [84]. The index of refraction of PS was considered 1.58 [85] and 1.56 for the block copolymer; this index was derived by comparing of the film thicknesses with the respective coverages measured by AFM and ellipsometry in the range between 20-100 nm.

3.2.6 Measurement of final particles coverage

Except for the experiments with calcium carbonate the final particle coverages Γ were determined by directly counting the number of particles per area by either AFM (diameters of $50-200\,\mathrm{nm}$), or by optical microscopy (diameters of $500\,\mathrm{nm}$ and larger). The areas inspected by AFM were between $30\,\mu\mathrm{m}\times 30\,\mu\mathrm{m}$ and $100\,\mu\mathrm{m}\times 100\,\mu\mathrm{m}$, those inspected optically ranged between $200\,\mu\mathrm{m}\times 200\,\mu\mathrm{m}$ and $2\,\mathrm{mm}\times 2\,\mathrm{mm}$ (high resolution camera XIMEA-MQ042MG-CM, objectives: FLN10x (NA=0.25), SLMPLN50x (NA=0.35) and SLMPLN100x (NA=0.6) from OLYMPUS). The Images were processed and analyzed by the software packages ImageJ and Gwyddion. In all cases at least 3 different areas were investigated, including areas at the substrate center as well as at some distance from the center. It is found, that within a radius of $8\,\mathrm{mm}$ away from the center of the rotation, the coverage does not change, see in appendix Figure B.2. Care was taken to assure that the data were representative for the samples. In the case of $CaCO_3$ the coverage was indirectly measured from the cover area respect to the total area, taking account the particle size distribution, for more detail see Appendix B .

3.2.7 AFM image and nano-manipulation

Atomic force microscope (AFM) was used for imaging, film thickness measurement and nano object manipulation. The apparatus was a JPK Nanowizard 3 and NanoWizard 4, tips from Budgetsensors, tip radius 10 nm (Tap300Al-G)). The surfaces topography of the deposits were imaged and analyzed on tapping mode. Above 150 nm the deposit polymer film thickness were determined by measuring the depth of a scratch. The molecular deposition on substrates pre-coated with nanoparticles was performed by JPK moving sideways the nanoparticles in contact mode, ones the particles were localized by imaging in tapping mode. After moving the particle, the area was imaged in tapping mode to observe the surface that was underneath the particle. The image were processed and the quantitative data were analyzed with the softwares, JPKSPM Data Processing, Gwyddion and $SPIP^{TM}$ (Scanning Probe Image Processor).

3.3 Analytic expression and numerical approximations

3.3.1 Numerical Analysis of the Meniscus Profile

Using the program Origin the meniscus profiles were fitted with Eq.7.8 from the contact to the particle to the far-field surface. The distance where Eq 7.1 identifies h_∞ is the length L, given by the fit (Eq.7.8); the contact point with the particle (r_c, h_c) was iterated until the R-Square was at least 0.99. The fit reveled the contact to the imaginary/ideal fiber (r_i, h_i), allowing to estimate the contact angle by Eq. 7.11.

Chapter 4

Evaporation of a Pure Liquid Thin Film in a Spin Cast Configuration

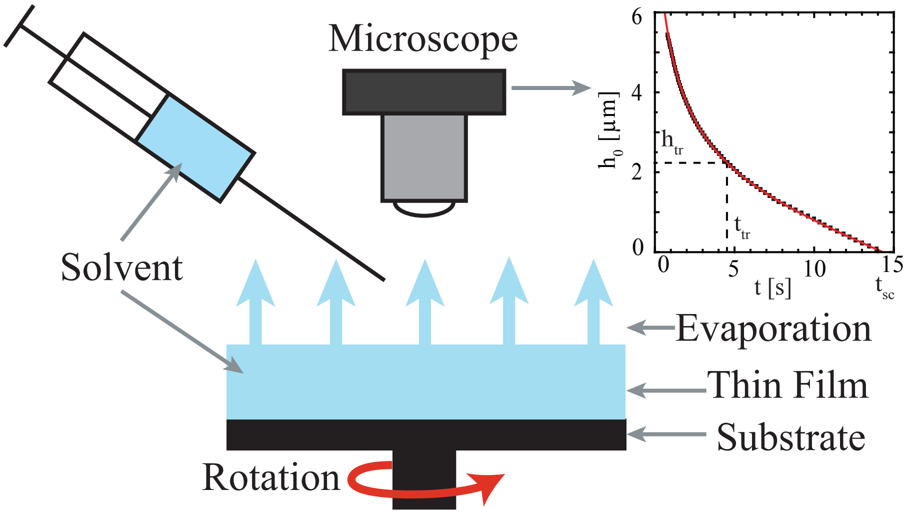

FIGURE 4.1: Pure solvent evaporation.

This chapter focuses on the evaporation behaviour of a thin pure liquid film in a spin cast configuration. Evaporation rates of various liquids under various conditions (in particular different rotation speeds) are measured and analyzed. The aim of the research is to find out, whether it is possible to directly calculate evaporation rates from basic liquid and process parameters. Thus it would be possible to calculate the results of a spin cast process (film thinning, deposition) a priori without any reference measurement on the evaporation behaviour. The findings show that this seems possible. The content of this chapter is the groundwork for a manunscript that is currently prepared to be submitted to the International Journal of Heat and Mass Transfer. The design and performance of the experiments have been by J. Danglad-Flores, as well the analytical and numerical calculations. S. Eickelmann contributed with part of the evaporation rate data derivative from thinning curves. J. Danglad-Flores wrote the first versions of the manuscript, under the supervision of H. Riegler.

4.1 Introduction

The zero order approximation and its modifications for higher solute concentrations and particle suspensions give valuable insight into the film thinning in a spin cast configuration, and allow an estimation on the final deposition of the nonvolatile components. For a quantiative description of the process the process parameters as well as the liquid properties have to be known. This means K and E have to be known. With viscosities available from literature (or approximated with available theoretical approaches in the case of mixtures) and the known speed of rotation(ω); K can easily be calculated. E on the other hand is a function of the evaporative conditions (technical specs of the spin cast setup) and appears less accessible by a priori calculations. even though the literature shows various examples where the final structure and properties of the deposit film are correlated to the solvent evaporation behaviour, no measurement or estimation of the evaporation rate are presented [86–91]. In part this may be because the measurement of E in a spin cast configurationis is not trivial technically. Only recently this has been done with sufficient precision with the on-line microscopy setup. Earlier measurements with non-imaging reflectometry also gave data on E [70]. But due to a lack of imaging, it could not be guaranteed that the thinning film was truely planar, without holes, etc. In practice, even if the zero order approach is applied to spin casting, it appears necessary to derive E experimentally from some "calibration" measurement, i.e. for the pure solvent. Based on this E the spin cast process can be then be analyzed and, for instance, the resulting deposition of the nonvolatile components can be predicted [32]. This empirical approach is a significant shortcoming and it would be a substantial progress if the measurement of the evaporation rate could be avoided.

In fact, already some time ago a theoretical description for the evaporation behaviour of thin volatile films in a spin cast configuration has been presented by Bornside, Macosko, and Scriven [53]. It has been accepted until now [92, 93]. But it has never been corroborated by direct measurements of E.

In the following measurement data from the evaporation behaviour of thin films in a spin cast configuraiton will be compared to the theoretical approach of Bornside, Macosko, and Scriven. It will be shown that it is indeed possible to estimate E a priori from literature data. Thus it is possible to describe the spin cast process a priori without calibration experiments of the evaporation rate.

4.2 Results

4.2.1 Evaporation from a planar liquid surface under static conditions

Fig. 4.2 depicts the experimentally measured static ($\omega = 0$) evaporation rates E for pure solvents. It is measured by solvent weight loss over time with the solvents in petri dishes of different diameters Φ. The evaporation rate is plotted as function of the inverse of surface diameter Φ [52]. Surface curvature, convection and side walls influence the static evaporation rate. By the experimental procedure setup these influences were minimized. Petri dishes with several centimeters in diameter were filled up to the rim. Thus most of the liquid surface was planar. The dishes were placed in the compartment of a precision scale, which was significantly larger than the petri dishes. During the measurements the compartment was closed at the sides, but open at the top. The loss of weight was measured as function of the time. Fig. 4.2 presents data from toluene (TOL) and water (W). The dashed lines show a linear fit of the measured E as function of $1/\Phi$. The intercepts for $\Phi \rightarrow \infty$ i.e., with negligible side wall effects, yield the static evaporation rates $E(\omega = 0) = e_0$ with $e_0(TOL) \approx 0.06\,\mu\text{m}\,\text{s}^{-1}$ and $e_0(W) \approx 0.02\,\mu\text{m}\,\text{s}^{-1}$

4.2.2 Evaporation of liquid films in a rotating plate

Fig. 4.3−A depicts experimentally measured thinning curves for pure toluene (full dots) and solutions of 8% PS-b-PMMA (MW:55k-b-22k) in toluene (open dots). For better visualization the curves are shifted laterally on the time axis. The dashed lines are theoretical fits to the experimental date according to Eq. 2.13. The parameter K (Eq. 2.14) is calculated

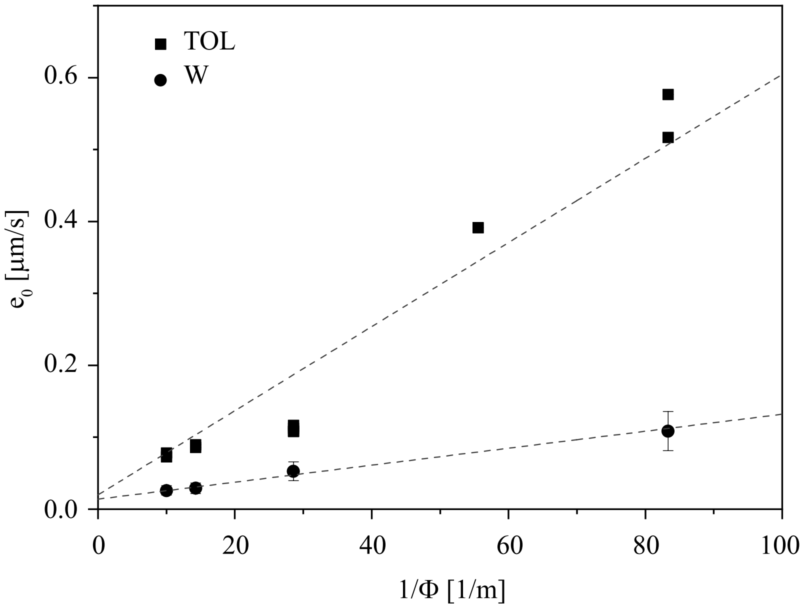

FIGURE 4.2: Experimentally measured evaporation rates at $\omega = 0$. The static evaporation e_0 rate is measured by solvent weight loss per time on petri dishes. The evaporation rate is plotted as function of the inverse of surface diameter Φ. The dashed lines show a linear fit. Data from toluene (TOL) and water (W) are presented. The Intercepts are $0.018\,\mu m\,s^{-1}$ and $0.015\,\mu m\,s^{-1}$ for toluene and water respectively.

from the system specifications (solvent properties, rotational speed). E is obtained from the best fit. The pure toluene data clearly show the transition from the non-linear hydrodynamic thinning at the beginning to the constant evaporative thinning, which ends with the complete evaporation of the liquid. The solid lines show the slope of the purely evaporative region $|dh/dt|$. This is assumed to be equal to the evaporation rate E. As long as the polymer solution is not too concentrated due to a loss of solvent, it has an evaporation rate E very similar to the pure solvent. Close to the end, with high polymer concentration the thinning slows down rather rapidly. Eventually thinning stops when it reaches the final thickness of the deposited polymer film. The gray dashed lines are the fitted thinning curves according to the zero-order theoretical model (Eq. 2.13).

Fig. 4.3—B presents experimentally observed thinning curves for several pure solvents. The obtained evaporation rates are: for chloroform, $E_{CHL} = 11.4\,\mu m\,s^{-1}$; for tetrahydrofurane , $E_{THF} = 7.0\,\mu m\,s^{-1}$; for toluene, $E_{TOL} = 1.8\,\mu m\,s^{-1}$; and for water, $E_W = 0.7\,\mu m\,s^{-1}$ (at 26 °C and a relative humidity of $40\,\% \pm 1\,\%$). It should be noted that the measurements from Fig 4.3 where coupled to on-line optical microscopy to make sure that the liquid film surfaces remained planar and did not dewet during thinning.

The different evaporation rates, E, are analyzed in terms of the theoretical model by Bornside, Macosko, and Scriven. Figure 4.4 shows the measured evaporation rates as function of the square root of the rotational speed, $\omega^{1/2}$ [31, 70, 94], for pure n-nonane (NON) and solutions of polymers (PS-b-PMMA) in toluene (TOL) with a concentration range from $0\,\%$ to $2\,\%$. For $\omega = 0$ the evaporation rates were taken from the static evaporation experiments. For the range of $500rpm < \omega < 4000rpm$ they were derived from the linear sections of the thinning curves. It should be noted that even at a polymer concentration of $2\,\%$ E is still quite similar to the pure solvent

Figure 4.4 shows that the data can be described by:

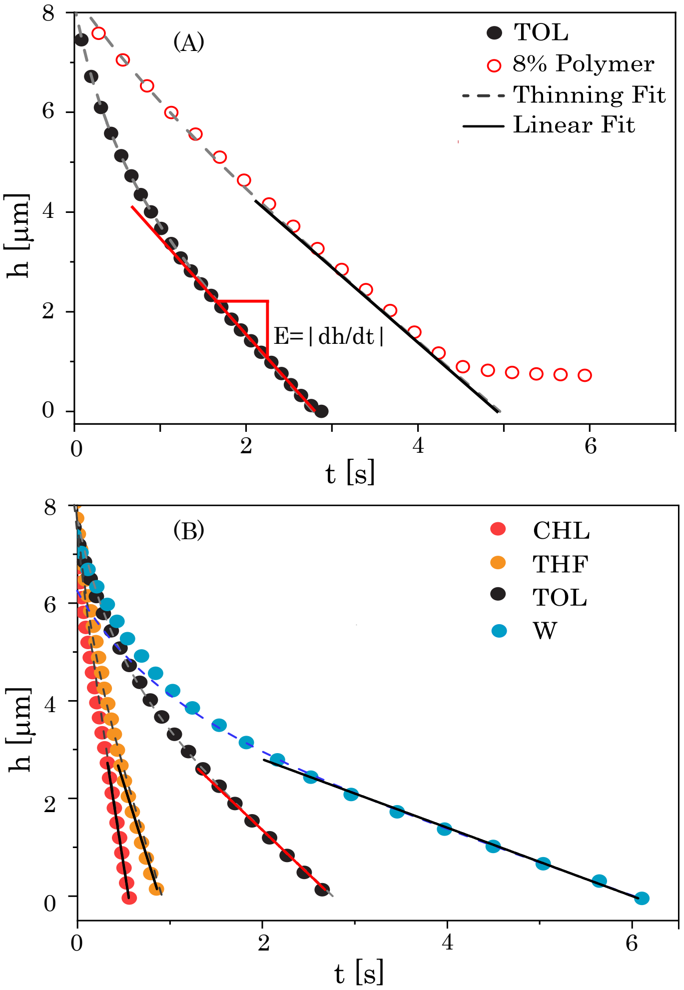

FIGURE 4.3: Experimentally measured thinning curves at 1000 rpm for (A) pure toluene (full dots) and 8% solutions of PS-b-PMMA (MW:55k-b-22k) in toluene (open dots). For visualization purpose the curves are shifted laterally on the time axis. The gray dashed lines are the theoretical fit to the thinning curves according to the zero-order model Eq. 2.13. While the solid lines mark the slope at the purely evaporative region. Panel B presents experimental data for a series of pure typical solvents: chloroform (CHL), tetrahydrofurane (THF), toluene (TOL) and water (W) at 26 °C and relative humidity of 40 % ± 1 %.

$$E(\omega) = e_0 + e_\omega \omega^{1/2}, \tag{4.1}$$

with e_0 as static evaporation rate and e_ω as "reduced" evaporation rate. With rotation speed typically used in spin casting, $e_0 \ll e_\omega \omega^{1/2}$. Therefore

$$E(\omega) \approx e_\omega \omega^{1/2} \tag{4.2}$$

is a valid approximation for Equation 4.1 in terms of e_ω for the case of spin casting. Together with Eq.2.12, it can therefore be concluded that:

$$e_\omega \cong \left(\frac{\sigma(x_a - x_{a\infty})}{R_g T \nu_b^{1/2}} \right) \left(\frac{P^* M_a D_{ab}}{\rho_L} \right). \tag{4.3}$$

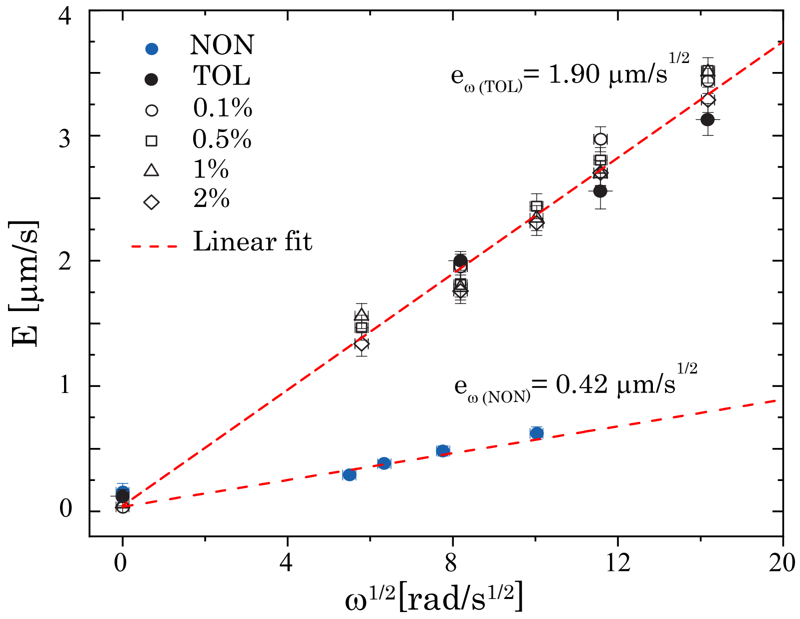

Figure 4.4: Experimentally measured evaporation rates, E, as function of the sample rotation rates ω, for pure n-nonane (NON) and toluene (TOL), as well for various polymer concentrations (PS-b-PMMA, MW:55k-b-22k, dissolved in toluene is given in mass percentage). The dash lines show the linear fit with slope $e_{\omega,TOL} = 1.9\,\mu\text{m/s}^{1/2}$ and $e_{\omega,NON} = 0.42\,\mu\text{m/s}^{1/2}$, and intercepts $0.06\,\mu\text{m}\,\text{s}^{-1}$ and $0.15\,\mu\text{m}\,\text{s}^{-1}$ for toluene and n-nonane respectively.

Figure 4.5 shows the experimentally measured e_ω as function of the pure solvent properties $P^* M_a D_{ab}/\rho_L$ (See also appendix, Table A.1). The typical variation for more than 3 measurements is only $7\,\%$. The slope of the linear fit (Pearson coefficient of 0.996); the interception at the origin is $5.6 \times 10^4\,\text{mol}^{1/2}/\text{m} \cdot \text{kJ}$. This is remarkably close to the constant factor from Eq. 4.3: With $R_g = 8.31 \times 10^{-3}\,\text{kJ}\,\text{mol}^{-1}\,\text{K}$, $T = 98.15\,\text{K}$, $\nu_b = 1.574 \times 10^{-5}\,\text{m}^2\,\text{s}$, $D_{ab} = 8.03 \times 10^{-6}\,\text{m}^2\,\text{s}^{-1}$ for toluene in air[95] (as a typical organic solvent) the predicted slope is $5.7 \times 10^4\,\text{mol}^{1/2}/\text{mkJ}$ (for $\sigma = 0, 563$, see Chapter 2, and $x_{a\infty} = 0$).

Table 4.1 shows for various typical pure solvents the measured static evaporation rates, e_0, the measured reduced evaporation rates e_ω, as well as the calculated reduced evaporation rates e_{th}. The static evaporation rates are in the range between $0.002\,\mu\text{m}\,\text{s}^{-1}$ and $0.7\,\mu\text{m}\,\text{s}^{-1}$. The values for the measured e_ω are quite precise, whereas the extrapolation of the measured static evaporation rates to $\Phi \to \infty$ results in rather wide error margins for e_0. Table 4.1 also compares the experimentally derived reduced evaporation rates, e_ω, with estimations for e_{th}, calculated with Eq. 4.3 (for solvent physico-chemical properties see Appendix A). The temperature of the system was taken as $26\,°\text{C}$. For water the relative humidity was assumed as $40\,\% \pm 1\,\%$, which means $x_{a\infty} = 0.0083$. On line optical microscopy shows that for all the experimental measurements in a spin cast configuration, after the drop flattening, during evaporative film thinning, the films remain flat, without disruptions or surface perturbations. Table 4.1 shows that for most of the investigated organic solvents, the values of e_ω and e_{th} agree within $20\,\%$. The most significant deviations appear for water, decane and dimethylformamide. The measured e_0 fits the tendency when the measured e_ω is extrapolated to E($\omega = 0$) (Figure 4.4) according to Eq. 4.1.

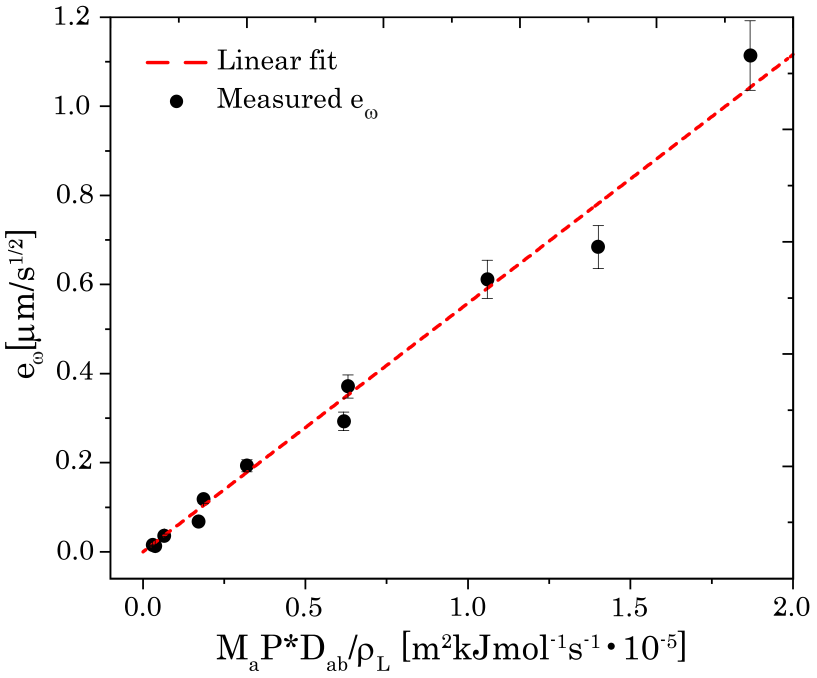

FIGURE 4.5: Experimentally measured reduced evaporation rates, e_ω, for various solvents as function of the pure solvent properties $(P^* M_a D_{ab}/\rho_L)$. The dash line shows the linear fit with interception in the origin, the slope is 5.6×10^4 mols$^{1/2}$/mkJ and the Pearson coefficient is 0.996.

4.3 Discussion

The evaporation rates of various liquids under static conditions and in a spin cast configuration have been measured and analyzed. Static evaporation rates are derived from weight losses of a liquid volume without enforced vapour convection. Measurements with different surface areas show that the results can be extrapolated to infinite size areas. Thus boundary effects are discarded and liquid-specific static evaporation rates, e_0, are derived. Evaporation rates with enforced convection in the spin cast configuration, $E(\omega)$, are measured for different rotation speeds by direct observation of the film thinning. It is found that the thinning respectively evaporation rate is proportional to $\sqrt{\omega}$. This agrees with a theoretical prediction published some time ago by Bornside, Macosko, and Scriven, [56] which has never been tested experimentally up to now. The theoretical approach also allows the direct calculation of the "reduced" evaporation rates, e_{th}, based only on literature data and readily available process parameters. Experimentally, it is found that $E(\omega) = e_{th}\sqrt{\omega} = e_\omega\sqrt{\omega}$. The experimentally derived e_ω of most of the investigated liquids agree quite well with the predicted values, e_{th}. Significant deviations are only found for water and liquids with low evaporation rates (decane and DMF).

Aside from this remarkable match between experiment and theory it should be noted that the theoretical approach predicts for the static case no evaporation at all. This is of course not the case. It is still open how the measured static evaporation rates, e_0, can be derived and explained theoretically from basic literature data. Nevertheless, the static evaporation rates $E(\omega = 0) = e_0$ are rather small comnpared to evaporation rates in a typical spin cast process. Therefore it can be assumed in an excellent approximation, that in a spin cast configuration the evaporation rate is given by $e_\omega\sqrt{\omega}$. The investigations show that this

TABLE 4.1: Experimentally measured e_0, e_ω, and theoretically calculated e_{th} for various pure solvents (ω = 1000 rpm). $T = 26\,°C$, RH (w) = $40\,\% \pm 1\,\%$ for the specific case of water. The "Error" indicates the difference between e_ω and e_{th}. The measurement error for e_ω is rather small. For e_0 it is rather large due to the extrapolation of the evaporation rates to $\Phi \rightarrow \infty$ as depicted in Fig. 4.2.

Solvent	e_0 $[\mu m/s]$	e_ω $[\mu m/s^{1/2}]$	e_{th} $[\mu m/s^{1/2}]$	**Error** [%]
Water	0.02	0.07	0.05	-33
Toluene	0.06	0.18	0.19	2
Ethyl acetate	0.43	0.61	0.58	-5
Chloroform	0.74	1.11	1.01	-9
Tetrahydrofuran	–	0.68	0.80	18
Dimethylformamide	0.01	0.01	0.02	53
n-Heptane	–	0.37	0.39	5
n-Octane	0.07	0.12	0.12	6
n-Nonane	0.15	0.04	0.04	15
n-Decane	0.0017	0.01	0.02	42
Methylcyclohexane	–	0.29	0.35	21

$e_\omega\sqrt{\omega}$ and thus the the outcome of spin cast processes can be estimated directly from literature and process parameter data. This finding makes obsolete a reference "calibration" measurements for spin cast setups and specific systems (solvent properties). With this the spin cast technique is applicable even without sophisticated instrumentation measuring explicitly evaporation rates. Neither theoreticals models that overestimate the solute (polymer) concentration effects.

Chapter 5

Deposition of Molecules from an Evaporative Thin Film

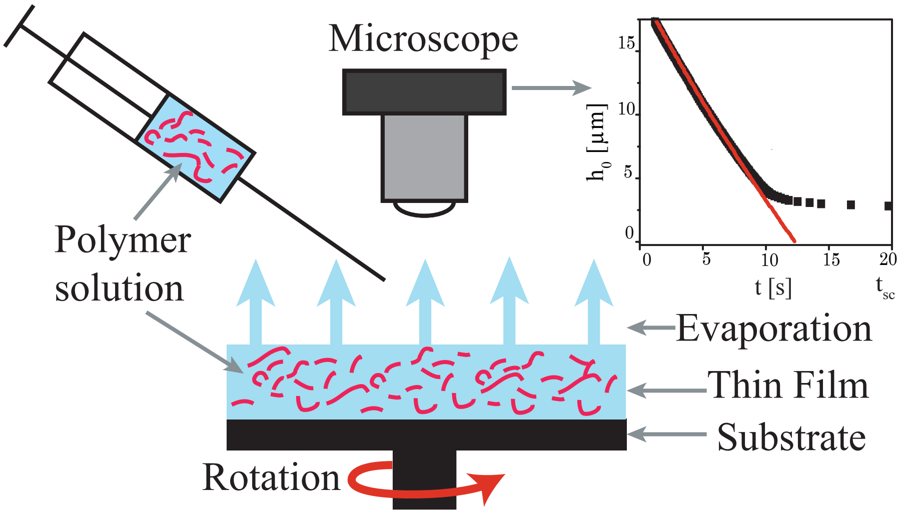

FIGURE 5.1: Deposition of polymers from evaporative thin films.

The content of this chapter has been published as: José Danglad-Flores, Stephan Eickelmann, and Hans Riegler. “Deposition of polymer films by spin casting: A quantitative analysis”. In: *Chemical Engineering Science* 179 (2018), pp. 257 –264

J. Danglad-Flores designed, conducted the experiments, analysed the data, and developed the theoretical description supervised by H. Riegler. J. Danglad-Flores wrote the first versions of the manuscript. S. Eickelmann build the experimental setup for the on-line imaging of planar thinning films and translated the raw interferometric data in thinning data. The manuscript was revised and edited by H. Riegler. All authors discussed and agreed with the manuscript content.

5.1 Introduction

Spin casting (spin coating) is a widely used technique to deposit films of uniform thickness on planar solid substrates[24, 57, 58]. It allows to deposit molecular thin films [72] to micrometer thick films, in a simple, robust, fast and reproducible way.

Although, even assuming idealized hydrodynamic and evaporative behavior as described in Chapter 2, film thinning and the accompanying solute enrichment is a rather complicated process. The increasing solute concentration has an influence on the hydrodynamic and on the evaporative properties of the film. Viscosity and evaporation behavior change continuously during film thinning. In addition, because the evaporation occurs from the film surface, the vertical solute concentration profile within the thinning film changes with time, possibly leading to a high solute enrichment close to the surface ("skin formation" [70], "crust" effect [96]). The combined process of hydrodynamic and evaporative film thinning has been investigated in quite a number of theoretical and experimental studies [31, 56, 60–69].

A practically useful theoretical analysis of the hydrodynamic-evaporative spin cast process should describe quantitatively how under the given (initial) process parameters (rotation, evaporation rate, liquid viscosity, etc.) the film thickness and its composition evolves with time. In particular, it should predict the final solute coverage. This has been done recently [29] in a *zero order* approach. For this approach it was assumed that the viscosity and the evaporation rate of the solution remains constant throughout the entire process of hydrodynamic-evaporative thinning. The values of viscosity and evaporation rate are assumed identical to those of the pure solvent. Based on easily measurable quantities this rather simple approach predicts the final solute film thickness (solute coverage) with remarkable quantitative precision for low solute concentrations (i.e., for final solute film thicknesses of up to several tens of nanometers). In the following we investigate at which solute concentrations this *zero order* approach starts to fail quantitatively and how it can be extended in a simple and practically feasible way into a "first-order" approach for higher solute concentrations i.e., higher final film thickness.

To this end, it is measured and analyzed in detail the hydrodynamic-evaporative thinning of solution films and the final solute coverages as a function of the solute concentrations for various solutes and solvents. This reveals at which solute concentrations the thinning behavior and final coverage starts to deviate significantly from the *zero order* approach. Based on these results a "first-order" description of the spin cast process is we present. The findings offer a rather simple and practically applicable recipe to quantitatively predict final solute film thickness of up to micrometers.

5.2 Results

The evaporative losses of the initially deposited liquid drop scale approximately with its linear dimension i.e., with radius r [6, 97, 98], whereas the time for the liquid flattening scales approximately with the inverse of the linear dimension i.e., with $1/r^2$ (see Emslie [30]). It turns out that liquids commonly applied in spin casting, such as toluene or water, deposited in typical quantities (drops of $100\mu l$ and more) on samples of a few cm^2 easily meet these conditions as can easily be estimated.

A rather crude estimation (derived from Fig. 2 of the paper of Emslie [30]) shows that $200\mu l$ of toluene deposited as a sessile drop with a Gaussian contour on a substrate rotating at 1000 rpm (i.e., $K \approx 6 * 10^9 m^{-2} s^{-1}$) will theoretically become a flat pancake of uniform thickness within $t = 1/(Kr^2) \approx 10\mu s$. On a planar substrate of about 1 cm^2 area this planar film is about $100\mu m$ thick. The evaporation rate of toluene for a planar film rotating at 1000 rpm is about $1\mu m/s$. In this case the evaporative losses within the flattening time of $10\mu s$ will lead to a loss of about $1nm$ toluene film, which will reduce the film thickness by a factor of only 10^{-5} (=$1nm/100\mu m$). In reality the time from a round drop touching the rotating substrate to a planar film through a sessile drop will last longer than only $10\mu s$. But by and large this crude estimation shows that for the given conditions (toluene, drop volume, sample size) evaporation can be neglected during the initial flattening process and the *zero-order* approximation of the spin cast process can be applied (which is confirmed by experiments[29]).

Fig. 5.2 depicts the final thicknesses h_f of different polymers (PS, PMMA, PS-b-PMMA) films deposited from polymer/solvent solutions with various initial (weighing in) polymer concentrations x_0 and different solvents (TO and EA). For low concentrations up to about $x_0 \approx 0.02$ (h_f around 100 nm) film thicknesses h is linearly proportional to the initial polymer concentrations x_0 in agreement with Eq. 2.21 (Fig. 5.2A). For higher polymer concentrations the film thickness is much higher than predicted (for $x_0 = 0.15$ by more than a factor of 3) as depicted in Fig. 5.2B. The dashed line in Fig. 5.2B shows the predicted coverage according to the *zero order* approximation Eq. 2.21. Measurements with other solute/solvent combinations yield similar results (see below).

Fig. 5.3 shows the experimentally measured thinning curves for pure toluene and various solutions of PS-b-PMMA in toluene from 0.001 to 0.15 w/w (the heights concentration is presented separately in the inset).

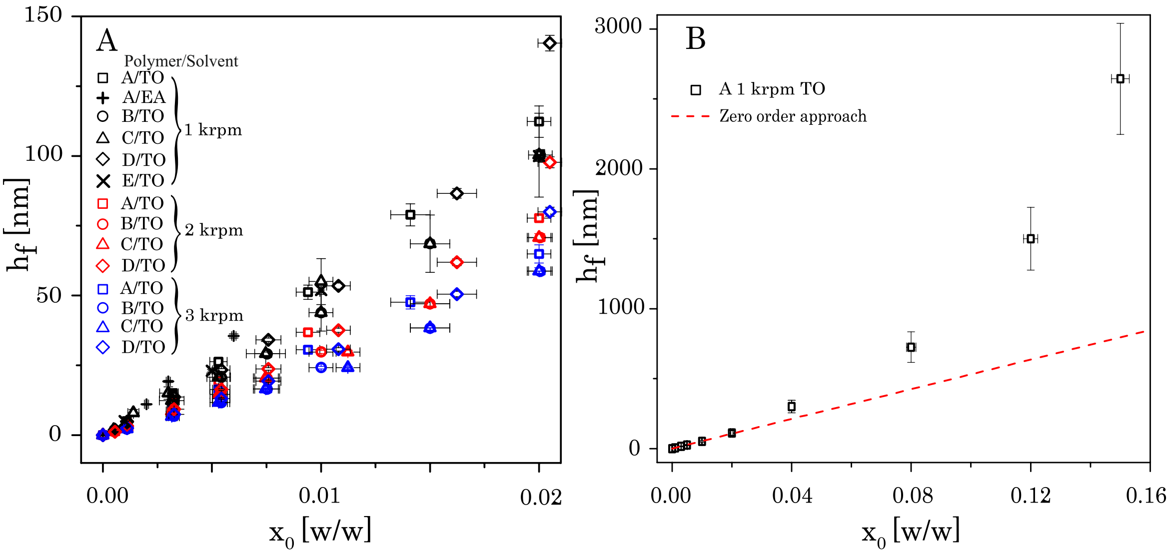

FIGURE 5.2: Final film thicknesses h_f measured by ellipsometry and AFM for A: PS-b-PMMA (Mn x 10^3= 55-b-22); B: PS (Mn x 10^3= 25): C: PS (Mn x 10^3= 50); D: PS (Mn x 10^3=195); E: PMMA (Mn x 10^3= 996) deposited from solutions in toluene (TO) and ethylacetate (EA) with various concentrations x_0 The sample rotations are denoted in krpm = 1000rpm. The panel (A) shows that for low polymer concentrations up to $x_0 \approx 0.02$ film thickness and x_0 are linearly proportional in agreement with the *zero-order* model (Eq. 2.21). For $x_0 > 0.02$ (i.e., $h > 50nm$) (panel (B)) h_f is increasingly much thicker than predicted in the *zero-order* calculation.

The thinning curves presented in Fig. 5.3 were taken from the same experiments that lead to the film thicknesses depicted in Fig. 5.2. The curves are plotted shifted laterally with different offsets in time to facilitate their presentation within the same figure without overlapping. The black solid lines are the fit of the data, the thinning curves are theoretically predicted based on the *zero-order* spin cast scenario presented below. In all cases the thinning occurs in the beginning rather rapidly, slows down, proceeds then linearly for some time until it slows down rather rapidly to end upon reaching the final height of the deposited polymer layer. For the lowest polymer concentrations the final thickness of the deposited film is barely visible with the scaling applied in Fig. 5.3. With the weighing in polymer concentrations exceeding about 1% the finally deposited polymer film clearly shows up in the curves. For $x_0 = 0.15$ initial polymer concentration the deposited polymer film is about 2.5 μm thick (see inset).

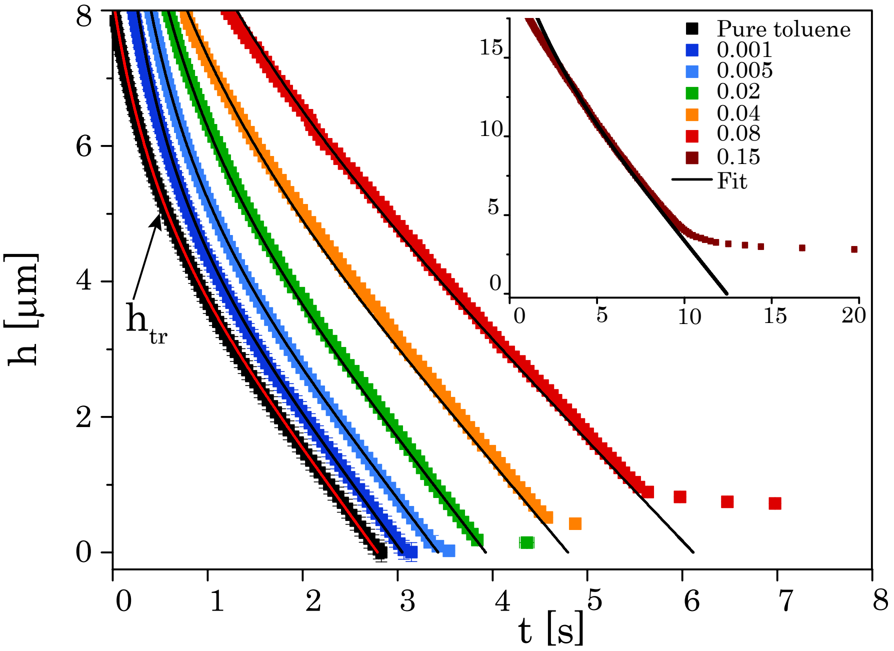

FIGURE 5.3: Experimentally measured thinning curves of pure toluene and various solutions of PS-b-PMMA (MW:55k-b-22k) in toluene at ω= 1000 rpm. For better visualization the curves are shifted laterally to each other on the time axis. Indicated for the pure toluene is also the transition height as they can be derived from fitting the thinning curve. The solid lines are the theoretical thinning curves according to the first-order model (see main text).

For polymer concentrations of up to about $x_0 = 0.02$ the crossover between the regime of steep and nonlinear hydrodynamic thinning and the linear regime of evaporative film thinning is clearly discernible. This transition range reveals h_{tr} (the h_{tr} indicated in the figure is the result of a fit of the thinning curve based on the first-order spin cast theory as presented below). With pure toluene h_{tr} is about 5.2μm. The transition height increases with increasing polymer concentration. With sufficient precisionh_{tr} can be derived quantitatively from fitting the experimentally measured thinning curves only for small x_0. With larger x_0 the crossover between hydrodynamic and evaporative thinning is getting too close to the early transient film formation process when the liquid undergoes the transition from a drop to a film. Therefore, in this case h_{tr} cannot be derived with reasonable accuracy from the experimentally measured thinning curves. On the other hand, all thinning curves presented in Fig. 5.3 display a rather wide range of a rather linear thickness decrease before the film thinning decreases rapidly due to the final polymer deposition/drying process. Presumably this linear range reflects film thinning dominated by evaporation.

Figure 5.4 presents the slopes, $|dh/dt|$, of the experimentally measured film thinning curves (Fig. 5.3) as a function of the time and the polymer concentrations. The indicated polymer concentrations, x_0, are the original weighing in values.

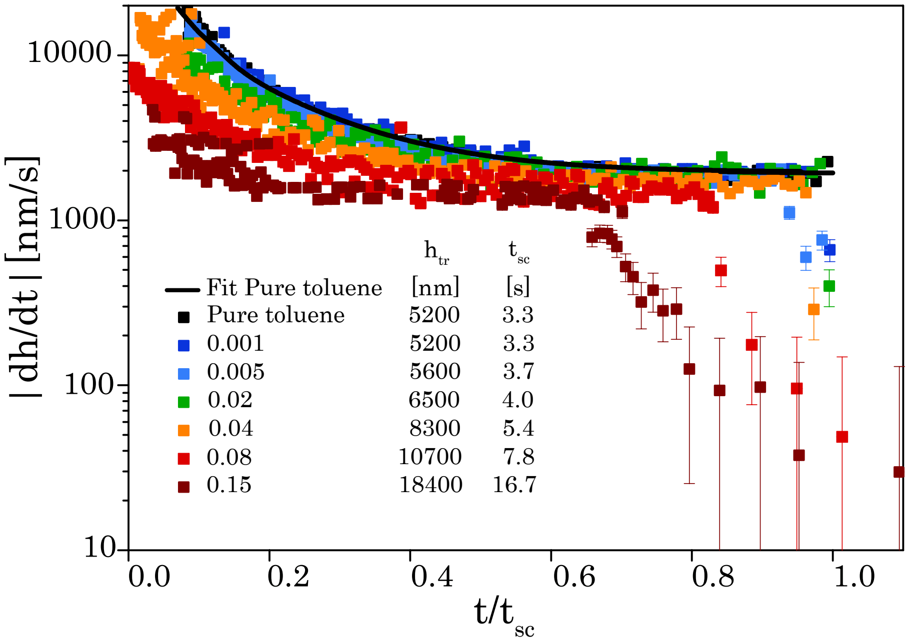

FIGURE 5.4: Thinning curves first derivate as function of the time. The time is rescaled by the total process time t_{sc} (Eq. 2.19). The polymer concentrations, x_0, are the initial weighing in values. The solvent is toluene, the polymer is PS-b-PMMA (MW:55k-b-22k).

The time is scaled with the process time, t_{sc}. Scaling the time with t_{sc} (Eq. 2.19) allows for a convenient presentation of all data in a single plot without too much stretching of the time axis (with increasing x_0 film thinning takes increasingly longer, as demonstrated in particular by the data presented in the inset of Fig. 5.3). Figure 5.4 reveals for all thinning curves a regime of film thinning with a constant slope, intermediate between the early non-linear hydrodynamic film thinning and the nonlinear drying behaviour at the end of the spin cast process. Except for the experiments with the highest initial polymer concentration ($x_0 = 0.15$), the range of constant slope as well as the slopes therein are nearly identical for all polymer concentrations. For $x_0 = 0.15$ the range of constant slope is shifted to relatively earlier times, but the slope therein is still quite similar to the cases of lower polymer concentration. According to the film thinning scenario (Eq. 2.13) this (constant) slope identifies the evaporation rate E of the liquid film after the film thinning ceases to be dominated by hydrodynamic forces.

At the end of a range with approximately constant slope$|dh/dt|$ (i.e., constant E), $|dh/dt|$ abruptly decreases. This sudden decrease of E is quite pronounced for the higher polymer concentrations. For low x_0 the sudden decrease occurs at rather thin films and only within a rather short time. Supposedly this late and rather slowly proceeding film thinning after the range with $|dh/dt|$ can be attributed to the final drying of a thin, polymer-rich film.

5.2.1 Evaporative process

Figure 5.5 depicts the experimentally derived evaporation rates, E, as function of the actual polymer concentration x (for PS-b-PMMA, MW=55k-b-22k, dissolved in toluene). The data are extracted from the results depicted in Figure 5.4. To this end it is assumed that film thinning at thicknesses below h_{tr} is dominated by evaporation and accordingly the polymer concentration is given by:

$$x(h) = \frac{h_{tr}}{h} x_0. \tag{5.1}$$

The solid blue line in Figure 5.5 was computed from Eq 2.12 based on the assumption of Raoult's law to predict the vapour pressure from a solution. The solid red line results as well from Eq 2.12, but taking account the solvent polymer molecular interactions through the Flory-Huggins relationship (Eq. 5.2); the vapor-liquid equilibrium behaviour of a polymer solution P^*_s was simplified by BMS[53] and give as,

$$P^*_\mathrm{s} = P^* exp[ln(x_a) + (1 - x_a) + \chi(1 - x_a)^2]. \tag{5.2}$$

where x_a is the solvent mass fraction and χ is the polymer-solvent Flory-Huggins coefficient, for polystyrene and polymethylmethacrylate in toluene $\chi = 0.45$ has been reported [99]. Figure 5.5 shows that even though the Raoult's law does not explain the evaporative behaviour of a highly concentrated polymer solution $(x > 50\,\%)$. It seems to confirm that the pure solvent evaporation rate E is applicable over the typical working region for weight in polymer concentration below $20\,\%$.

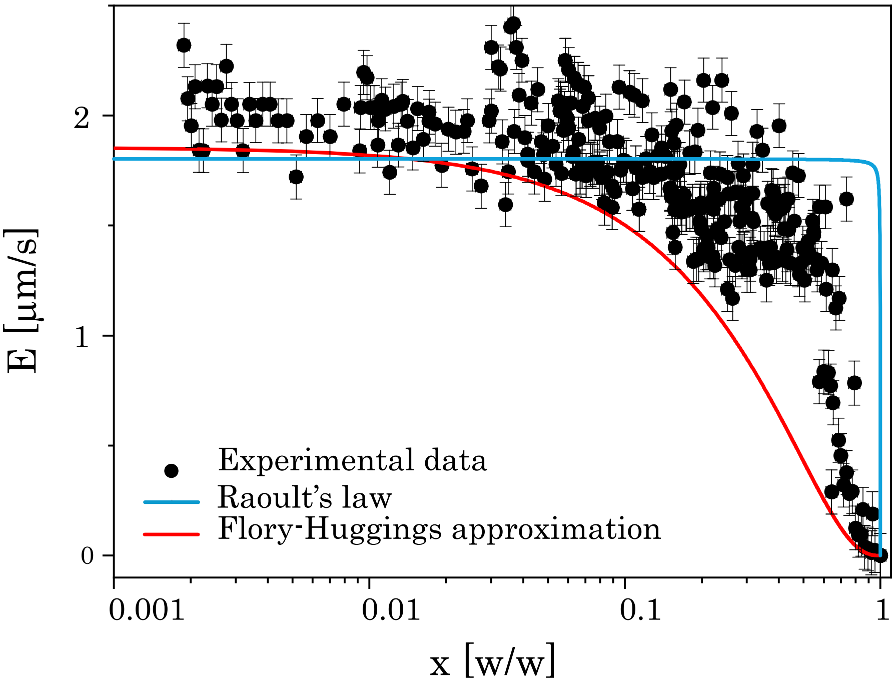

FIGURE 5.5: Evaporation rates E derived from the slopes dh/dt of the experimentally measured thinning curves of film thicknesses below h_{tr} as function of the polymer concentration. Because $h < h_{tr}$ evaporative thinning dominates and $dh/dt = E$. x is the polymer concentration within the film corresponding to the measured E. It is derived from the original weighing in value, x_0, by taking into account the loss of solvent due to evaporation. The data were recorded at ω= 1000 rpm. The blue solid line is the theoretical prediction from Eq. 2.12 assuming the Raoult's law to describe the vapour-liquid equilibrium of the polymer in toluene solution; the solid red curve takes account the correction for the polymer solvent interactions through a simplification of the Flory-Huggings expression (Eq. 5.2).

Figure 5.5 reveals that up to a polymer concentration of about $x = 0.05$ the evaporation rate remains identical to the one of pure toluene. Furthermore, even up to about $x = 0.5$ the evaporation rate decreases only by about 25%.

5.2.2 Initial hydrodynamic influence

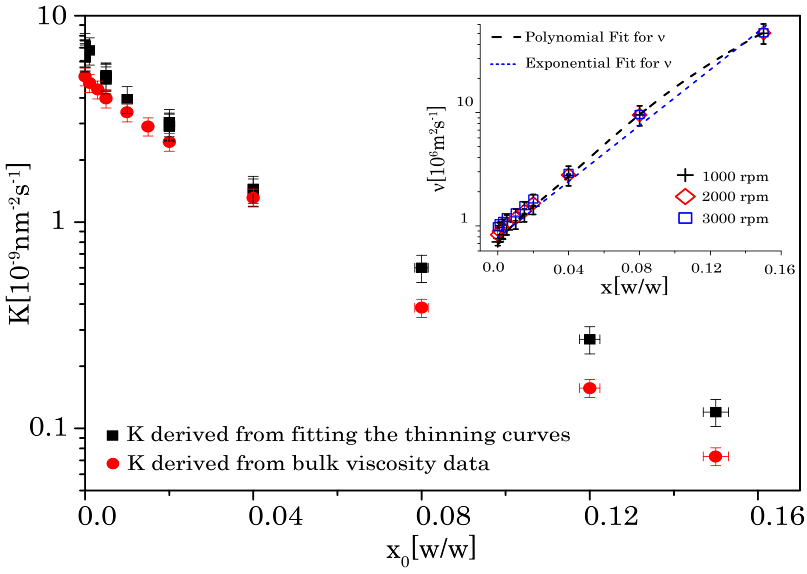

FIGURE 5.6: Spin cast parameters K plotted as a function of x_0, the weighing in polymer concentration (MW: 55k-b-22k, dissolved in toluene) at ω= 1000 rpm. The full black squares present K derived from best fits of the experimentally measured thinning curves according to Equation 2.13 and assuming (constant) evaporation rates E as derived from the intermediate, constant slope of the thinning curve (For the fits the thinning behavior (Fig. 5.5) during the initial transient transformation from a drop to a film of uniform thickness as well as the thinning during the final film draying is neglected). The full red circles in the main frame depict K calculated with Equation 2.14 from the viscosities obtained by the bulk measurements (see inset). The inset shows the dynamic bulk viscosities from bulk solutions at different concentrations and shear speeds. Also shown are fits of the bulk viscosity data (dashed: polynomial; dotted: exponential; see also main text).

Figure 5.6 presents the spin cast parameters, K, as function of x_0. The inset presents the bulk viscosities of the polymer solutions as function of x_0 measured by a rheometer. The "Experimental K" values are calculated from the experimentally measured viscosities via Equation 2.14. The "Fitted K" values are derived from best fits of the experimentally measured thinning curves assuming that they are following Equation 2.13. For the fits/simulations it is assumed that the evaporation rate is constant and identical to the value revealed by the intermediate, constant slope of the corresponding thinning curve as depicted in Figure 5.5 (i.e., essentially assuming in all cases the same E of $\approx 1.8\mu m/s$ except for $x_0 = 0.15$ with $E = 1.5\mu m/s$). Figure 5.3 shows some examples of such fits together with the corresponding experimental data [1].

---

[1] The fits assume that the thinning curves start at infinite thickness and end at zero thickness without any polymer/solute deposition i.e., a pure solvent with the E and K of the real polymer solution. It therefore focuses only on the experimental data in the range (1) after the transient film formation at the beginning of the spin cast process and (2) before the thinning curve shows the deposition of a polymer film at the end of the process. The deviations of the real thinning curve from an idealized thinning curve at the beginning and at the end of the real spin cast process are quite obvious so that the upper and lower cutoff for the fitting range is quite unambiguous.

The inset of Figure 5.6 shows that the viscosities of the polymer solution changes by about 2 orders of magnitude if the polymer concentration increases from $x = 0$ to $x = 0.15$. The solutions were investigated at three different speeds. As can be seen they behave like a Newtonian fluid. The experimental data could be fitted quite nicely with a polynomial of third order ($\nu = 10^6\rho^{-1}(13.3x^3 - 0.29x^2 + 0.035x + 0.0006)$) following ref. [100] as well as exponentially ($\nu = 700\rho^{-1}exp(28.5x)$) according to refs. [53, 101]; the density of the solution was taken as mass fraction proportionality from the density of each component.

The change of two orders of magnitude in ν is reflected in the decrease of K, which decreases by nearly two orders of magnitude when the polymer concentration increases from $x_0 = 0$ to $x_0 = 0.15$. Figure 5.6 reveals that K derived from fitting the thinning curves and K derived from bulk viscosity data agree quite well within the entire range of polymer concentrations. This means that the experimentally measured thinning curves up to $x_0 = 0.1$ can be described by Equation 2.13 with a constant E identical to the one of the pure solvent and K values based on the viscosity of the bulk solutions with the weighing polymer concentrations x_0.

5.2.3 General deposition theory from evaporative films

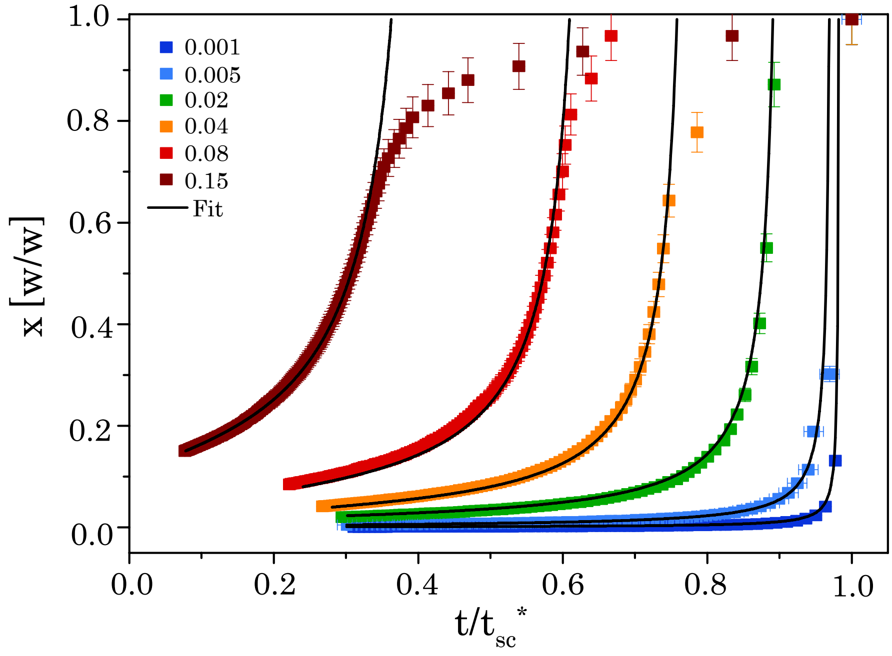

FIGURE 5.7: Time evolution of the polymer concentration x during film thinning for different initial x_0. The time is scaled with an empirical process time t^*_{sc} ($t^*_{sc} = t_{sc} + a$, with a = an additional time taking into account complete solute drying as derived from the empirical thinning curves (i.e., when $dh/dt = 0$)). The concentration evolution is derived from the empirical thinning curves with $x = x_0 * h_{tr}/h$. The black solid lines are derived from fits to the experimentally observed thinning curves assuming ideal thinning behavior according to Eq. 2.13 with a fixed E of the pure solvent and a fixed K based on the bulk viscosities of the initial solution as shown in Figure 5.8

Fig. 5.7 supports the solvent like evaporation assumption by presenting the time evolution of the polymer concentration x as derived according to Equation 5.1 as a function of time. The time is scaled with an empirical process time t^*_{sc}, which is a combination of the t_{sc} plus the additional time for complete solute drying (i.e., when $dh/dt = 0$) as derived from the empirical thinning curves. The black solid lines are derived from fits to the experimentally observed thinning behavior assuming the thinning behavior according to Eq. 2.13 with a constant E (of the pure solvent) and constant K based on the bulk viscosities of the initial solution as shown in Figure 5.6. The experimental data agree with the theoretical curves up to concentrations of about $x \approx 0.65$ or even higher (for the lower initial x_0). At concentrations higher than $x \approx 0.65$ the polymer enrichment slows down (as can also be seen in Figure 5.5).

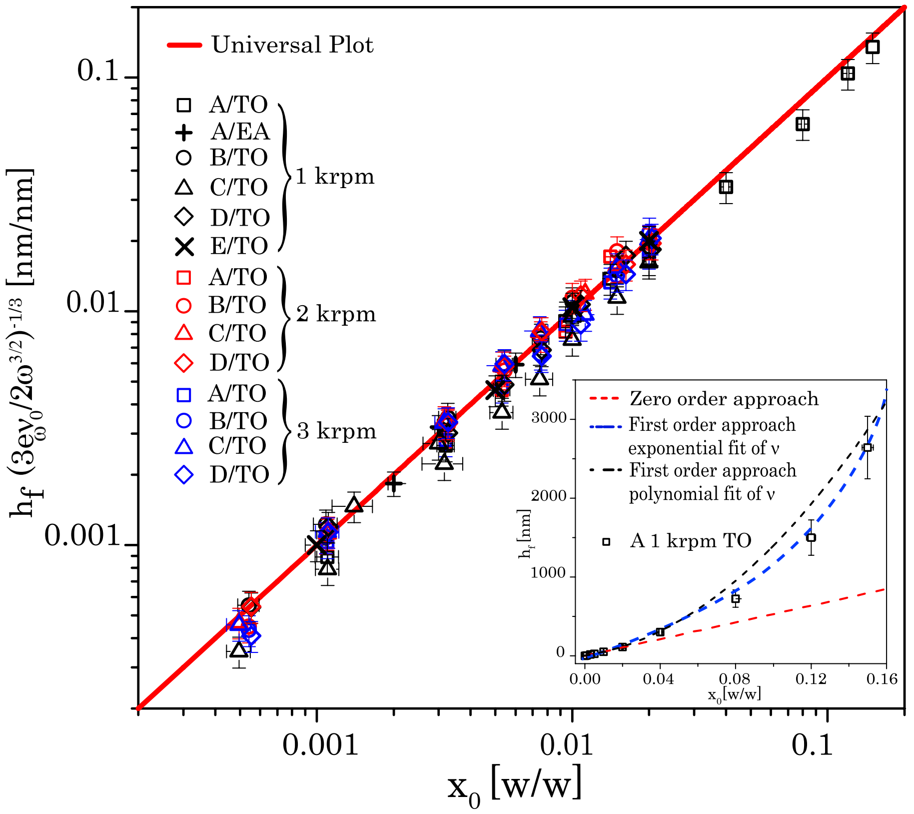

FIGURE 5.8: Final film thicknesses, h_f, as function of the initial weighing in polymer concentrations x_0. Data are shown for various combinations of polymers, solvents and rotational speeds. h_f is scaled by $\left(\frac{3e_\omega \nu_0}{2\omega^{3/2}}\right)^{1/3}$ assuming constant evaporation rates e_ω of the corresponding solvent (180 $nm/s^{1/2}$ for TO and 610 $nm/s^{1/2}$ for EA) and the bulk kinematic viscosities ν_0 of the solutions with concentration x_0. The inset shows h_f for polymer A dissolved in TO as function of the initial weighing in polymer concentration x_0. The dotted line shows h_f predicted according to the *zero-order* approach (see Fig. 5.2). The solid line shows h_f according to the first order approach resulting from Eq. 5.3 with constant e_ω and bulk viscosity properties ν_0. The red dashed line shows hf predicted according to the *zero-order* approach (see also Fig.5.2). The black dashed line shows h_f according to the first order approach from Eq. 5.3 with constant e and bulk viscosity properties ν_0 as presented in Fig. 5.6 and fitted by an polynomial rheological behaviour. The blue dotted line shows the exponential fit of the bulk rheological behaviour.

Figure 5.8 presents the experimentally measured final polymer film thicknesses, h_f, as function of the initial weighing in polymer concentrations x_0. The final film thicknesses are scaled by the transition heights, h_{tr}, of the corresponding systems. The data are from different polymers, different solvents, and different speeds of rotation. They agree very well with a linear behavior between the final film thickness of the deposited non-volatile solute, h_f, and the initial (weighing in) concentration, x_0, of the solute according to Eq 5.3, where $E = (e_\omega \sqrt{\omega})$ (as was shown in Chapter 4) has been replaced by e_ω according to Eq 4.2:

$$h_f = x_0 \left(\frac{3 e_\omega \nu_0}{2 \omega^{3/2}} \right)^{1/3} = x_0 \left(\frac{3 e_\omega \eta_0}{2 \rho_0} \right)^{1/3} \omega^{-1/2}. \tag{5.3}$$

The evaporative conditions are quite similar for different spin cast instruments, as long as the ambient vapor phase is not coming close to becoming saturated with the solvent vapor. The main parameter affecting the evaporation is the rotation

We developed Equations 5.3, as a general expression of the first order correction to predict the final solute film thickness, h_f, as a function of the physiochemical system parameters. All parameters are easily measurable or approximated. They are either (1) weighing-in properties (η_0, ρ_0), easily accessible by bulk measurements, (2) adjustable process parameters (x_0, ω), or (3) parameters accessible with one single experiment (e_ω from the measurement of h_f for a given set of η_0, ρ_0, x_0, and ω) or approximated by Eq. 4.3 for the specific solvent and environment condition (vapor solvent content of the spin cast particular setup).

5.3 Discussion

The deposition of polymer films onto planar substrates by spin casting polymer solutions with volatile solvents was analyzed. By measuring and understanding how in detail the hydrodynamically flattened solution film gets thinner due to hydrodynamics and evaporation, and finally forms a dry polymer film. With particular interest on the behavior of solutions with a relatively high polymer concentration, which lead to final dry polymer film thicknesses of up to several micrometers. In this case the simple *zero-order* approach that was presented earlier [29], which essentially neglects the impact of the dissolved solute on the spin cast process, is quantitatively not correct any more. Figure 5.2 reveals experimentally above which weighing in solute concentrations, x_0, the *zero order* approach fails quantitatively with respect of the predicted final film thickness. Details on the film thinning behavior for different polymer concentrations are presented in Figure 5.3. Its analysis (Figure 5.4) reveals the "real" evaporation rates during film thinning (Figure 5.5) i.e., the evaporation rates for films of an actual polymer concentration x that results from the polymer enrichment due to the solvent evaporation. It is found that the evaporation rates are barely affected by the polymer concentration up to $x \approx 0.5$. This can be understood because 1.) of the relatively low *molar* solute concentration even for large x and 2.) there is barely any relative enrichment of polymer close to the film surface. The solute enrichment close to the surface can be estimated as follows: The vertical solute distribution is determined by the competition between the solute enrichment close to the film/air interface due to the solvent evaporation and the solute dilution due to diffusion away from the film/air interface. The relative strength of these antagonistic effects is characterized by the Sherwood number [29]. With diffusion coefficients D of typically $\geq 10^{-11} m^2/s$ for the polymers used, $Sh_{h_{tr}}$, the Sherwood number at h_{tr}, is smaller than 1. This small Sherwood number means that the vertical solute distribution within the thinning film is rather uniform at h_{tr}. It also means, to a first approximation, that the solute composition is even more uniform as the film is getting thinner than h_{tr} due to evaporation.

The data of Figure 5.4 show that the evaporation rates are essentially those of the pure solvent for up to $x \approx 0.5$. E decreases only significantly for $x > 0.5$, indicating a drying process of the polymer-rich solution at these polymer concentrations [102]. Still, even with $x > 0.5$ a pronounced polymer enrichment at the film surface ("crust" or "skin" formation) is not likely, because in this case the evaporation rate would decrease much steeper than observed [103]. Due to the rather constant evaporation rates (Figure 5.5) for films much thinner than h_{tr} even for $x > 0.02$, E can be excluded as main reason for the deviation between the measured final film thicknesses and the ones predicted by the *zero order* analysis. Instead, as main cause for this discrepancy the substantial increase in viscosity with increasing polymer concentration was identified as depicted in Figure 5.6. Most remarkable, K_0 i.e., the *weighing in* kinematic viscosity ν_0 is the key parameter, which determines the final film thickness h_f. Its impact on the final film thickness results from its effect on the transition height, h_{tr}. With increasing K the transition between hydrodynamic and evaporative thinning is shifted to larger film thicknesses, resulting in thicker final solute film thicknesses, h_f. The variation of K respectively ν during film thinning has no influence on h_f, because this variation occurs essentially during evaporative film thinning. In this case the amount of solute per film area i.e., h_f, remains constant.

Figure 5.8 presents in a universal plot the relation between the final thicknesses, h_f, and the initial polymer concentration, x_0, for different polymers, solvents and rotation speeds. The final film thickness is normalized with the transition heights of each experiment based on solvent-specific and instrument-specific evaporation rates e_ω, as well as ν_0, the measured weighing in kinematic viscosity of the solutions. The excellent agreement between the measured data and the data calculated with Equation 5.3 demonstrates the validity of the first-order approach leading to Equation 5.3. By just replacing the viscosity of the pure solvent by the viscosity of the solution. Equation **??** results practical for spin cast applications because η_0 and ρ_0 are accessible (estimable/measurable) bulk properties. The parameter ω is adjustable. And the solvent- and instrument-specific value for e_ω can be determined with just one experimental measurement of h_f through Equation **??** or estimated by Eq 4.2.

there are a quite a number of experimental and theoretical studies literature addressing similar topics as analyzed here [24].

In particular the relation between the final solute film thickness and whatever is considered as relevant spin cast parameters is addressed in several previous publications. Indeed data similar to Figure 5.2 can be found in the literature [31, 104, 105]. On-line thinning curves similar to those of Figure 5.3 have also been published before [34, 37, 106–109]. However, these data were never analyzed in detail theoretically in respect to a simple, transparent spin cast scenario without a guesswork of adjustable parameters. For instance, experimental findings have been explained with evaporation rates and/or viscosities, which (supposedly) continuously vary during the spin cast process due to the solute enrichment [110]. Based on suitably selected adjustable parameters the *first order* models *explain* the experimental findings. But these earlier models fail to *predict* the result of a spin cast process quantitatively, in particular on a more general, universal scope [111], because the models are based only partially on final deposit experimental data. Data as presented in Figures 5.4, 5.5 and 5.7 were not available in the literature.

Moreover, considering the findings from Chapter 4. By substituting Eq 4.3 in Eq. 5.4 a general expression is presented, as:

$$h_f = x_0 \left[\left(\frac{3\eta_0}{2\rho_0} \right) \left(\frac{\sigma(1 - x_{a\infty})}{R_g T \nu_b^{1/2}} \right) \left(\frac{P^* M_a D_{ab}}{\rho_L} \right) \right]^{1/3} \omega^{-1/2}. \tag{5.4}$$

The Eq 5.4 allows to predict the final film thickness based in the theoretical pure solvent evaporation rate, the rheology of the initial solution, and the parameter ω. However, it should be consider that Eq. 5.4 does not take account specific set-up configuration (e.i. chamber dimension, inner gas flow, etc.)

The result of these new experimental insights is a rather universal, concise theory, which (1.) accurately predicts the final film thickness for a wide range of thicknesses (Figure 5.8), (2.) is based on only a few measurable (bulk) quantities (Equation **??**), (3.) is supported by experimental data (in particular Figure 5.4) and, (4.) is based on a simple, transparent physics approach.

5.4 Summary and Conclusion

For those who wants to apply evaporative spin casting (a solution of a nonvolatile solute and a volatile solvent) a lucid and well-defined "recipe" to achieve a specific solute coverage. In particular, based on detailed experimental investigations. A final "master" formula is provided (Eq. 5.3). Step-by-step we explicitly relate the theoretical description to the experimental observations and specify the boundary conditions of its validity. It turns out that the spin cast process is rather straightforward even for relatively high solute concentrations. Only a few easily measurable bulk system parameters (η_0, ρ_0, ω) and one estimable (e_ω) are sufficient to describe the process and to predict its main result, the final solute coverage. Beyond that, the data and analysis presented in this report disclose a transparent picture on the physics occuring during evaporative spin casting, such as the thinning behavior, the evaporation behavior, and the evolution of the solute concentration.

Chapter 6

Deposition of Particles from an Evaporative Thin Film

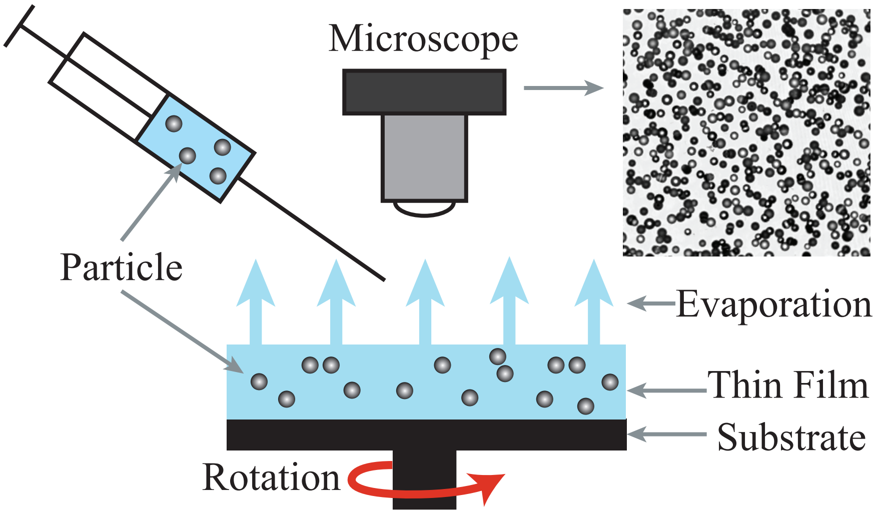

FIGURE 6.1: Online imaging of the deposition of particles.

This chapter was accepted in Langmuir as: "Controlled Deposition of Nano- and Micron-Size Particles by Spin Casting ". It analyses the particle deposition by spin casting of a dispersion of particles in a volatile liquid. J. Danglad-Flores designed and performed the experiments. He did the analytical and numerical calculations. He also wrote the first versions of the manuscript. K. Eftekhari synthesized the calcium carbonate particles. She also assisted during some of the deposition experiments. Skirtach A. revised the manuscript. The manuscript was revised and edited by H. Riegler. All authors discussed and agreeded with the manuscript content.

6.1 Introduction

Up to some years ago evaporative spin casting was mainly used to fabricate thin polymer coating [24–28]. But recently the spin casting of suspensions of nano size objects, such as nanoparticles [112], nanorods [113], or nanowires [114, 115] in volatile liquids have been used to produce thin layers of such objects on solid substrates. Thus, for instance ordered monolayers [116–118] or multilayers [119, 120] have been prepared with special optical properties [38, 113, 121, 122]. The particle coverage is an important system parameter, which is adjusted by the process parameters (initial concentration, rotational speed, solvent, etc.). Up to now, the process conditions to obtain a certain, desired particle layer coverage from a certain particle/liquid dispersion were derived empirically by trial and error [123]. However, there was no consistent and reliable theoretical approach available, which allows the prediction of the particle deposition based on the applied process parameters.

Recently, Karpitschka et al. [29], based on experimental data and, provided a rather transparent and particularly practical theoretical approach for evaporative spin casting of solutions with low solute concentrations. Recently it has been shown [32] that with some substantial modification this scenario is valid even for solutions with rather high polymer concentrations. The resulting, easily applicable approach allows to predict the final layer coverage (the film thickness) for diluted molecular solutions of small molecules, as well as for relatively high concentrated polymer solutions leading to final film thicknesses of up to several microns.

The deposition of particles will be tested for dispersions of low and moderately high concentrations of particles in volatile liquids with particle sizes ranging from a few tens of nanometers to tens of microns.

It should be take account that spin casting of particle dispersions differs from that of molecular solutions in at least two aspects: 1.) The size of the particles may reach or even exceed the thickness of the transition height (typically a few microns). Thus even low particle concentrations may have an impact on the film thinning behavior ergo the final coverage). 2.) Sedimentation during the spin cast process may contribute to the final coverage.

Taking account the findings from Chapters 4 and 5; the earlier approach [29, 32], and its limits will be tested, and modified to correctly predict the coverage in the case of particle dispersions.

Considering that above the h_{tr}, the solute concentration remains approximately c_0, the weighing in concentration. This is a reasonable assumption, as Karpitschka et al.[29] and Danglad-Flores et al.[32] have shown. Later, as soon as the film is thinner than h_{tr}, film thinning is governed by evaporation only. Therefore all of the solute, which is contained in the film with thickness h_{tr} is finally deposited on the substrate:

$$\Gamma_0 \approx c_0\, h_{tr} = c_0\, (E/2K)^{\frac{1}{3}}. \tag{6.1}$$

For particle dispersions it is convenient to use c_0 in particles per volume, which via Eq. 6.1 directly yields Γ_0 in number of particles per area. If the particle concentration is given as mass fraction, x_0, c_0 can be derived via $c_0 = x_0(3\rho_L)/(4\pi\rho_p \mathrm{R}^3)$ (ρ_p = particle density, ρ_L = liquid density and R the particle radius).

6.2 Results

6.2.1 Particle coverages

Fig. 6.2 shows examples of AFM and optical images with particles deposited on the silica surfaces. At various c_0 dispersed in water or ethanol. Therefore the concentration in numbers of particles per volume decreases rapidly with the particle diameter d_p. As a result the numbers of particles per area (the coverage) decreases with increasing particle size. Frames A to D present SiO_2 particles with diameters of 50, 200, 550 and $1000\,\mathrm{nm}$. Frames E to F show PS particles with diameters of d_p= $8\,\mu\mathrm{m}$ and $25\,\mu\mathrm{m}$. Image G shows the case of $CaCO_3$ particles with a mean diameter of $d_p \approx 2.6\,\mu\mathrm{m}$ as derived from the size distributions by optical microscopy (frame H). One can see that in some cases the particles are not uniformly distributed on the surface. In particular in the case of small diameters the particles tend to form 2D aggregates. Most pronounced is the particle aggregation in the case of the $CaCO_3$ particles. In the cases of the silica and the PS particles the particles are of rather uniform sizes and individual particles can easily be identified. Thus, it is possible to measure quite

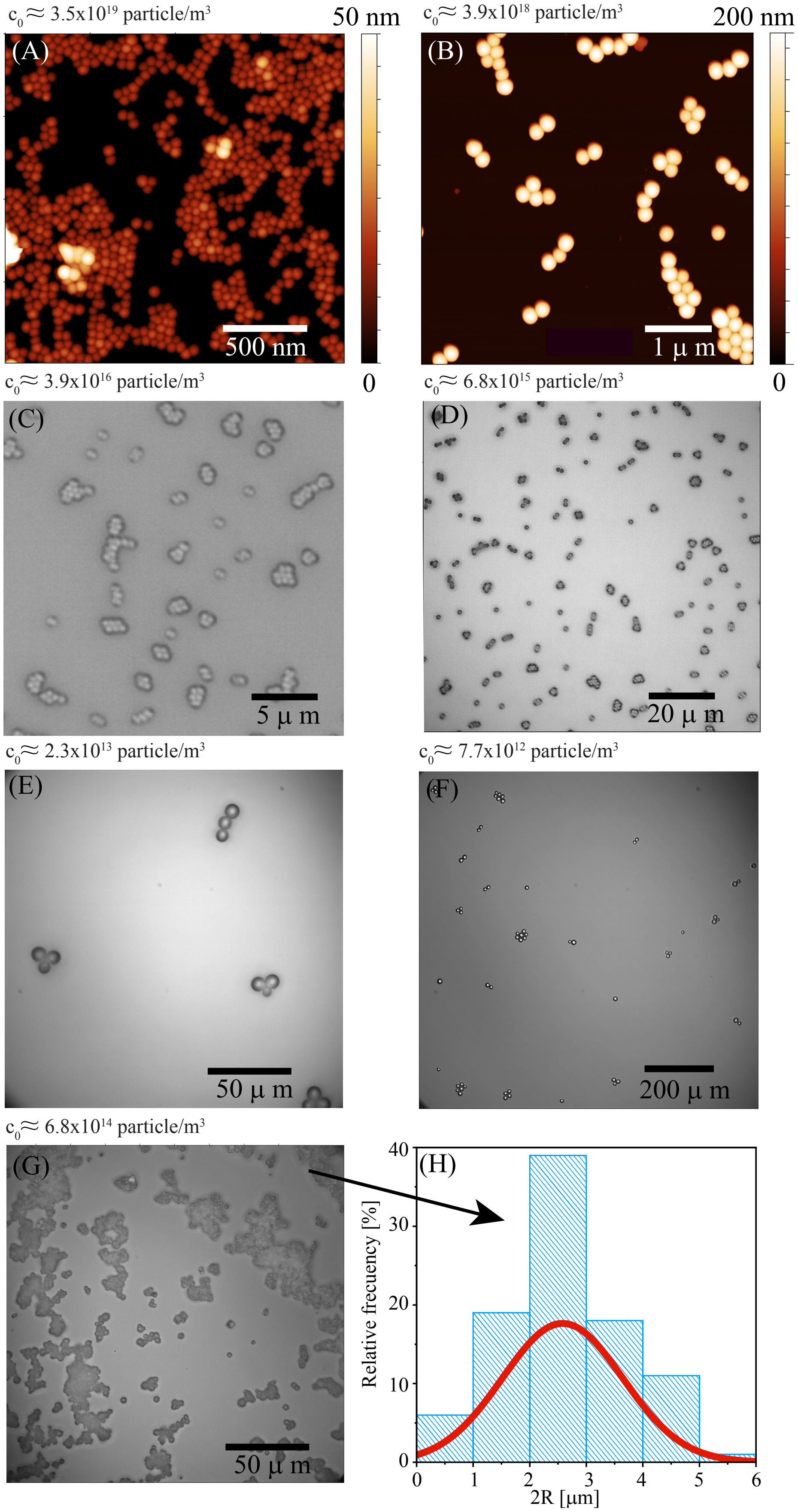

FIGURE 6.2: Surface coverage with particles deposited from dispersions $\omega = 1000\,\mathrm{rpm}$. (A-D) silica particles (SiO_2) with diameters of d_p = 50, 200, 550 and 1000 nm; (E and F) polystyrene particles (PS) with d_p = 8 and 25 μm; (G) calcium carbonate particles ($CaCO_3$) with a mean diameter of d_p = 2.6 μm, and (H) details of the particle size distribution of frame G. The silica particles with d_p = 50, 200 nm and the PS particles with d_p = 8 μm were dispersed in ethanol. The other particles were dispersed in water.

precisely the average particle coverages in numbers of particles per area by just counting the particles. With the calcium carbonate particles the approach of counting particles per area is rather awkward, because the particle size varies considerably. Therefore the relative amount of surface area, which is covered by the particles is determined. Separately the particle size distribution is approximated by analyzing cases of low coverage from low weighing in concentrations, which allowed to discriminate individual particles (see supplement). the coverage is *estimated* for the entire sample in number of particles per area From the combination of the size distribution and the surface coverage.

6.2.2 Particle coverages as function of concentrations and sizes

Fig. 6.3 shows the number of particles deposited per unit area, Γ, scaled with the transition height, h_{tr}, as function of the weighing in concentration, c_0 (in number of particles per volume). Data are shown for particles consisting of SiO_2, PS and $CaCO_3$, with sizes ranging from $50\,\mathrm{nm}$ to $25\,\mu\mathrm{m}$ dispersed in water and ethanol. Water and ethanol have different evaporation rates ($E_{water} = 0.7\,\mu\mathrm{m\,s^{-1}}$, $E_{ethanol} = 3.2\,\mu\mathrm{m\,s^{-1}}$, both at $1000\,\mathrm{rpm}$ (see thinning curves in the supplement). Thus they have different transition heights ($h_{tr,water} = 4.5\,\mu\mathrm{m}$, $h_{tr,ethanol} = 8.0\,\mu\mathrm{m}$). Therefore, for a meaningful comparison of the observed Γ of these different systems and, in particular for a comparison with the theoretically expected coverages, Γ has been scaled by h_{tr} [29, 32]. The dashed line depicts the Γ that is expected from the zero-order approach according to Eq. 6.1 with constant E and K. Fig. 6.3 (A) shows the data for various different types of particles and the two liquids for particle sizes up to $2.6\,\mu\mathrm{m}$ in diameter. Fig. 6.3 (B) shows results for particle diameters of 6, 8 and $25\,\mu\mathrm{m}$. Fig. 6.3 (A) reveals that except in the case of the big particles, the observed coverages are in excellent agreement with the coverages predicted by Eq. 6.1. It should be noted that in the case of the $CaCO_3$ particles the error margins are much larger than for the other particles because of the large variation in particle size leading to the somewhat indirect determination of the coverage as described above. Fig. 6.3 (B) reveals that for the large particles the observed coverage is significantly larger than expected from the zero order approximation calculated according to Eq. 6.1.

6.2.3 Universal plot of Γ as function of the particle sizes

Fig. 6.4 shows the comparison between the experimentally measured coverages and the coverages calculated according to Eq. 6.1 for all samples investigated. The data are plotted in a way, which explicitly discloses the particle size as a key parameter. It can be seen that irrespective of the particle material or size, the liquid material, or the weighing in concentrations, the experimental results match the zero-order predictions as long as the particle size is small enough. Small enough means less than a few microns in diameter. The threshold for deviations from the predictions is in the range of the transition height h_{tr}. This is depicted in the plot through the vertical dashed line at $d_p^3 = (2R)^3 = h_{tr}^3$ (Fig. 6.4 shows h_{tr} of ethanol, because the $8\,\mu\mathrm{m}$ PS particles dispersed in ethanol are the smallest particles, which deviate markedly from the zero order prediction).

6.3 Discussion

6.3.1 Limits of the zero-order approach: Rheology

Fig. 6.4 indicates that the approach of calculating the coverage according to Eq. 6.1 is correct as long as the particle diameters, d_p, are smaller than h_{tr}. For $d_p > h_{tr}$ the observed coverage is significantly larger than predicted. This may be explained as follows: If the particle

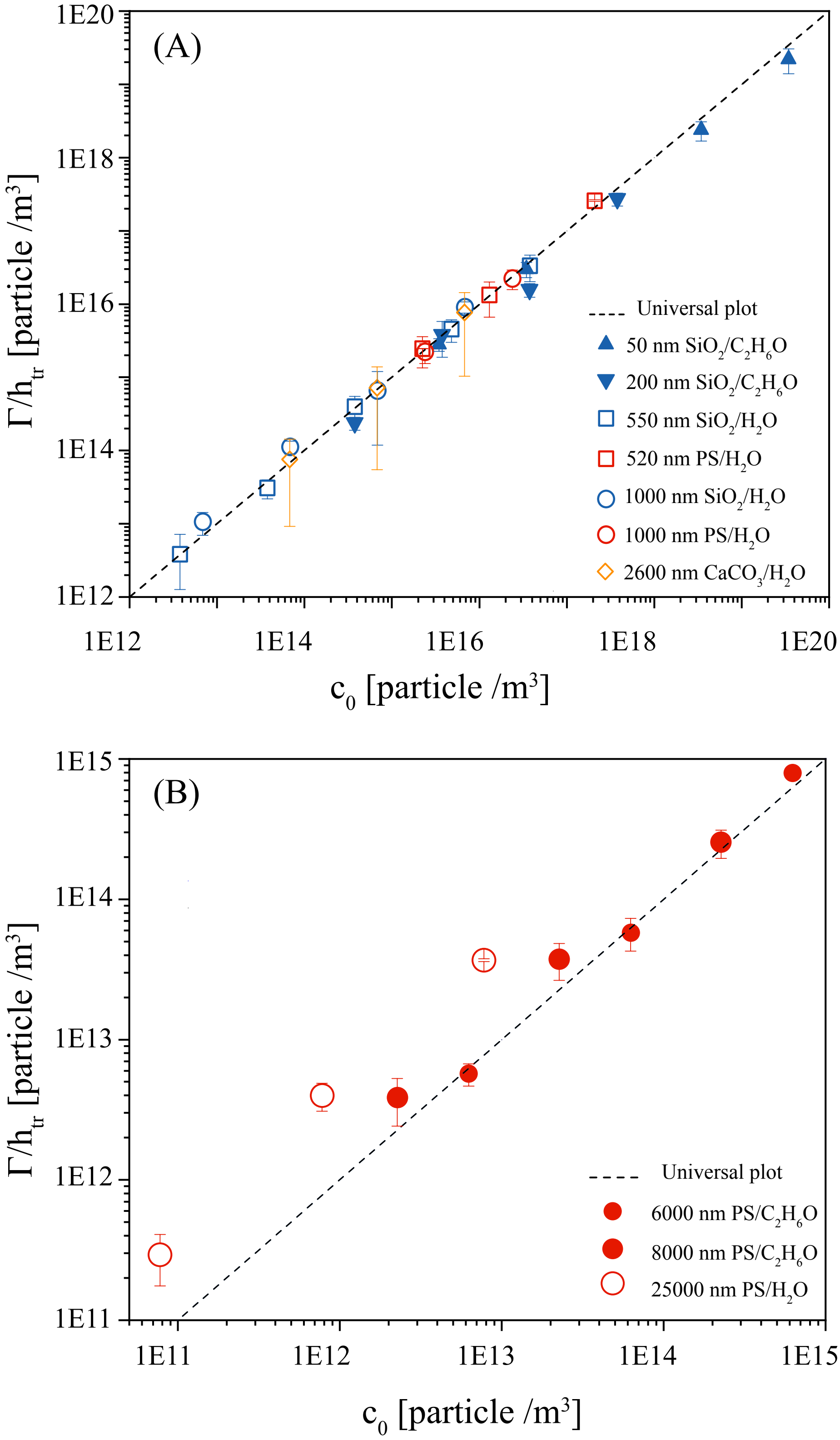

FIGURE 6.3: Final coverage Γ (in number of particles per area), scaled by the transition height, h_{tr}, as function of the initial concentration, c_0 (in number of particles per volume). Data are shown for particles consisting of SiO_2, PS and $CaCO_3$, with sizes, panel (A) ranging from 50 nm to 2600 nm, and panel (B) from 6000 nm to 25 000 nm, dispersed in water (open motif) and ethanol (close motif). Evaporation rates E and transition heights h_{tr} for $\omega = 1000\,\mathrm{rpm}$: $E_{water} = 0.7\,\mu\mathrm{m\,s^{-1}}$; $E_{ethanol} = 3.2\,\mu\mathrm{m\,s^{-1}}$; $h_{tr,water} = 4.5\,\mu\mathrm{m}$; $h_{tr,ethanol} = 8.0\,\mu\mathrm{m}$.

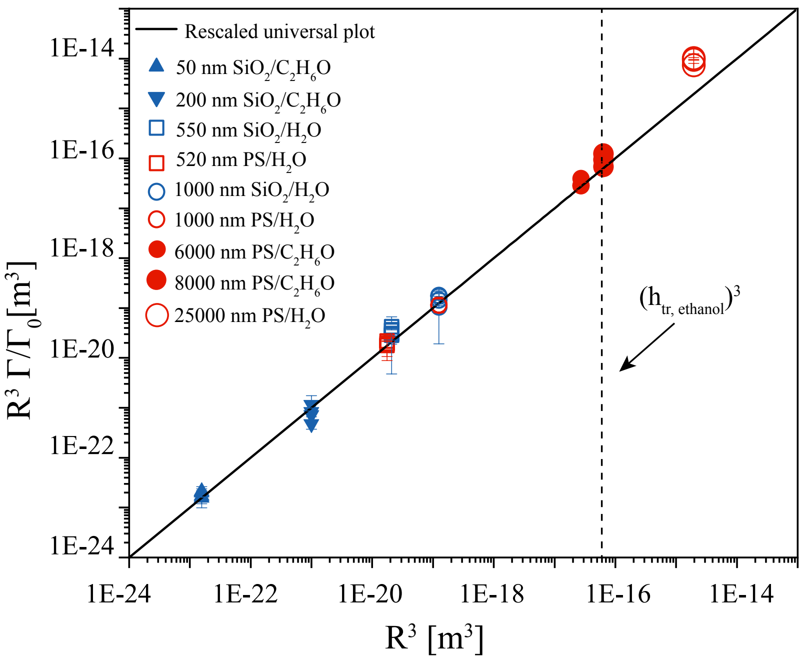

FIGURE 6.4: Ratio between measured coverages (Γ) and calculated coverages (Γ_0) multiply by the particle radii cubed, R^3, as function of the particle radii cubed, R^3. The solid line (slope one) indicates where Γ = Γ_0. The dashed vertical line marks R^3 $= h_{tr,ethanol})^3$, where the cube of the particle diameter is equal to the cube of the transition height of ethanol.

diameter is larger than h_{tr}, the assumption that a film of thickness h_{tr} contains a particle concentration equal to the weighing in concentration is not correct. The zero-order scenario assumes that the liquid film containing the dispersed particles is thinning through hydrodynamic (centripetal) flow until it reaches h_{tr}. Until the film thickness reaches h_{tr} the particle concentration remains constant, because liquid and particles flow radially outward. Around h_{tr} the hydrodynamic thinning becomes negligible. Evaporation starts to dominate and the particle concentration increases. However, with sufficiently large particles i.e., $d_p > h_{tr}$, this is not correct any more. In this case, as soon as the film thickness h is equal to d_p *all* particles within a film will contact the substrate (the film thickness, h, is here defined as the mean height of liquid per area). Thus all particles that are in the film of thickness d_p are approximately immobilized and will finally be deposited So, in the case of $d_p > h_{tr}$ a rather crude approximation predicts:

$$\Gamma_{d_p}(d_p > h_{tr}) \approx c_0\, d_p = c_0\, \frac{d_p}{h_{tr}}\, (E/2K)^{\frac{1}{3}}. \tag{6.2}$$

The data of Fig. 6.4 show that for the aqueous dispersion of PS particles with diameters of d_p = 25 µm the observed coverage Γ is about 5 times larger than what is predicted as Γ_0 i.e., if particle size is not taken into account. If $d_p > h_{tr}$ however is taken into account according to Eq. 6.2 (with $h_{tr} \approx 4.5\,\mu$m), the predicted coverage is ≈ 5-6 fold higher in agreement with the experimental findings.

With the optical microscopy set-up is possible to the influence of d_p and h_{tr} on the particle movement and coverage. Fig. 6.5 shows the case of aqueous dispersions ($h_{tr} = 4.5\,\mu$m) of PS particles with A) $d_p = 25\,\mu$m ($c_0 \sim 7.8 \times 10^{11}\,$particles/m^3) and B) $d_p = 1\,\mu$m ($c_0 \sim 2.4 \times 10^{14}\,$particles/m^3). The images show that in the case of the big particles with d_p= $25\,\mu$m $>> h_{tr}$ the number of particles per area decreases as long as $h > d_p$. As soon as

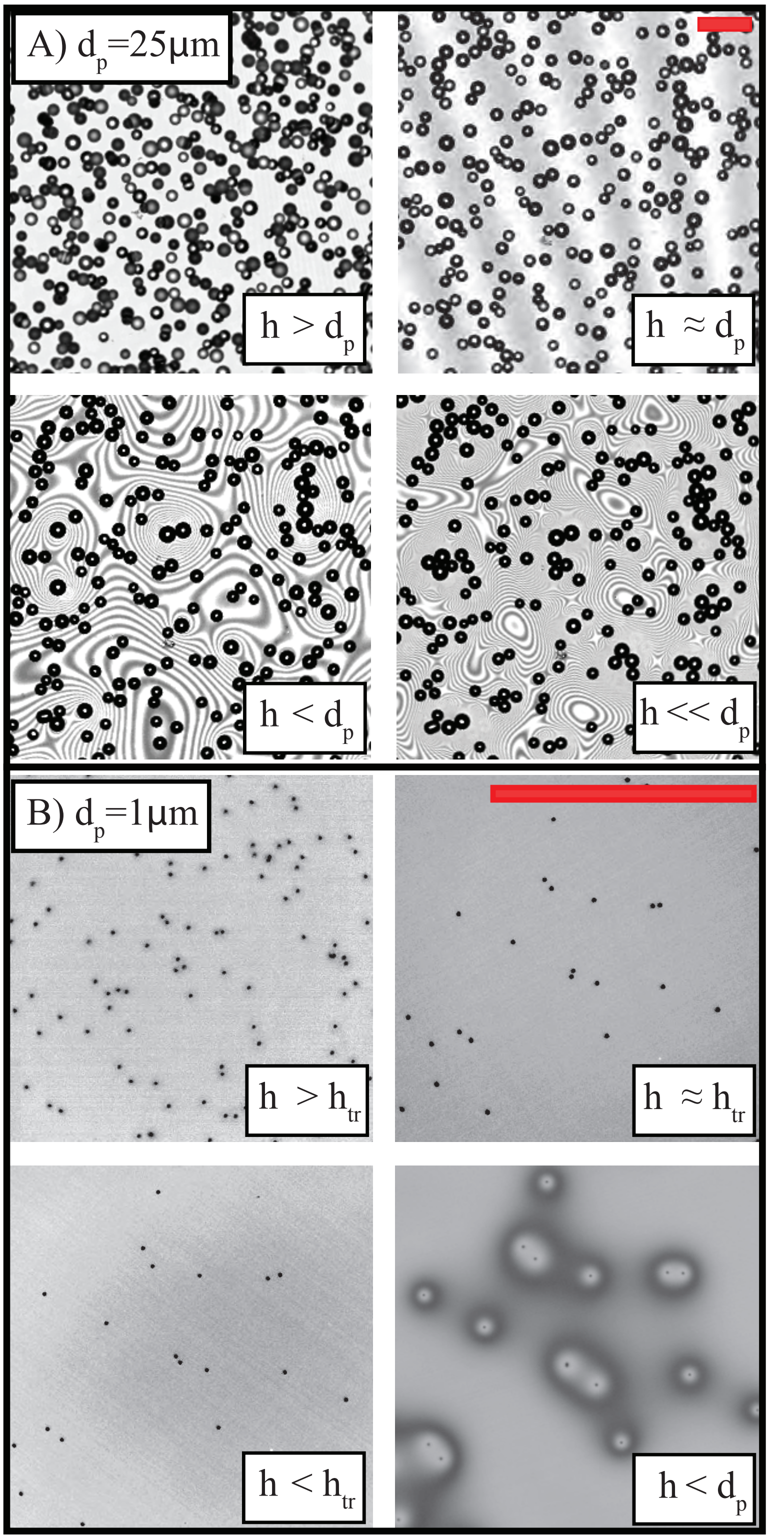

FIGURE 6.5: Sequence of optical images recorded during the spin casting ($\omega = 1000\,\mathrm{rpm}$, the bar indicates $100\,\mu\mathrm{m}$) of aqueous dispersions of PS particles with A) d_p=25 µm ($c_0 \sim 7.8 \times 10^{11}\,\mathrm{particles/m^3}$) and B) d_p=1 µm ($c_0 \sim 2.4 \times 10^{14}\,\mathrm{particles/m^3}$). h = liquid film thickness = the mean volume of liquid per area. With the big particles, as long as $h > d_p$, the number of particles per area decreases, for $h < d_p$, it remains about constant. With the small particles, the number of particles per area decreases as long as $h > h_{tr}$. For $h < h_{tr}$ (h_{tr}=4.5d_p) and $h < d_p$ it remains constant. In both cases, for $h < d_p$ the liquid surface gets distorted (interference fringes).

$h \approx d_p$, the number of particles per area barely decreases any more. All particles contained in the film of thickness $h \approx d_p$ are finally deposited as described by Eq. 6.2. The interference fringes indicate that the film surface is flat for $h > d_p$ and becomes undulated for $h < d_p$. The parallel interference fringes at $h \approx d_p$ show that it is flat, but very slightly inclined with $<< 1\,\mathrm{deg}$. In the case of the particles with $d_p = 1\,\mu\mathrm{m} << h_{tr}$ the particle density decreases as long as $h > h_{tr}$ and remains approximately constant if $h < h_{tr}$. The final surface coverage is determined by Eq. 6.1.

6.3.2 Limits of the zero-order approach: Sedimentation

Figures 6.5 and 6.4 and Eq. 6.2 indicate that the particle size has a direct influence on the final coverage due to the direct interaction between the hydrodynamic-evaporative film thinning on the particle concentration. What about the combined impact of particle size and particle density i.e., sedimentation? For Eqs. 6.1 and 6.2 it is assumed that the composition within the spreading drop right after deposition and within the layer thinning due to hydrodynamics down to d_p or h_{tr} remains constant and equal to the weighing in value c_0. With strong sedimentation this may be wrong. As soon as the spin cast process begins, through sedimentation particles continuously move to the substrate surface and accumulate/attach there. Thus sedimentation can lead to a final Γ, which is higher than predicted by Eq. 6.1. The extra amount of Γ resulting from sedimentation, $\Gamma_{\overline{\Delta\rho}}$, may be estimated as follows: The speed of sedimentation, $u_{\overline{\Delta\rho}}$, as function of the relative particle density $\overline{\Delta\rho}$, is given by[124]:

$$\begin{aligned} u_{\overline{\Delta\rho}} &= \frac{g}{18\nu} \cdot \frac{\rho_P - \rho_L}{\rho_L} \cdot d_p^2 \\ &= \frac{g}{18\nu} \cdot \overline{\Delta\rho} \cdot d_p^2. \end{aligned} \tag{6.3}$$

g is the gravitational acceleration ($9.8\,\mathrm{m\,s^{-1}}$) and ν is the kinematic viscosity. Sedimentation leads to a continuous deposition of particles at the substrate surface within a time $t_{\overline{\Delta\rho}}$ of:

$$\begin{aligned} \Gamma_{\overline{\Delta\rho}} &= c_0 \cdot u_{\overline{\Delta\rho}} \cdot t_{\overline{\Delta\rho}} \\ &= c_0 \cdot \frac{g}{18\nu} \cdot \overline{\Delta\rho} \cdot d_p^2 \cdot t_{\overline{\Delta\rho}}. \end{aligned} \tag{6.4}$$

For Eq. 6.4 it is assumed that particles reach the substrate and get deposited as they move downwards with speed $u_{\overline{\Delta\rho}}$ during time $t_{\overline{\Delta\rho}}$.

In the following, it is assumed that the sedimenting particles are smaller than h_{tr}. Therefore, sedimentation accumulates particles during $t_{\overline{\Delta\rho}} = 0.3 t_{sc}$ i.e., the time *before* the film reaches h_{tr} (see Eq. 10.3):

$$\begin{aligned} \Gamma_{\overline{\Delta\rho}} &\approx c_0 \cdot \frac{\overline{\Delta\rho} g}{18\nu} \cdot d_p^2 \cdot 0.3 t_{sc} \\ &\approx c_0 \cdot \frac{\overline{\Delta\rho} g}{18} \cdot d_p^2 \cdot \frac{1}{2}(2E^2K)^{-\frac{1}{3}} \\ &= c_0 \cdot \frac{\overline{\Delta\rho} g}{36\nu E} \cdot d_p^2 \cdot h_{tr}. \end{aligned} \tag{6.5}$$

For a rough estimation, is consider that sedimentation plays a significant role, as soon as it contributes as much to the final coverage as the *regular* deposition process. Thus Eqs. 6.1 and 6.5 yield:

$$c_0 \cdot h_{tr} = c_0 \cdot \frac{\overline{\Delta\rho} g}{18\nu} \cdot d_p^2 \cdot \frac{h_{tr}}{2E}. \tag{6.6}$$

This yields a diameter of d_{tr} for the transition between deposition dominated by evaporation and sedimentation:

$$d_{tr} = \sqrt{\frac{36\nu E}{\overline{\Delta\rho} g}}. \tag{6.7}$$

With Eq. 2.16 this equation can be written as a function of h_{tr}:

$$d_{tr} = \sqrt{\frac{24\omega^2}{g}} \cdot (\overline{\Delta\rho})^{-1/2} \cdot h_{tr}^{3/2}. \tag{6.8}$$

Eq. 6.8 evaluates the significance of the contribution of sedimentation as function of $\overline{\Delta\rho}$ and in particular of h_{tr}, the key parameter of any spin cast process. Let us assume that a dispersion with particles of relative density $\overline{\Delta\rho}$ is spin cast at a rotation speed ω and with a transition height h_{tr}. Eq. 6.8 says that if the particle diameter is smaller than d_{tr}, then contributions of sedimentation to Γ can be neglected. If they are larger than d_{tr}, sedimentation plays a role.

If the particles are smaller than h_{tr}, but larger than d_{tr} (i.e., no direct size effect, but sedimentation plays a role), as a first approximation, one may combine Eqs. 6.1 and 6.5 and assume:

$$\begin{aligned}
\Gamma &\approx \Gamma_0 + \Gamma_{\overline{\Delta\rho}} \\
\Gamma &\approx c_0 \cdot h_{tr} + c_0 \cdot \frac{\overline{\Delta\rho} g}{18\nu} \cdot d_p^2 \cdot \frac{h_{tr}}{2E} \\
\Gamma &\approx c_0 h_{tr} \Big[1 + \frac{\overline{\Delta\rho} g}{36\nu E} d_p^2\Big].
\end{aligned} \tag{6.9}$$

Fig. 6.6 sums up the analysis regarding the impact of size and sedimentation on the final coverage. It reveals in an overview plot under which spin cast conditions the final coverage of particles, Γ, can be described reasonably well either by

1.) the zero-order approximation (Eq. 6.1), or when it needs corrections due to;

2.) size effects (Eq. 6.2) and/or

3.) sedimentation (Eq. 6.9).

Fig. 6.6A shows the general relations between the various parameters for $\omega = 1000\,\text{rpm}$. Fig. 6.6B shows how the plot is used to estimate the deposition behavior of a specific dispersion. Both figures show a plot of $\overline{\Delta\rho}$ versus h_{tr}, covering their practically useful ranges. The dashed straight line computed from Eq 6.7, which is inclined at about $15°$, is the borderline for the pure size effect. It marks d_{tr} = h_{tr}. For spin cast conditions that are located below this line the particle size, d_{tr}, is larger than h_{tr}. In this case the final coverage should be estimated by Eq. 6.2. Sedimentation is affected by size and $\overline{\Delta\rho}$ and cases located above the dashed line may or may not be affected by sedimentation. Relevant for an estimation of the contribution from sedimentation are the dotted, parallel lines, inclined at about $40°$ (calculated by Eq. 6.7), marking specific particle diameters.

How particle size and specific spin cast conditions are taken into account is demonstrated with examples of three particles sizes of 1, 8, and $25\,\mu\text{m}$ in diameter in Fig. 6.6B (indicated by the red crosses). An aqueous dispersion of PS particles is assumed. This means as specific conditions $h_{tr} = 4.5\,\mu\text{m}$ (the vertical dashed blue line) and $\overline{\Delta\rho} = 0.3$ (the horizontal dashed red line). The crossover between these two conditions and the corresponding particle size, d_{tr} (dotted lines) identifies the transition diameter for particles under these conditions. According to Fig. 6.6B, it is obtain for this case $d_{tr} \approx 2.8\,\mu\text{m}$. This means that for particles, which are smaller than $2.8\,\mu\text{m}$ and spin cast under these conditions, sedimentation can be neglected for the calculation of Γ. If they are bigger, sedimentation contributes to Γ. Hence, for instance, the final coverage for particles with a diameter of $1\,\mu\text{m}$ can be calculated

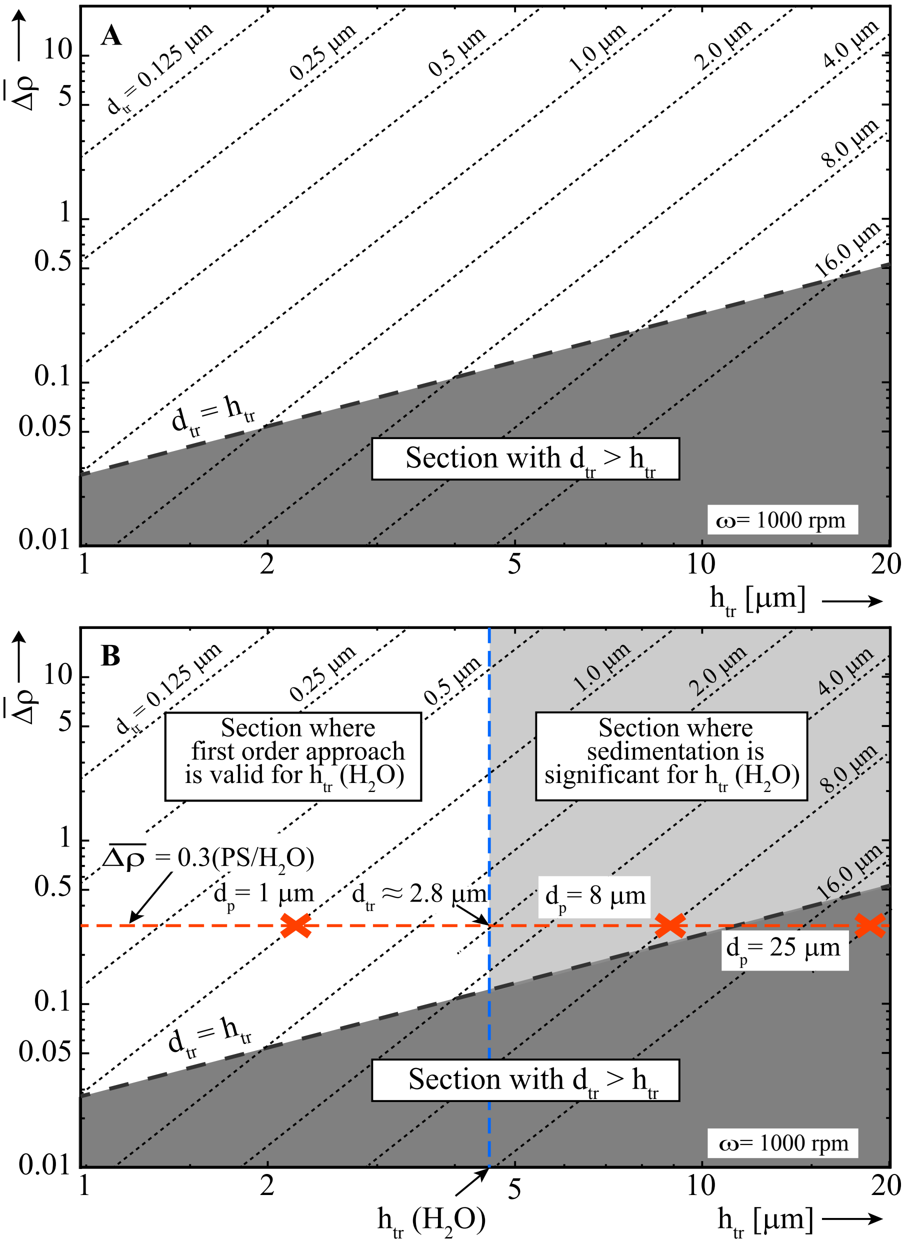

FIGURE 6.6: Threshold of the particle size (d_{tr}) deposited from spin casting, as function of the relative density $\overline{\Delta\rho}$ and the h_{tr}, the fine dash lines ($\approx 40^\circ$) are calculated by in Eq.6.8 for $\omega = 1000\,\mathrm{rpm}$, represent the particle diameter were the film thinning equalizes the sedimentation speed (Eq. 6.6) for a given system; to the left side the sedimentation can be neglected, for bigger particles (to the right of the specific dash line) is expected that sedimentation plays a role and a deviation from the prediction by excess. The dash blue line marks the h_{tr} for water, they represent the ultimate limit for Eq. 6.1 respect to de particle size is $d_p = h_{tr}$, where the dash thick line ($\approx 15^\circ$) cuts the discontinue ones, to the left side of the h_{tr} is the working, to the right of the h_{tr} Eq.6.1 is not valid any more. On panel B the condition of an aqueous dispersion of PS particles is marked with a red dash line; experimentally tested particle sizes are marked with red crosses over the three plot regions.

with the zero order approximation (Eq. 6.1). For the final coverage of particles with a diameter of $8\,\mu\mathrm{m}$, on the other hand, sedimentation should be considered (Eq. 6.9). For particles with a diameter of $25\,\mu\mathrm{m}$, sedimentation and the pure size effect (their diameter is larger than h_{tr}) has to be considered. This means Eq. 6.2. Eq. 6.9 is not correct in this case, because the time during which sedimentation adds to Γ is shorter than t_{tr} (because $d_p > h_{tr}$). In this case one could estimate the contributions of size (Eq. 6.9) and sedimentation (Eq. 6.2, assuming t_{tr}) separately, and chose for a correction of Γ whatever correction is larger.

It should be noted that the particle sizes of 1 and $25\,\mu\mathrm{m}$ depicted in Fig. 6.6B reflect the real cases presented in the experimental section (Fig. 6.4). On the other hand, the conditions for the PS particles with d_p= $8\,\mu\mathrm{m}$ presented in the experimental part were significantly different. Ethanol, which was used as liquid instead of water has a much larger h_{tr} ($\approx 7.5\,\mu\mathrm{m}$). This corresponds to $d_{tr} \approx 6\,\mu\mathrm{m}$. Therefore, in this case the contribution from sedimentation to Γ is relatively weak. In fact, Fig. 6.3 shows that Γ for these particles is only slightly larger than what is predicted in the zero order approach.

6.4 Summary and Conclusion

The deposition of nano and micron size spherical particles dispersed in volatile liquids is investigated as function of the weighing in concentrations, the particles size, and the densities of liquid and particles. The particles are deposited by hydrodynamic evaporative spin casting. The deposition process is investigated on line optically during the spin cast process and the final particle coverage is measured. The data are analyzed in view of the zero-order approach. This approach assumes a simple hydrodynamic evaporative behavior of the liquid only, without taking into account any impact of the dispersed particles. It has been used successful to describe the deposition of monomer and polymer films. For particle dispersions, was found that the zero order approach works quantitatively quite well for particle sizes up a few microns in diameter. For larger particles the observed final coverage exceeds the predicted value significantly.

The causes for this deviation were found and analyzed. A theoretical approach is presented, which describes the impact of the particle size and the particle weight on the final particle coverage. It is suggested that large particles have an impact on the transition between hydrodynamic and evaporative film thinning and thus on the outcome of the deposition process. Sedimentation of particles may also contribute to the final coverage, if the particle density is significantly larger than the density of the liquid and if the particles are big enough. In addition, It is offered a new approach, which takes size and/or sedimentation effects into account. This permits the prediction of the final particle coverage even for rather large and/o heavy particles. The theoretical predictions are in agreement with the experimental results.

Chapter 7

Liquid Thin Film Shape Around Nanoparticles

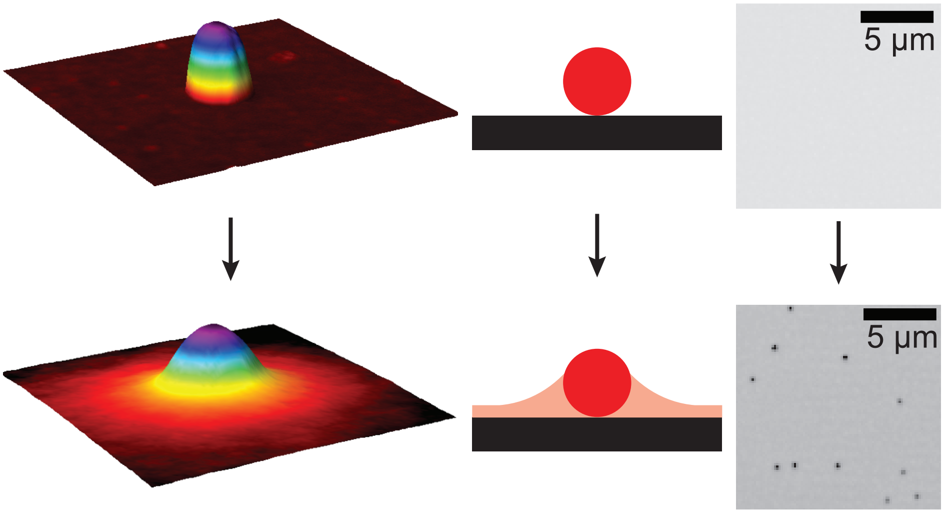

FIGURE 7.1: Meniscus distortion around nanoparticles

The content of this chapter has been published as: “Meniscus shape around nanoparticles embedded in molecularly thin liquid films”. In: *Langmuir* 34.38 (2018), pp. 11364–11373 J. Danglad-Flores, S. Eickelmann, and G. Chen performed the experiments and contributed equally. J.D.-F. performed the AFM measurements and did the theoretical analysis and numerical fit of the meniscus data obtained by AFM and optical microscopy, providing Fig 6 and 7 and partially Fig 5. S. Eickelmann focused on the microscopy imaging. He worked on image processing and translated the optical raw data into film thickness. G. Chen. also performed some of the optical microscopy experiments, synthesized and characterized the nanoparticles. Miettinen M. S. worked on the theoretical background of the meniscus shape. H.R. organized and supervised the research, wrote the manuscript, and contributed to the data analysis and interpretation. All authors have discussed the results, read the manuscript, and agreed with its content.

7.1 Introduction

Small objects embedded in thin films are ubiquitous in nature [125–130]. They are a topic in basic research [131–136] and proposed as well as used for applications [137–141]. If the particles are larger than the film thickness, they "stick out". Therefore they will distort the adjacent film surface (cause a "meniscus"). The geometry of this meniscus is of interest in applied and fundamental science, because it reflects the interactions between the particle and its environment and is a measure/cause for the interaction between neighboring particles. Therefore the meniscus geometry is an important system parameter.

For micrometer-sized and larger systems meniscus shapes have been investigated experimentally and theoretically [142–145]. For smaller i.e., truly nanometer-size systems, with particle diameters and really thin films (thicknesses $\ll 1\,\mu\mathrm{m}$), meniscus geometries have been studied experimentally up to now only for solid systems. For instance, systems with particles embedded in polymeric films were imaged by atomic force microscope (AFM)[146–149], scanning electron microscopy (SEM)[146, 150] or with confocal optical methods[151–157]. In these cases the meniscus geometries were affected by the solidification process. They may not reflect the equilibrium situation of the particles embedded in the mobile/liquid film. This case, meniscus shapes in the vicinity of nano-size particles embedded in very thin liquid (mobile) films, has not been investigated up to now. The shape of the meniscus of a liquid film adjacent to a nanoparticle (NP) is still unknown. It is still unknown how it depends on particle size, on film thickness, on film properties (surface tension), on substrate properties, etc.

If the size of NPs is well below the resolution limit for visible light (Rayleigh limit [158]), their *imaging* is impossible with conventional optical microscopy. It has been shown however, that it is possible to identify the *location* of nano size objects with conventional optical microscopy through their refraction/diffraction signature e.g., by the "caustics" caused by surface distortions [159]. The optical diffraction signature is usually weak but it can be enhanced by sophisticated image processing (oversampling, background subtraction, contrast enhancement, etc. [35]). Slight defocussing along the optical axis[160–163] may also enhance the diffraction signal in particular with particles embedded in thin films[159, 164].

In the following NPs embedded in a molecularly thin liquid film will be studied, the distortion of the liquid film around the nanoparticles and to *quantitatively* measure the adjacent meniscus shape. We use a special setup of interference enhanced optical reflection microscopy. We determine the location of even very small NPs (diameters $\ll 100\,\mathrm{nm}$) embedded in liquid films. We measurer the meniscus shape as well as the far-field liquid film thickness with nm precision. We find that in comparison to the vertical scale the lateral scale of distortion reaches out further by orders of magnitude more.

7.2 Results

7.2.1 Optical footprints of NPs and their menisci in liquid films

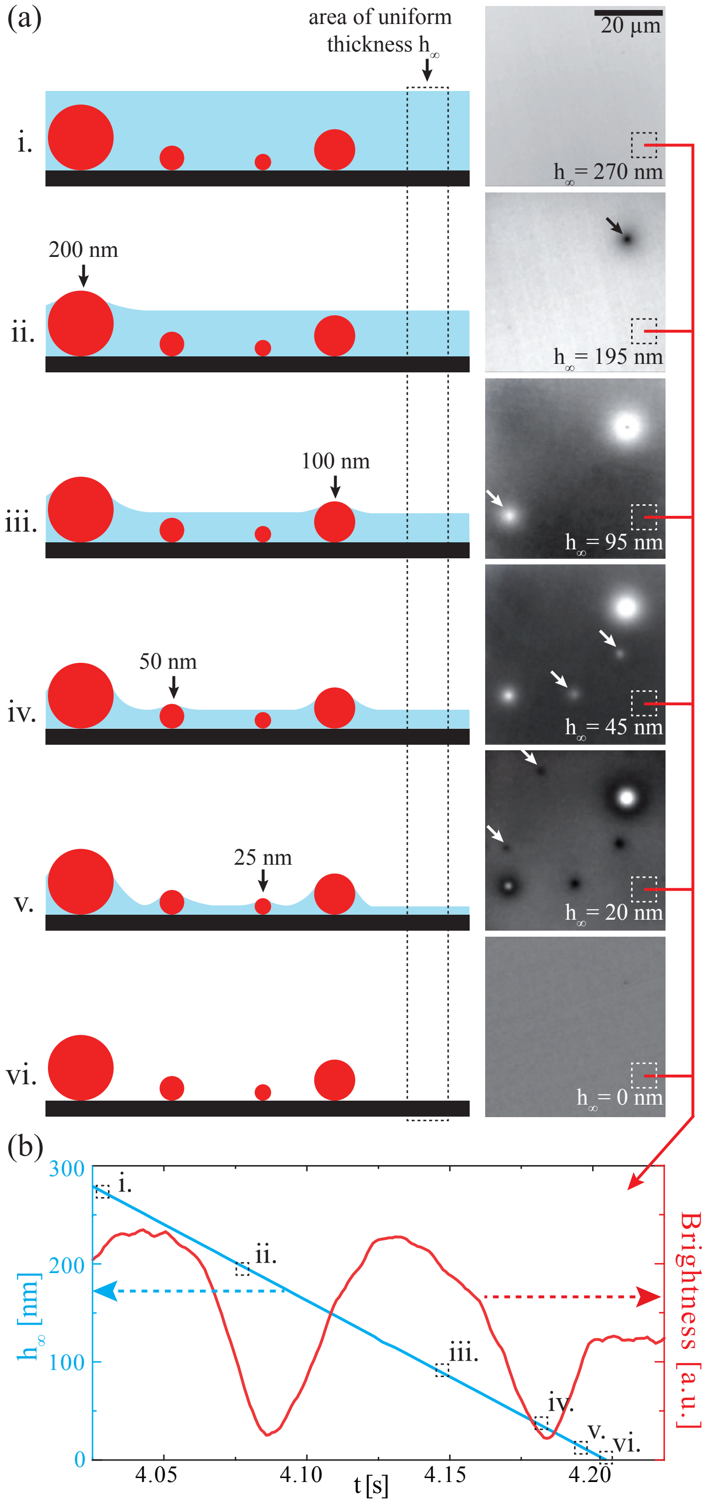

FIGURE 7.2: Snapshots of optical footprints of NPs embedded in a thinning toluene film. Attached to the substrate surface are individual NPs with diameters of $d_{NP} \approx 25, 50, 100$ and $200\,\mathrm{nm}$. The NPs are randomly distributed and laterally several tens of μms apart. (a) Images recorded at various far-field toluene film thicknesses, h_∞, and cartoons of the corresponding vertical film cross sections (not to scale laterally). (b) In red the brightness variation of far-field (planar) film sections with time (due to evaporation) and in blue their corresponding film thickness, h_∞.

Figure 7.2 (a) presents a sequence of interference microscopy snapshots, which were recorded during the evaporative thinning of a toluene film on a planar silicon wafer substrate. Figure 7.2(b) shows the time-dependent variation of the "Brightness" (gray level) as it is measured from a surface area with a planar film of uniform thickness (i.e., an area without NP). This signal is translated into a momentary "far-field" toluene film thickness, h_∞ i.e., a film thickness undisturbed by NPs.

The samples were prepared by first depositing a mixture of Platinum-Nanoparticles (NPs) with diameters d_{NP} of $\approx 25, 50, 100$ and $200\,\mathrm{nm}$ onto a planar silicon wafer sample via spin casting from an aqueous solution. The process conditions and NP-concentrations were adjusted [14, 29, 32] such that the average distance between individual NPs was in the range of several tens of microns. The data presented in Figure 7.2 were obtained during the evaporative thinning of a film of pure toluene i.e., during the spin casting of pure toluene onto the substrates with the NPs already deposited.

The snapshots of Figure 7.2 (a) reveal that at certain locations spots of locally different gray levels appear as soon as the film thickness has decreased to a certain value. The gray levels of the spots change as the film gets thinner. The spots remain and disappear only when the toluene has evaporated completely [a]. AFM and optical investigations on the lateral arrangements and the surface coverage of the NPs on the dry samples prove that individual NPs are the origin of the spots i.e., the observed local gray level variations. The cartoons next to each microscopy image suggest the vertical cross-sections through the liquid films including the NPs. [b].

7.2.2 Optical footprints as a function of the far-field film thickness for different liquids

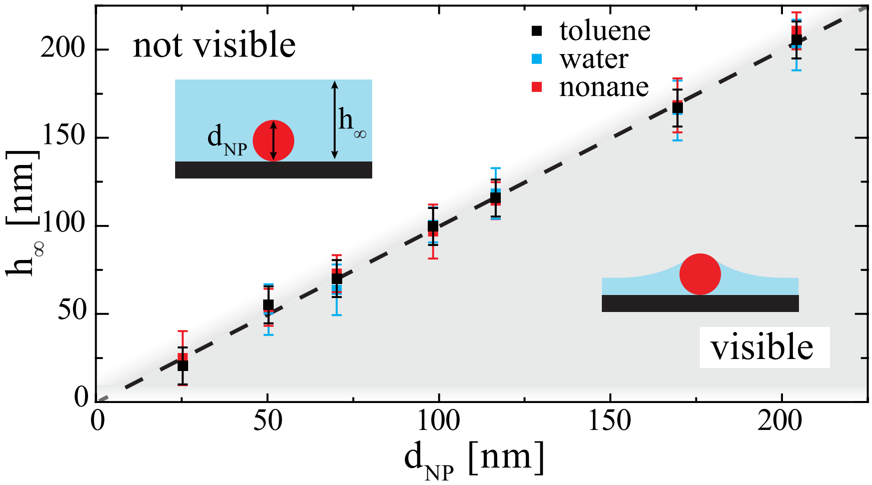

FIGURE 7.3: Region where NP footprints are not observed ("not visible") and where footprints are detected ("visible") as function of the NP size d_{NP} and of the far-field film thickness h_∞ for various liquids (toluene, water and nonane). The dashed line marks $h_\infty = d_{NP}$. The Pt-NPs had diameters of $25, 50, 70, 100, 120, 170$ and $200\,\mathrm{nm}$.

---

[a] Spots from the largest NPs with diameters of $200\mathrm{nm}$ are still faintly visible even with completely dry substrates.

[b] Please note that in the cartoons of Figure 7.2 (a) the lateral and vertical scales are different by about a factor of 100 to enable a reasonable visualization of the NPs and their environment.

Figure 7.3 presents results from optical imaging of substrates during the evaporative thinning of films of various liquids (toluene, water, and nonane) that were deposited on substrates with individual NPs of different diameters d_{NP} attached to them. The data are based on measurements analoguous to those presented in Figure 7.2. The Figure shows the range where local optical footprints caused by NPs are observed as a function of the NP size, d_{NP}, and of the far-field film thickness, h_{∞}. The figure shows that optical footprints of the NPs are only visible if there is a liquid film with $0 < h_{\infty} \leq d_{NP}$. For dry samples and for $h_{\infty} > d_{NP}$ optical footprints such as those presented in Figure 7.2 are not observed.

7.2.3 Meniscus profiles derived from the local gray levels

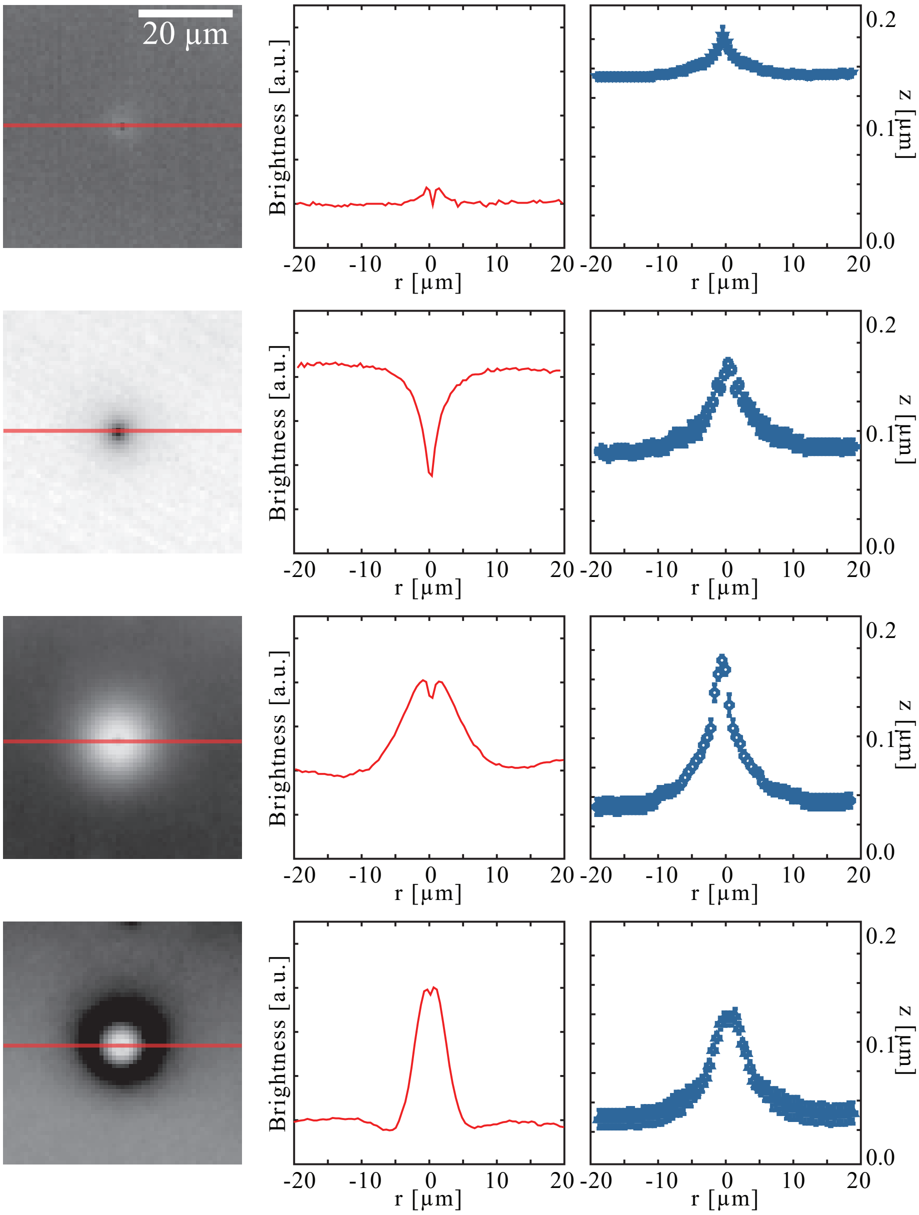

FIGURE 7.4: Translation of optical footprint data into meniscus geometries. Depicted is the case of an individual NP ($d_{NP} = 200\,\mathrm{nm}$) embedded in toluene films of different thicknesses. Left column: Optical reflection images at film thicknesses $h_\infty = 150, 90, 50,$ and $20\,\mathrm{nm}$. Middle column: Gray level variations along lines through the center of the NP. Right column: Translation of the gray levels of individual camera pixels into the local film thickness. Assumed is the same relation between gray level and film thickness as for planar film sections.

Figure 7.4 presents the translation of the optical footprint (locally varying gray levels) caused by a NP into the geometry of the surrounding meniscus. The NP with a diameter of $200\,\mathrm{nm}$ is embedded in toluene films with far-field thicknesses of $h_\infty = 150$, 90, 50, and $20\,\mathrm{nm}$. The column on the left shows the optical images. The column in the middle presents the gray level variations on a line through the center of the location of the NP. The right column depicts the meniscus geometry as it has been derived from the gray level variations. For the derivation of the meniscus profiles it is assumed that the imaged gray level can directly be translated into the local film thickness of the imaged spot (see Figure 7.2(b) and Methods section). Even though the diameter of the NP is much less than $1\,\mu\mathrm{m}$, the meniscus profiles extend up to $\approx 10\,\mu\mathrm{m}$ away from the location of the NP (the lateral and the vertical scales of the plots of Figure 7.4 are different by about two orders of magnitude). The plots show that the optically measured height in the center at $x = 0$ does not match the (known) height of the NP. It is different for different h_∞, decreasing from about $180\,\mathrm{nm}$ for $h_\infty = 150\,\mathrm{nm}$ to about $120\,\mathrm{nm}$ for $h_\infty = 20\,\mathrm{nm}$. This is an optical artifact. The lateral extension of the NP is smaller than the diffraction limit. The data indicate that a one-to-one translation of the gray levels of individual pixels into a corresponding local film thickness is a crude approximation, which may be quantitatively wrong. Therefore the validity of such an analysis has to be investigated. This is done in the following section by a comparison between optical and AFM data.

7.2.4 NPs embedded in solid polymer films

Figure 7.5 presents a comparison between AFM and optical microscopy data of the same sample location with NPs embedded in solid polymer films. Individual NPs were first deposited on a planar silica/silicon substrate. Then thin polystyrene (PS) films were spin cast onto these samples from a polystyrene/toluene solution. The optical and the AFM investigations were performed after complete evaporation of the solvent. Cases (a) and (b) show NPs that are embedded in the PS film. In case (c) the NP embedded in a PS film was removed before the investigation. The figure shows the AFM data (false colour images and height profiles) and optical imaging data (gray level images and interferometrically derived height profiles (see Figures 7.3 and 7.4)). The lateral scale is so small that individual camera pixels of uniform gray levels can be identified in the optical images. Nevertheless, the lateral scaling is still much larger (μm) than the vertical one ($10\,\mathrm{nm}$), so that the spherical NPs (or their outline as in (c)) indicated in the figure by the gray area appear strongly elliptically distorted.

The data show that by and large the meniscus profiles measured by AFM and by optical interferometry match. Significant differences between the "true" (expected) and the measured profiles appear only within $200\,\mathrm{nm}$ from the NP (or from the center of its former location, as in case (c)). Most likely these differences around $x = 0$ are due to diffraction effects in the case of the optical imaging. Very close to the NPs the AFM data may also not reflect the true shape of the surface topography due to the conical shape of the AFM tip (tip convolution effect). In the case of Figure 7.5(c) a NP of $70\,\mathrm{nm}$ diameter was removed after the polymer film formation. This can clearly be seen from the AFM data, whereas the optical data do not reveal the crater-like shape of the surface.

The data depicted in Figure 7.5 reveal two important features:

1.) For comparable NP sizes and far-field film thicknesses the lateral range of the meniscus distortion is significantly smaller for the solid polymer films than for liquid films of pure solvents (see Figure 7.4). This indicates that polymer enrichment in the course of the solvent evaporation during film formation affects the final meniscus shape.

2.) The geometrical meniscus profiles measured by AFM and by optical reflection microscopy are virtually identical within the measurement errors (except for the center region very close to the NP). This means meniscus geometries derived from optical reflection microscopy images are quantiatively correct except for a region of about $0.5\,\mu\mathrm{m}$ around the location of the NP.

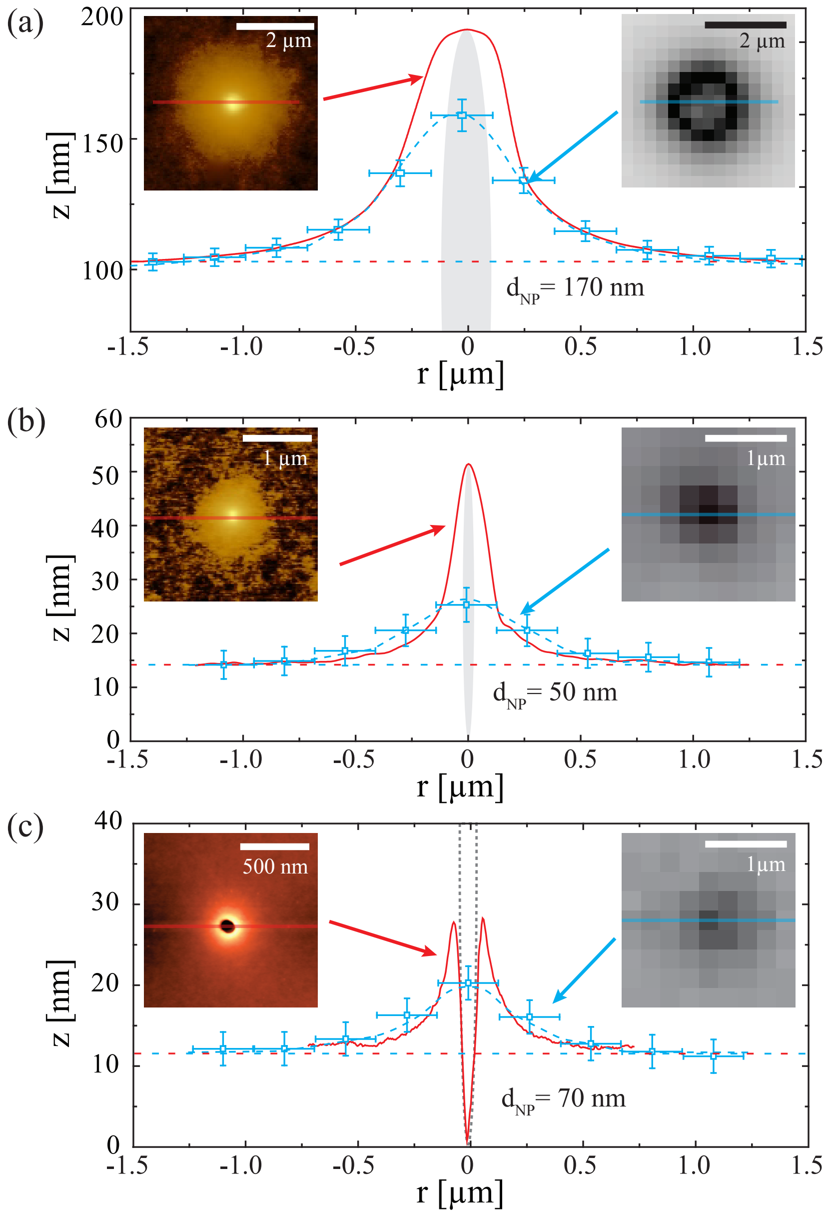

FIGURE 7.5: Comparison between the optical and the AFM signatures of NPs embedded in PS films with a) a NP of 170 nm in diameter ($h_\infty = 100\,\mathrm{nm}$) and b) of 50 nm diameter ($h_\infty = 15\,\mathrm{nm}$).c) the 70 nm NPs embedded in a PS film ($h_\infty = 12\,\mathrm{nm}$) were removed before AFM investigation. The gray ellipsoid represents the spherical NPs. The optical signatures (blue data points) were derived from the gray levels in a zero-order approach (see main text). The blue dashed line is a guide to the eye. The AFM signature (in red) was obtained by tapping mode.

7.2.5 Meniscus geometries

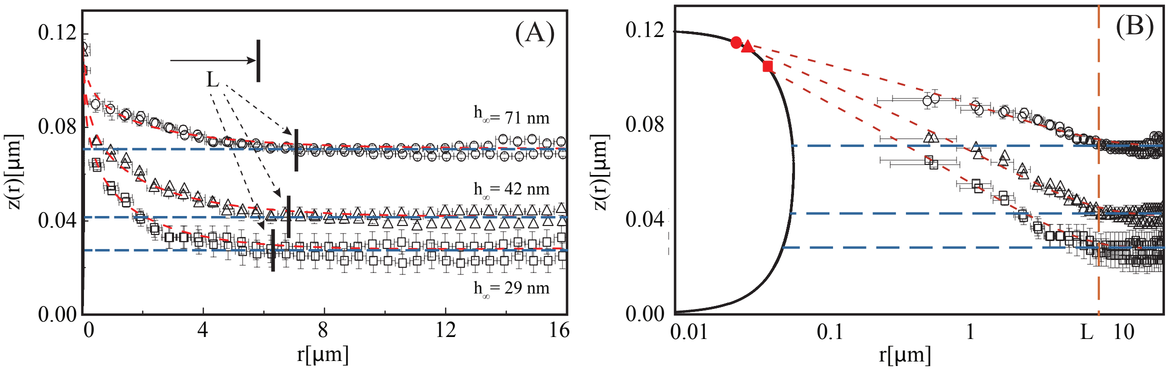

FIGURE 7.6: Meniscus geometries derived from optical reflection microscopy. (A) Lin-lin-plot of the meniscus profiles around a NP with $d_{NP} = 120\,\mathrm{nm}$, embedded in toluene films of $h_\infty = 29\,\mathrm{nm}, 42\,\mathrm{nm}$, and $71\,\mathrm{nm}$ as indicated by the blue dashed lines. Each curve consists of two sets of data points (from both sides of the NP) The red dashed lines show a hyperbolic cosine fit of the data points. The vertical and horizontal scales are different by about a factor of 80. (B) Lin-log-plot of the data shown in (A).

Figure 7.6(A) presents experimental data of the geometry of the meniscus profiles in the vicinity of a NP with a diameter of $d_{NP} = 120\,\mathrm{nm}$. For a better visualization of the meniscus distortion the linear scalings of the horizontal and the vertical axes differ by a factor of 80 (the spherical NPs are plotted in scale and therefore appear distorted). The NP was embedded in toluene films with three different far-field liquid film heights, h_∞ = 29, 42, and $71\,\mathrm{nm}$ (indicated by the dashed blue lines). The two data sets depicted represent the profiles from either sides of the NP. According to the data the meniscus reaches out as far as $\approx 5\,\mu\mathrm{m}$ away on both sides from the NP. Figure 7.6(B) shows the same data in a lin-log plot. The linear behaviour reveals a logarithmic meniscus profile within most of the meniscus range.

In Chapter 2 (Figure 2.2) was presented the schematic of the cross section through the NP and the film/meniscus in the vicinity of the NP was shown . As well, Figure 2.2 presents the definitions of the various parameters that are used to fit the experimental data. It turns out that all meniscus shapes can be fitted quite well by a combination of a logarithmic (hyperbolic cosine)[49] and an exponential decay as follows.

Surface Shape

The meniscus shape of the liquid film distorted by a cylinder is described by the following catenary curve [49].

$$r(z) = r_i \cdot \cosh\left(\frac{z - h_i}{r_i}\right). \tag{7.1}$$

The Eq.7.1 in its exponential form (Eq. 7.2) can be solve as an expression for z(r):

$$u = \frac{e^w + e^{-w}}{2}. \tag{7.2}$$

Where

$$u = \frac{r(z)}{r_i}. \tag{7.3}$$

$$w = \frac{z - h_i}{r_i}. \tag{7.4}$$

The domain of the Eq 7.2 is restricted as $[0, +\infty) \to [1, +\infty)$. After algebraic arrangements the function is inverted to the hyperbolic arc cosine by solving the quadratic Equation 7.5.

$$0 = e^{2w} - 2ue^{w} + 1 \tag{7.5}$$

The solutions are:

$$e^{w} = u \pm \sqrt{u^2 - 1} \tag{7.6}$$

Both are positive so by substitution of u and w in Eq. 7.6 the meniscus shape can be written as.

$$z(r) = h_i \pm r_i \cdot \ln\left(\frac{r}{r_i} + \sqrt{\left(\frac{r}{r_i}\right)^2 - 1}\right). \tag{7.7}$$

The Eq. 7.7 has two solution the positive (growing) and the negative (decaying) branch. The meniscus is described by the negative branch. In order to introduce a complete description of the surface profile we introduced the length L as an exponential decay factor, to describe the transition from the hyperbolic cosine behaviour (Eq. 7.7) to the planar far-field surface.

$$z(r) = \left[h_i - r_i \cdot \ln\left(\frac{r}{r_i} + \sqrt{\left(\frac{r}{r_i}\right)^2 - 1}\right)\right] e^{-\frac{r}{L}} + h_\infty. \tag{7.8}$$

Contact to the particle

The contact point on the bead is given by:

$$r^2 + (h_c - R)^2 = R^2. \tag{7.9}$$

Then

$$r(z) = \pm\sqrt{R^2 - (h_c - R)^2}. \tag{7.10}$$

It is known the angle of interception $(r_c; h_c)$ above two curves correspond to the angle form between the two tangents with the instantaneous slope at meting point; which is given by the corollary formula:

$$\Theta_c = \arctan\left(\frac{m_1 - m_2}{1 + m_1 \cdot m_2}\right); \tag{7.11}$$

Where the slopes m_1 and m_2 are given as:

$$m_1 = \pm\frac{R - h_c}{\sqrt{R^2 - (h_c - R)^2}}. \tag{7.12}$$

$$m_2 = \sinh\left[arcosh\left(\frac{\sqrt{R^2 - (h_c - R)^2}}{r_i}\right)\right]. \tag{7.13}$$

7.2.6 Universal meniscus profile and distortion length L

According to this equation the logarithmic contribution dominates for $r < L$ i.e., in the meniscus region up to where the meniscus phases out into the planar film. In this transient region away from the NP, close to $r = L$, the exponential contribution provides a smooth transition between the essentially logarithmic meniscus shape and the flat film. It should be noted that the profile of Equation 7.8 formally describes a meniscus shape with its left vertex contacting an (imaginary) vertical round cylinder of radius $r = r_0$ at a height $z = h_0$ with a contact angle of $\Theta_c^{cyl} = 0$. Mathematically this profile is identical to a meniscus, which intersects a NP with radius R at $r = r_c$ and at a height $z = h_c$ with a contact angle Θ_c^{NP} between the liquid and the NP surface.

Figures 7.6(a) and (b) demonstrate that the experimental data can nicely be fitted (red dashed curves) with the profile described by Equation 7.8. The linear-logarithmic plot Figure 7.6(b) shows a linear behaviour in virtually the entire meniscus range between the contact with the NP and the transition to the planar far field film surface. Practically, for fitting the experimental data, the exponential contribution of Equation 7.8 is rather negligible. It is only necessary to formally provide a smooth connection between the logarithmic meniscus profile and the planar far-field film surface. Figure 7.6 (b) also shows that fits of the experimental data with meniscus profiles according to Equation 7.8 yield rather well-defined distortion lengths L. Regarding interfacial physics, the logarithmic meniscus shape means that the liquid surface on the meniscus has nowhere a net local curvature. Hence there is no capillary pressure difference between the liquid in the meniscus section and the liquid within the surrounding planar film.

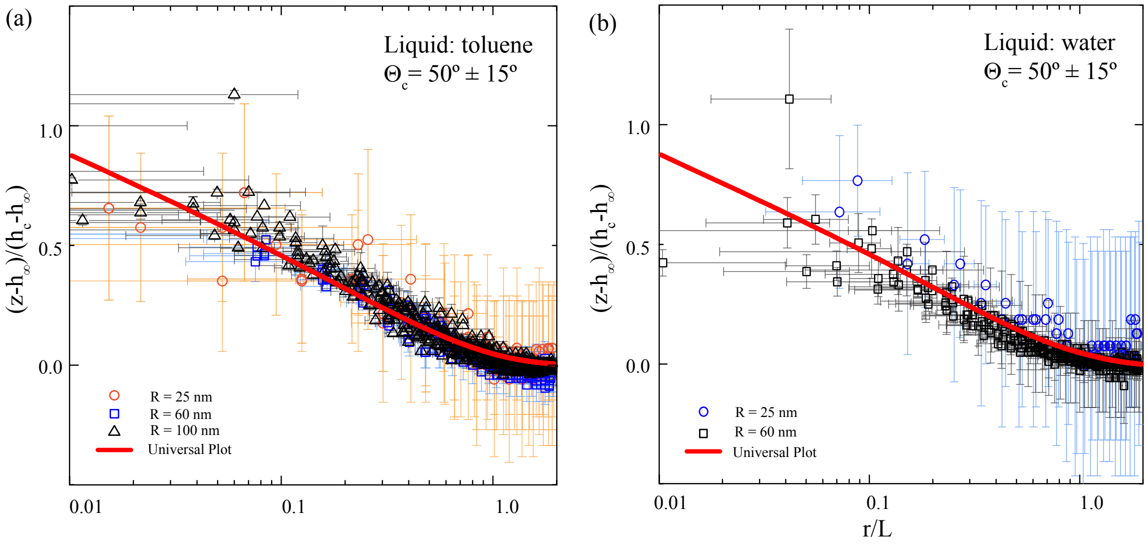

FIGURE 7.7: Meniscus geometries as measured for different NP radii, R, and film thicknesses, h_∞. The data are fitted according to the profile presented in Figure 2.2 and plotted in a universal way by rescaling the x-axis (lateral distance from the center of the NP, r) with the distortion length, L, and the y-axis (net vertical meniscus elevation, $z - h_\infty$) with the net distance between the film surface and the contact with the particle at $h_c - h_\infty$. Singled out by colour are those data points, where the interference conditions lead to a rather weak thickness contrast (orange data points in (a) and blue data points in (b)). Although technically this leads to rather large systematic error bars, the data still reflect the general behaviour quite well.

All the individually measured experimental meniscus profiles can be fitted quite well with the profile described by Equation 7.8, yielding different L, Θ_c, h_c, r_c, as well as h_0 and r_0 for the different known/measurable R and h_∞. Because all menisci can universally described by Equation 7.8 they also can be plotted in a universal way with proper axis scaling. This is demonstrated by Figure 7.7 presenting a large number of experimental data from different sized NPs embedded in films of different thicknesses. The films consisted of (a) toluene and (b) water. All the fits indicate for both liquids the same contact angle with the NPs of $\Theta_c \approx 50 \pm 10°$.

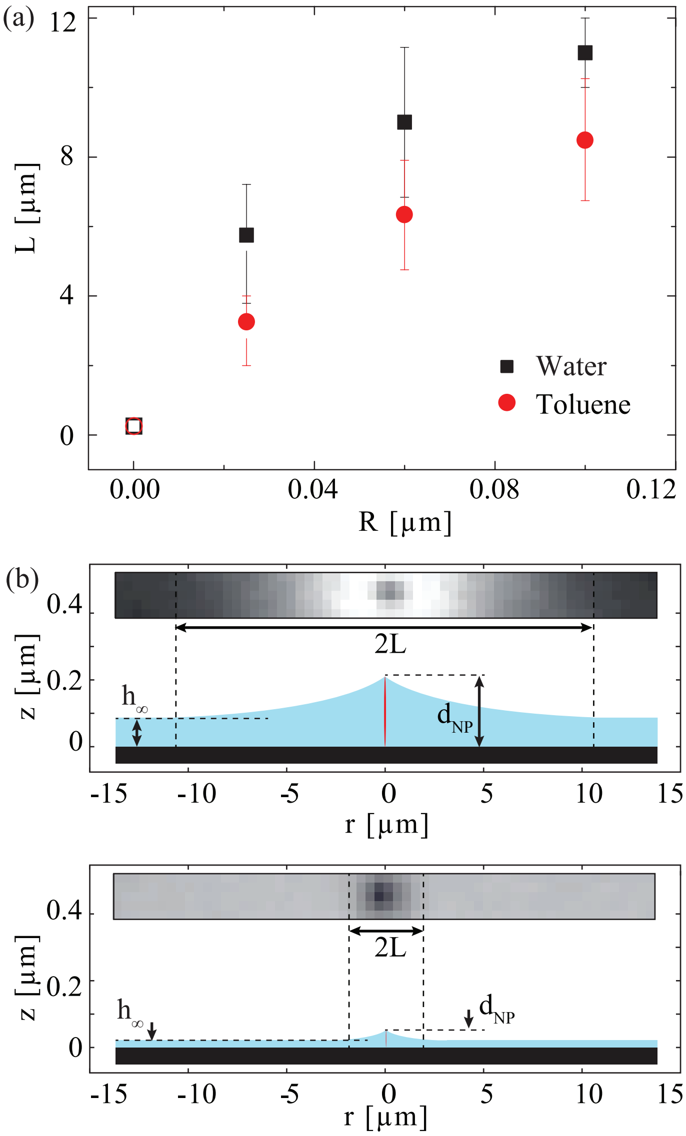

FIGURE 7.8: (a) Distortion length L vs NP radius R as derived from the fits of the experimental data. The open circles/squares at the origin indicate the data that are expected at this point.
(b) Optical imaging raw data and corresponding cartoons of the derived meniscus shapes for the combination of $d_{NP} = 200\,\text{nm}$, $h_\infty = 90\,\text{nm}$ (top) and $d_{NP} = 50\,\text{nm}$, $h_\infty = 12\,\text{nm}$ (bottom). The lateral and the vertical scales are different by nearly two orders of magnitude (the NPs appear as very elongated red ellipses).

Figure 7.8(a) shows a plot of the distortion lengths L vs the NP radii R. L is derived from fits of the experimental measured meniscus profiles. It can be seen that L increases with R in a slightly non-linear fashion (assuming that the origin is a data point). It is also observed that L of water is always slightly larger than L of toluene. Quite remarkable, L is independent from h_{∞}.

Figure 7.8(b) illustrates the findings presented in Figure 7.8 through a combination of raw imaging data from real experiments and schematics, which show the corresponding cross sections of the liquid film plus NP in the same lateral scale. Depicted are the cases of $d_{NP} = 200\,\mathrm{nm}$ and $h_{\infty} = 90 nm$ as well as the combination of $d_{NP} = 50\,\mathrm{nm}$ and $h_{\infty} = 12\,\mathrm{nm}$. The lateral scales of all microscope images and cartoons are the same. The vertical scales in both cartoons are the same but different to the corresponding lateral scales (hence the strongly distorted shape of the spherical NPs).

Chapter 8

Capillary-Enhanced Immobilization of Nanoparticles

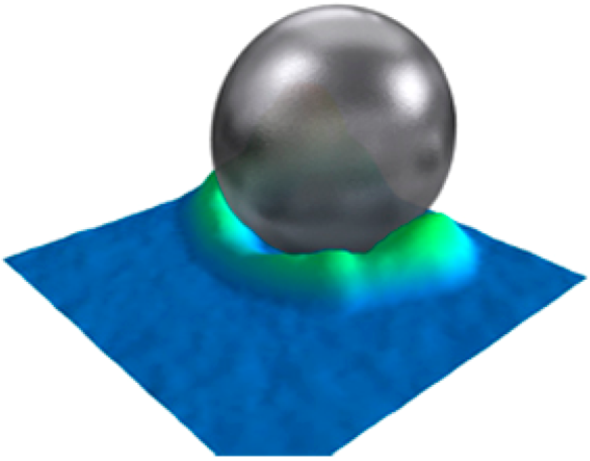

FIGURE 8.1: Capillary-Enhanced Immobilization

This chapter contents unpublished and published material from:

Guoxiang Chen, Rodrigo Perez-Garcia, José Danglad-Flores, and Hans Riegler. "Capillary-Enhanced Immobilization of Nanoparticles". In: *The Journal of Physical Chemistry Letters* 8.24 (2017), pp. 6094–6098.

J. Danglad-Flores performed AFM nano-particle manipulations experiments (APTES and polymer systems). He designed and performed the experiments with different particle size leading to the Figure 8.5 (unpublished data) His work was focused in the particle-polymer system. Chen developed the general idea, performed the APTES-particle experiments and wrote the first version of the manuscript. Pérez-García R. performed the experiments with the C_{60}-particle system and contributed to the image processing. H.Riegler organized and supervised the research, re-wrote the manuscript and contributed to the data analysis and interpretation. All authors have discussed the results, read the manuscript, and agreed with its content.

8.1 Introduction

Films of nanoparticles (NPs) on solid substrates have immense potential for novel applications as new composite and functional materials e.g., in catalysis [166], chemical sensing [167–169], electrochemistry [170], or other devices [171–174]. A key requirement in most applications of NP coated surfaces is a strong, persistent adhesion of the NPs to the surface.

The mechanical stability of NP coatings has been achieved by various ways, such as thermal embedding [175] atomic/molecular layer deposition [176, 177], and covalent chemical bonding [178–180]. Chemical bonding is often accomplished through coupling agents. Typically this means functionalization of the substrate surface by deposition of a (molecularly) thin layer of the coupling agent before the NP deposition. With chemical bonding through coupling agents the adhesion between NP and substrate is determined by the interactions between NP and coupling agent and coupling agent and substrate, respectively. It depends on the individual strength of the bonds and on the number of bonds. The contact area ("footprint") between a spherical NP and a planar substrate is rather small. Therefore the overall adhesion of the NPs to the substrate can be relatively weak, even with strong individual bonds. NP adhesion can be improved by increasing the number of contacts between NP, coupling agent and substrate, indeed a strong NP adhesion may be achieved even though the individual interactions/bonds between NP, coupling agent and substrate are rather weak.

A substantial increase of links between NP and substrate through a coupling agent can be achieved through capillary effects [165]. Enhanced adsorption in pores (kind of "capillary condensation") can be used to enrich the coupling agent in the annular gap, which surrounds the small direct footprint area between the NP and the substrate surface (the gap acts like a "pore"). Here this concept is pursued for various cases. It is applied to upgrade the widely used protocol for the immobilization of NPs with APTES as coupling agent. It is also shown that the approach also works well with ordinary polymers as unspecific coupling agents. It is demonstrated that with this approach even weakly interacting monomers such as fullerenes (C_{60}) can be used to immobilize NPs on planar surfaces. The adhesion strength is investigated by ultrasonication experiments and the proposed capillary-enhanced adhesion scheme is corroborated by AFM investigations.

8.2 Results

Figure 8.2 presents a comparison between the "conventional route" that has been used up to now to immobilize NPs with APTES ("APTES-NP") and our new route using APTES, a polymer and a monomer (C_{60}) as coupling agents (NP-APTES", Polymer, C_{60}). In all cases planar surfaces of silica (silicon wafers with an oxide layer) serve as substrates. The surfaces were cleaned and hydroxilated by piranha solution (for more details on the substrate cleaning/preparation see Chapter 3).

In the conventional route the hydroxylated silica surface is first coated with a thin (molecular) layer of APTES. For a smooth surface coating this is preferentially done by chemical vapour deposition (CVD)[181, 182]. Then NPs are deposited onto these coated surface by immersion of the substrate into an aqueous NP suspension[183]. As depicted in Figure 8.2 the immobilization of the NP on the substrate is dominated by the cross-link between the amine of the APTES and the citrate attached to the NP. Because APTES as well as citrate supposedly form a thin (monomolecular) film, links between substrate and NP are limited to the rather small area of direct contact between the planar substrate and the spherical NP.

In the new approach, the sequence of preparation steps is changed. The NPs are deposited on the silica substrates before the surface is exposed to the coupling agent. They are deposited from an aqueous solution by evaporative spin casting, which allows a precise control of the NP coverage [29, 33]. The NPs adhere (weakly) to the bare silica surface because of VdW interactions. The coupling agents are deposited on the substrate after the deposition of the NPs on the substrate. Three types of coupling agents were applied: 1.) a widely used cross-linking monomer (APTES), 2.) polymers, such as polystyrene (PS, Mw:45k), and

3.) a monomer (C_{60} fullerenes). APTES was applied by CVD from the gas phase, as in case of the conventional approach. The polymers as well as the C_{60} monomer were deposited by evaporative spin casting from solution with a volatile hydrophobic solvent (typically toluene). The spin cast conditions were adjusted to obtain only a very low overall surface (submonolayer) coverage of the polymers respectively C_{60} monomers [32].

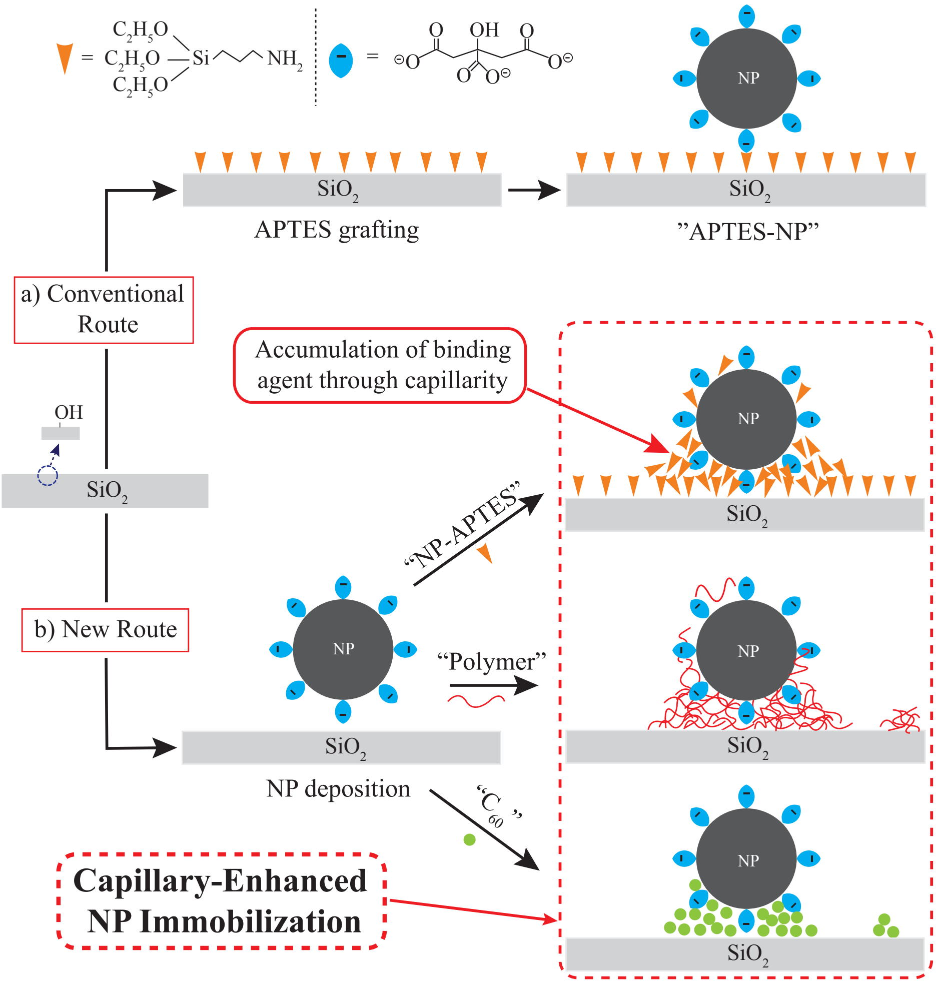

FIGURE 8.2: Comparison between (a) the widely used *conventional* route for NP immobilization on planar substrates by a molecularly thin film of APTES and (b) our *new* approach. In the conventional approach the surface is first functionalized by APTES and then the NPs are deposited (*APTES-NP*). In our new approach the sequence is reversed: First the NPs are deposited and then the *coupling* agents (APTES, polymer, C_{60} monomer).

8.2.1 Enhanced adhesion

Figure 8.3 presents a comparison of the NP adhesion strength between the conventional route and the new approach. To this end the samples were sonicated in a water bath for 30 minutes. The left column shows AFM data of dry samples prior to the sonication ("As deposited"). The right column shows dry samples after they were sonicated for 30 min in a water bath ("After sonication"). Data are presented (from top to bottom) for the following preparation procedures: 1.) without any coupling agent (No APTES), 2.) with APTES applied in the conventional route (APTES-NP), 3.) with APTES applied in the new route (NP-APTES), 4.) with an ordinary polymer ("PS") applied in the new approach and 5.) with a monomer also applied in the new route (C_{60}). It should be noted that Figure 8.3 presents for most of the case the same sample areas before and after the sonication treatment. This is made possible by a special AFM sample holder, which allows to reproducibly position and investigate (with the same AFM tip) the sample after it was taken out of the AFM sample holder for the sonication. In the case without any binding agent the surface is without NPs after sonication. With the conventional preparation sequence, a substantial amount of the NPs is missing. With the new method the NP coverage is virtually unchanged after the sonication for all coupling agents. The vast majority of NPs remain at their original locations. It is very hard to find NPs that are missing after the sonication (see inset in Figure 8.3). The data demonstrate that the NP immobilization with APTES as binding agent applied by the new protocol is much more efficient than with the conventionally applied routine. It is demonstrated that conventional polymers without any specific interactions with the immobilization partners (NP, substrate surface) can be used as efficient binding agents. Even C_{60} fullerenes, a monomer without specific interactions with the binding partners, immobilize the NPs more efficiently than APTES applied by the conventional protocol.

8.2.2 Capillary condensation underneath of nano-particle

Figure 8.4 shows the results of experiments with individual NPs that were moved sideways (with the AFM tip) to reveal the original contact area (footprint) between the NPs and the substrate surface. The location of the NPs prior to their lateral displacement has been determined by triangulation based on the locations of other NPs in their vicinity. One can see that in the case with the NP grafted in the conventional way ("APTES-NP") the footprint area of the NP is barely different from the surrounding surface. In the case of the new method ("NP-APTES") the footprint area can be identified as a spot, which is different from the surrounding surface. The area is about $0.3\,\mathrm{nm}$-$0.4\,\mathrm{nm}$ higher. In the cases of PS and C_{60} as binding agent the footprint area reveals substantial elevations i.e., some extra deposit. The topologies are similar to rings opened by the lateral movement of the NP.

On Figure 8.5 the AFM images show the results of consecutive deposition experiments with first NP deposition and then the deposition of the polysterene („$NP - PS$“ $x_0(PS) \approx 10 \times 10^{-6}\,\mathrm{w/w}$). The particle diameters were (A) $d_p = 50\,\mathrm{nm}$, (B) $d_p = 200\,\mathrm{nm}$, (C) $d_p = 550\,\mathrm{nm}$, and (D) $d_p = 1000\,\mathrm{nm}$. The particles were pushed away from their initial position (in frame (A) the particle is only slighty shifted sideways, in the other cases the particles are out of the field of view). The panels present the area around the original position of the silica particles and their footprints. The initial positions (footprints) of the particles can be identified quite clearly. At their original location one can see annular rings of polymer (white arrow in frame (A)) as depicted already for particles with $d_p = 50\,\mathrm{nm}$ in Figure 8.5. Aside from the annular polymer footprints, which had accumulated in the annular gap between the particle and the substrate surface one can also see that the polymer aggregates in vicinity of the original particle location are affected up to a certain distance. Polymer aggregates near the original particle location are different in size than further away or there is even a polymer depletion zone (frames (C) and (D)). The zone of influence is marked by the blue dashed ring extending up to $\sim 0.7\,\mathrm{\mu m}$ for the particle with $d_p = 200\,\mathrm{nm}$ (frame (B)), up to $\sim 3\,\mathrm{\mu m}$ for the particle with $d_p = 550\,\mathrm{nm}$ (frame (C)), and $\sim 6.5\,\mathrm{\mu m}$ for the particle with $d_p = 1000\,\mathrm{nm}$ (frame (D)). The depletion zone reaches out to $\sim 0.5\,\mathrm{\mu m}$ for the particle with $d_p = 550\,\mathrm{nm}$ (frame (C)), and $\sim 0.7\,\mathrm{\mu m}$ for the particle with $d_p = 1000\,\mathrm{nm}$ (frame (D)).

The data show that the amount of polymer, which is accumulated in the annular gap is increasing with particle size. Compared to the average polymer coverage this accumulated amount is quite substantial, in particular in the case of the larger particles. Therefore it is suggested that the depletion zone is a result of the accumulation/concentration of the

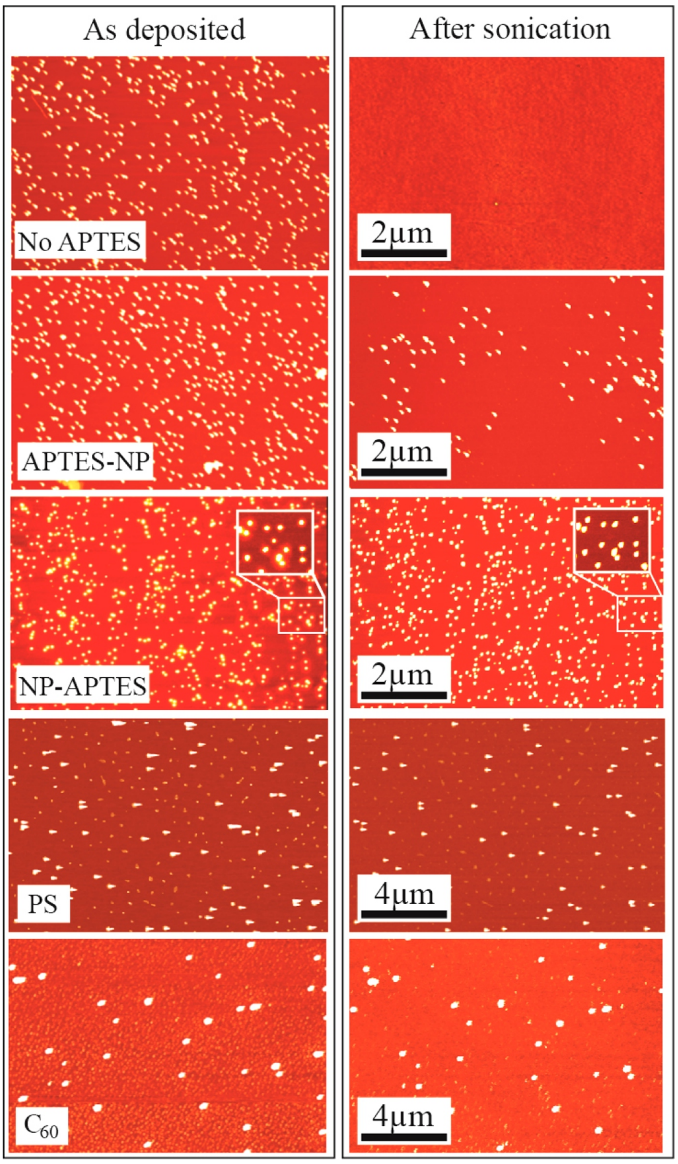

FIGURE 8.3: Comparison of the Pt NP substrate adhesion strength by sonication in a water bath. The AFM data shown the samples prior (left column) and after (right column) the sonication . From top to bottom for NP immobilization 1.) without any coupling agent, 2.) with APTES applied in the conventional route ("APTES-NP"), 3.) with APTES applied in our new route ("NP-APTES"), 4.) with an ordinary polymer ("PS") as agent applied in the new approach and 5.) a monomer (C_{60}), also applied in the new route. In the "NP-APTES" the soom up insert shows one NP is missing after the sonication. The NP sizes were $\sim 70\,\mathrm{nm}$ ("No APTES", "APTES-NP", "NP-APTES") and $\sim 25\,\mathrm{nm}$ ("PS" and C_{60}) in diameter.

polymer in the gap. Aside from that, the sizes of the polymer aggregates also vary with distance and size of the particles.

The size of the polymer aggregates is determined by nucleation and growth processes. The earlier the polymer overcomes the nucleation barrier, the earlier the aggregates start to grow and thus the bigger they can become (relative to those, which start to grow later). On the other hand, the size is also determined by the total supply i.e., how long the aggregates

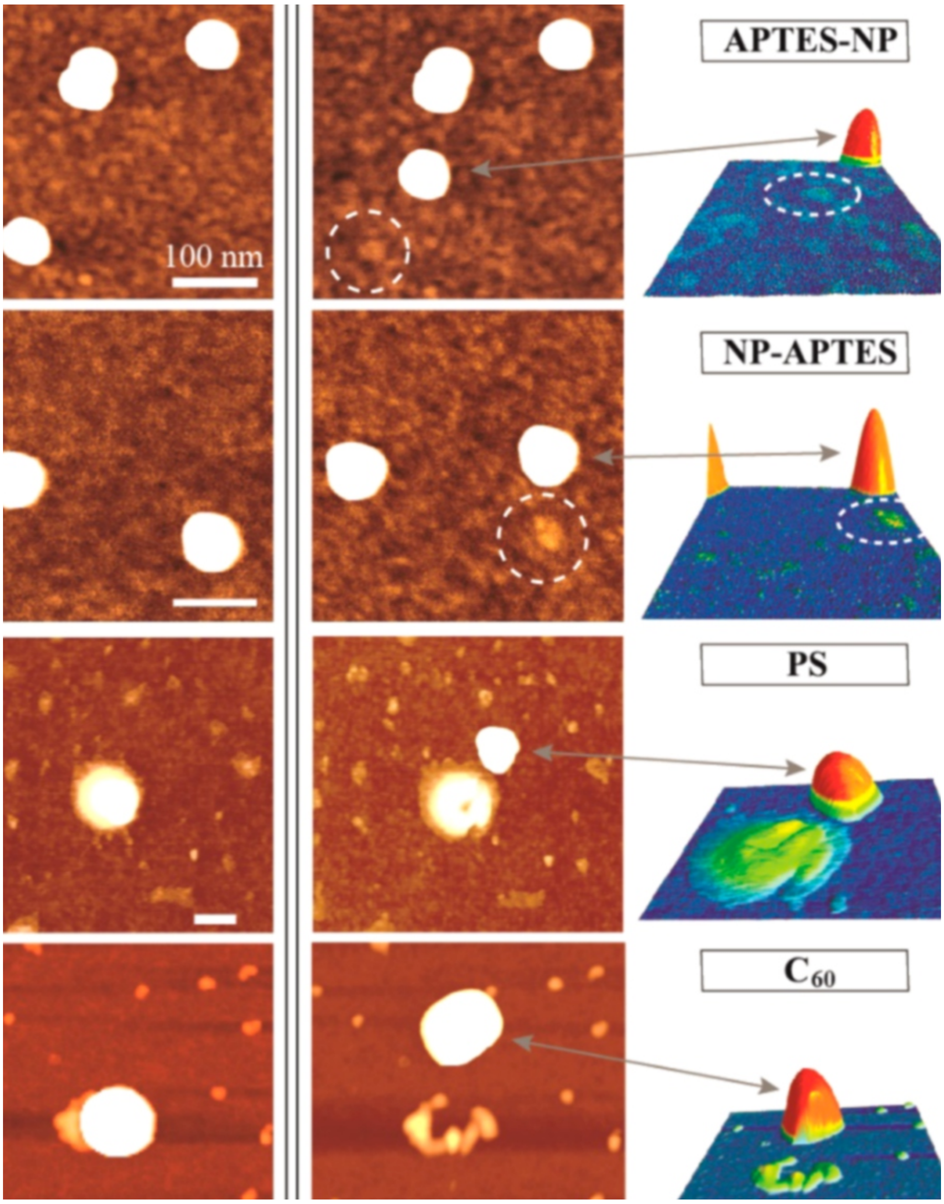

FIGURE 8.4: AFM images from consecutive deposition experiments $NPmolecule$, the footprint areas after moving individual NPs away from their original position. Left row AFM image prior to particle movement. Middle row AFM images of the same area after lateral movement of the NP. Right row AFM 3D images of the area in the vicinity of the NP (after it is moved).

can grow until the supply stops when the entire solvent has evaporated. It can be assumed that the polymer transport occurs by diffusion. On line optical microscopy shows that the polymer solution is not dewetting. Rather it forms a meniscus, as presented in Chapter 7. By and large, the observed polymer aggregation and aggregate size distribution is the result of a complicated interplay between film drying, local polymer enrichment, and nucleation and growth processes.

8.3 Discussion

It appears as if the extra deposit was located in the annular gap around the contact area between the NPs and the substrate. The AFM data also show that the surface areas of the

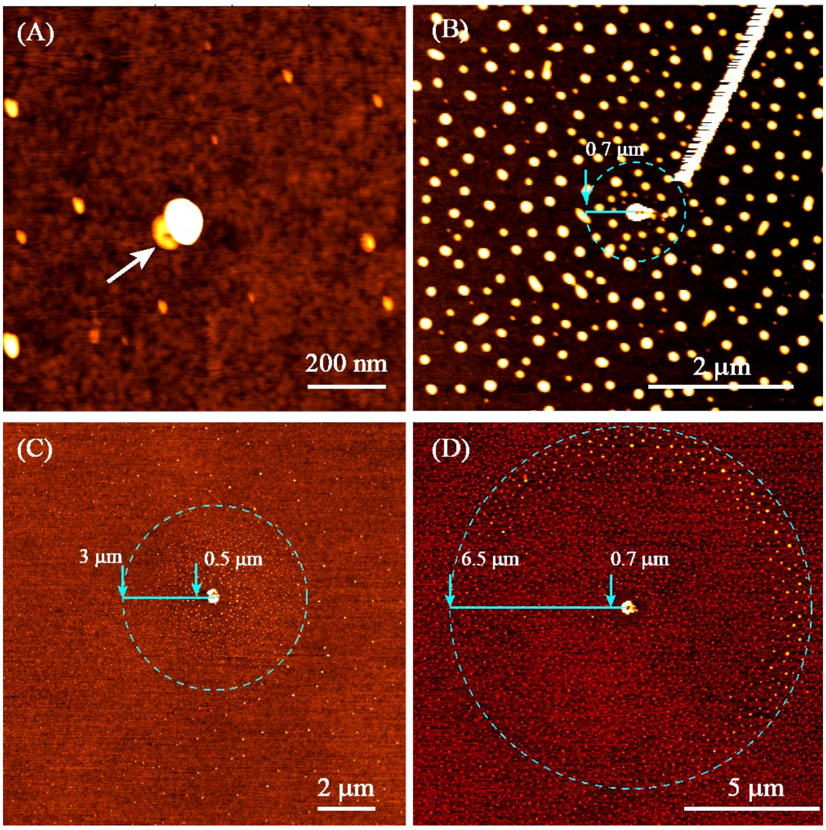

FIGURE 8.5: AFM images from consecutive deposition experiments $NP - PS$ (first nanoparticles, then polymer deposition). The NPs were removed after the preparation (in (A) it is still close to the original location) and the images show the area around their original location with (A) a particle with $d_p = 50\,\mathrm{nm}$, (B) a particle with $d_p = 200\,\mathrm{nm}$, (C) a particle of $d_p = 550\,\mathrm{nm}$, and (D) a particle of $d_p = 1000\,\mathrm{nm}$. The frames show the polymer accumulation within the annular gap next to the NP contact with the substrate. They also show how far the influence of the NPs reaches regarding the polymer aggregate size and distribution. On-line microscopy shows that the polymer aggregate nucleation and growth occurs during a film thinning behaviour as depicted in an earlier chapter of this thesis. There is meniscus formation but no dewetting during film thinning/drying.

samples without attached NPs, which were prepared with the APTES by the conventional as well as by the new method are relatively featureless with a roughness of a few Å. This indicates a (monomolecular) APTES coating without bulk aggregates of APTES (the sonication data of the first row in comparison to the second row of Figure 8.3 proves that there is some APTES on the substrate surface). With PS occasional patches/domains about 10 Å thick are observed. The shape and amount of these individual PS domains are typical for a submonolayer coverage of PS on silica as is expected from the applied spin cast conditions. It is remarkable that these domains are much thinner than the deposits found in the footprint area. For C_{60} individual C_{60} aggregates (spherical caps) are observed, which are distributed randomly over the substrate surface. This is in agreement with investigations on C_{60} deposited on silica [184, 185]. In comparison to the case with PS the C_{60} accumulated in the annular gap around the contact between NP and substrate appears more like a chain of spherical caps than a continuous broken ring. The experimental data with the PS and the C_{60} demonstrate that the enhanced NP immobilization is not caused by larger, polymeric-like structures formed by the binding agents, which create a layer on top of the

NPs and the substrate surface, holding the NPs in place. It appears very unlikely that PS forms a large closed network at the low PS coverage applied. For C_{60} under the applied conditions a network-like structure holding the NPs in place is even more unlikely. AFM data reveal that with the new preparation protocol the binding agent is accumulated in the annular gap surrounding the contact between the spherical NPs and the planar substrate surface. The accumulation could lead to the enhanced immobilization of the NPs, because it increases the number of links between substrate, binding agent, and NP. In other words, the contact area between NP and substrate is increased. We propose that the accumulation of the binding agent is caused by capillarity. The annular gap surrounding the small contact area between the spherical NP and the planar substrate acts like a narrow pore, where the binding agent gets enriched due to capillary-enhanced adsorption (kind of a "capillary condensation") [186–188]. It is shown that this "capillary-enhanced grafting" works for different methods of applying the binding agent, such as deposition from the vapor phase and deposition from solution. It works with different types of binding agents, such as those with specific tailor-made cross-linking properties (APTES). But it also works with polymers without specific binding properties (PMMA, PS). It even works with monomers without binding properties (C_{60}). It is also demonstrated that the new route works for NPs of different sizes and NPs made from other material than platinum (e.g., gold, see appendix Figure B.4). Figure 8.5 indicates the possible limitation of the presented new approach respect to the size of the particles. It shown that particles $d_p \geq 200\,\mathrm{nm}$ are removed by the AFM tip during the imaging (Figure 8.5 B). The scale of the concentrically regions around the particles (where the size and distribution of the polymer aggregates is affected) increases with the particle size. This fact seems to agree with the increases of the meniscus length L presented in Figure 7.8 for pure liquid systems (Chapter 7). Although, what it determines the exact length is still an open question.

The new preparation protocol is quite universal. It also works for different shapes of NPs and substrates as long as the attachment of the NP to the substrate surface creates some pore-like structure, which then leads to a capillary-enhanced local accumulation of the binding agent. In conclusion we present a new preparation protocol to immobilize NPs on surfaces through binding agents. In contrast to the conventional immobilization protocols we attach the NPs to the bare substrate first and deposit the binding agent afterwards. sonication experiments prove that this can strongly increase the adhesion of the NPs.

8.4 Summary and Conclusion

The consecutive deposition of nanoparticles and molecules was studied. Molecules with specific and unspecific binding properties were tested. The sequence of deposition of particle and later molecules enhances the attachment of nanoparticles to the substrate. Even in the case of molecules with unspecific binding propierties. In comparison with the conventional sequence used for nanoparticle fixation (molecules-particles); the sequence presented here leads a higher nanoparticle immobilization. Therefor is proposes a new route for nanoparticle fixation.

Chapter 9

Summary and Conclusions

The formation of thin liquid films by hydrodynamic-evaporative spin casting is studied on-line, and it is investigated how the evaporation process in this configuration leads to a final deposit. The liquid films consist of volatile components and nonvolatile species, which are finally deposited. The experimentally obtained results were analyzed and based on the data the processes were described theoretically. In particular a new time-resolved, optical interference microscopic approach gave new insights into the film thinning behavior. The sophisticated, new investigation technique was supported by AFM and ellipsometry.

The spin cast process is driven by an interplay of hydrodynamics (viscous flow) and evaporation. Therefore, in a most simple approach, the evaporation rate of pure volatile liquids films on a rotating plate was investigated as function of the speed of rotation, ω, including the static case $\omega = 0$. The static evaporation rate e_0 was found significantly smaller compared to evaporation rates with $\omega > 0$. It is observed that the evaporation rate in a spin cast setup can be described by $E(\omega) = e_0 + e_\omega\sqrt{\omega}$. Except for the static contribution, this agrees with theoretical predictions. For polymer solutions, the evaporation rate was found approximately the same as for the pure solvent up to moderately high polymer concentrations ($x \sim 0.5\,\mathrm{w/w}$).

The case of spin casting of mixtures of nonvolatile solutes dissolved in volatile solvents was directly observed with time resolved microscopy. The results were compared with predictions of the *zero order model*. The *zero order model* assumes for the spin cast process viscous and evaporative properties of the volatile solvent only. It ignores solute contributions and it is valid for low solute concentrations. Measurements show that beyond certain solute concentrations the predictions of the *zero order model* become inaccurate. It turns out this is mainly due to the change in viscosity. Based on these findings a modification of the *zero order* model has been developed. The *first order* correction takes into account the viscosity changes due to the solute. It predicts the polymer concentration evolution within the film and the final polymer film coating quantiatively correct for polymer concentrations of up to $x \sim 0.15\,\mathrm{w/w}$.

Complementary to the deposition molecules (polymers) also the deposition of nano and micron size spherical particles dispersed in volatile liquids is investigated. Studies were performed as function of the particle weighing in concentration, the particles size, and the densities of liquid and particles. Again the data were first analyzed in view of the *zero order* approach. It is shown that this theory is valid for small particles and for low particle concentrations. However for particles with more than several microns in diameter, the observed final coverage exceeds the predictions. The observed *zero order* prediction boundaries are studied and analyzed in terms of the particles size and the particle sedimentation. Modifications of the *zero-order* approach were worked out, which result in an improved theory that correctly predicts the particle final coverage.

With the new microscopy setup the shape of the liquid film surface was investigated, when the thickness of the liquid film approaches the size of embedded nanoparticles. Thus for the first time the lateral distortion of a liquid around a nanoparticle has been measured experimentally. It is found that the meniscus has the shape of a hyperbolic cosine curve. Its size, the lateral distortion extension (length) is unexpectedly large. However shorter than the capillary length given for the liquid. It scales with the nanoparticle size. What determines length of the distortion remains unclear. Because of the unexpectedly large distortion length, orders of magnitude larger than the nano particle size, the nano particles can be located/observed optically although their size is much smaller than the diffraction limit.

Also investigated was the consecutive deposition of nanoparticles and molecules by spin casting. It was tested, how specific and unspecific binding properties of the molecules to the nanoparticles and the substrate surface influence the attachment of the nanoparticles to the substrate surface. Unexpectedly, it is found that the attachment of nanoparticles to the substrate is strongly increased if a solution with a low concentration of molecules (small molecules, polymers) is deposited by spin casting *after* the nanoparticles are already deposited on the substrate surface. It is found that in this case the molecules accumulate because of capillary effects in the annular gap next to the contact between the particles and the substrate surface. The particle immobilization rather strong is due to the rather large of contact area between substrate, accumulated molecules, and particle, even for molecules with unspecific binding properties.

In sum, this work deals with several aspects of spin casting, although the focus is on a better understanding of the processes occurring during film thinning and how these processes determine the final deposit. Based on experimental data and their analysis theoretical approaches are developed, which describe the processes significantly better than previous approaches. The focus is in particular on predictions regarding the final solute coverages. The results help to improve the application of spin casting as a tool to fabricate well defined films of monomers, polymers, or nanoparticles.

Chapter 10

Outlook and On Going Work

10.1 What is the minimum volume needed to create a film?

It should be noted that in both cases, the zeroth-order analysis and the first-order approach discussed in Chapter 4 and 5 is assumed ideally an "$infinite\ liquid\ column$" at time zero. The liquid thins by hydrodynamics with a constant overall concentration before the h_{tr} is reached. Thus, the deposited amount of liquid has to be sufficiently large. But, how much is sufficiently large?

In practical terms a limited volume is dropped on the substrate and during the transcendence period it is extended to form a homogeneous film over the surface. There is a practical reason to estimate the initial homogeneous film height h_0. The initial film h_0 is the minimum liquid film height needed to create a film, that will thin homogeneously, before the h_{tr} is reached. Then h_0 can be translated in the minimum effective volume of solution to be dispensed. Coming back to the work of Emslie et al.[30]. We take the most simple scenario of a drop with an Gaussian initial contour which distribution isgiven by.

$$h_0 = a \cdot e^{-\alpha^2 \cdot r_0^2}. \tag{10.1}$$

Where a is the initial thickness at the center, α is the reciprocal of the radius (r). Considering the solutions of the differential equations for the system **??**, it has been shown that the condition [30]

$$Ka^2 t_p = 1, \tag{10.2}$$

produces and uniform thickness film. In the most extreme case the film must be planar at the time (t_p) when reach the h_{tr}, so we take the t_{tr} as a limit, expressed as.

$$t_{tr} = \left(\left(2\pi - \sqrt{3}\log 4\right)/(4\pi)\right) \cdot t_{sc} \approx 0.309 \cdot t_{sc}. \tag{10.3}$$

By substituting Eq. 2.19 and 10.3 in Eq 10.2 and after mathematical arrangements a is

$$a = \sqrt{\frac{2 \cdot 3^{3/2}}{2\pi - \sqrt{3}\log 4}} \cdot h_{tr} \approx 2 \cdot h_{tr}. \tag{10.4}$$

Now, on a free infinite impermeable surface a drop of initial volume V_0 at the center will spread radially in a "$pancake\ like\ shape$"[44]. Eq. 10.4 ideally predict the film height after the transition from a drop shape to a planar pancake; but indeed the film will keep thinning hydrodynamicaly from "a" until reaches the h_{tr}; therefore neglecting the lost of solvent due to evaporation, thus the maximum area covered by the liquid film will be equivalent to the final coated area (A_Γ) after the evaporation leading to the solute deposition. A_Γ should be limited by the initial dropped volume in order to satisfy:

$$A_\Gamma = \frac{V_0}{2h_{tr}}. \tag{10.5}$$

The expression given on Eq. 10.5 seems very simple but; if it is confirmed implies a practical optimization tool for coating purposes.

10.2 Thin Films with Lateral Surface Tension Gradients

The film thinning of liquid binary mixtures was preliminary investigated. Both liquids were volatile and completely miscible. Individually the liquids wet the substrate (silica). The thinning of the pure liquids by spin casting was continuously planar films until complete evaporation. Mainly two parameters were evaluated; the difference in the evaporation rates E and difference surface tensions γ. Liquid A is the one with the higher evaporation rate E_f ("f" for faster). Liquid B has the lower evaporation rate E_s ("s" for slower). The corresponding surface tensions are γ^A and γ^B. This defines a surface tension difference:

$$\Delta\gamma^{\mathrm{A,\,B}} = \gamma^A - \gamma^B \tag{10.6}$$

For instance, toluene has a surface tension of $\gamma_{tol} = 28.5\ \mathrm{mN/m}$ and nonane of $\gamma_{non} = 22.8\ \mathrm{mN/m}$. Thus $\Delta\gamma^{\mathrm{tol,\,non}} = +5.7\ \mathrm{mN/m}$. The combination of heptane ($\gamma_{hep} = 20.1\ \mathrm{mN/m}$) and nonane yields $\Delta\gamma^{\mathrm{hep,\,non}} = -2.7\ \mathrm{mN/m}$. Toluene has an evaporation rate of $E_{tol} = 1800\ \mathrm{nm/s}$, heptane $E_{hep} = 3000\ \mathrm{nm/s}$ and nonane $E_{non} = 600\ \mathrm{nm/s}$ (all at $\omega = 1000\ \mathrm{rpm}$). All these liquids are miscible without a miscibility gap and combinations with various ratios of E as well as positive and negative $\Delta\gamma^{\mathrm{A,\,B}}$ can be investigated. The mixing ratios x_0 are the initial ratios (weighing in) prior to liquid deposition and film formation.

Figure 10.1(a) shows a sequence of microscopy images recorded during the film thinning of a mixture of 10% nonane and 90% toluene. Under each frame cartoons are presented the suggested film topography. In the beginning at t=$0.604\ \mathrm{s}$ the liquid mixture is virtually planar (the gray level variations indicate a vertical roughness variation of only $\approx 100\ \mathrm{nm}$ on a lateral distance of mm). At $1.257\ \mathrm{s}$ the films starts to become wavy. This feature becomes more pronounced ($1.648\ \mathrm{s}$) and eventually pronounced undulations are formed ($1.950\ \mathrm{s}$). At this stage the vertical roughness is in the range of micrometers, comparable to the (average) film thickness. The holes of the undulations finally come into contact with the substrate. The film ruptures and splits into individual drops ($2.003\ \mathrm{s}$). These drops continuously become smaller through evaporation and after some time the substrate is completely dry.

Figure 10.1(b) shows the evaporative film thinning behaviour of a mixture of 10% toluene and 90% heptane. In contrast to the nonane/toluene mixture the film remains rather flat during its evaporation/thinning (it is not perfectly flat as in particular the image taken at time $2.000\ \mathrm{s}$ reveals. But it is flat in comparison to the case (a)).

Figure 10.2 presents a possible mechanism for the destabilization of evaporative thinning films of binary mixtures of volatile components with different evaporation rates and surface tensions. It can be assumed that occasionally small local inhomogeneities in the local evaporation behaviour may occur. These will result in a small local enrichment of one component. If the result of this local enrichment is a surface tension gradient, it may cause a Marangoni flow. If this flow acts against the local enrichment both, the enrichment and thus the flow will dissappear. The film remains stable. If the surface tension gradient leads to a Marangoni flow, which increases the local enrichment, this enrichment may get enhanced. In this case the film surface becomes wavy, undulated and eventually may even rupture. This mechanism explains at least qualitatively the main experimental findings. A more detailed analysis is currently in progress.

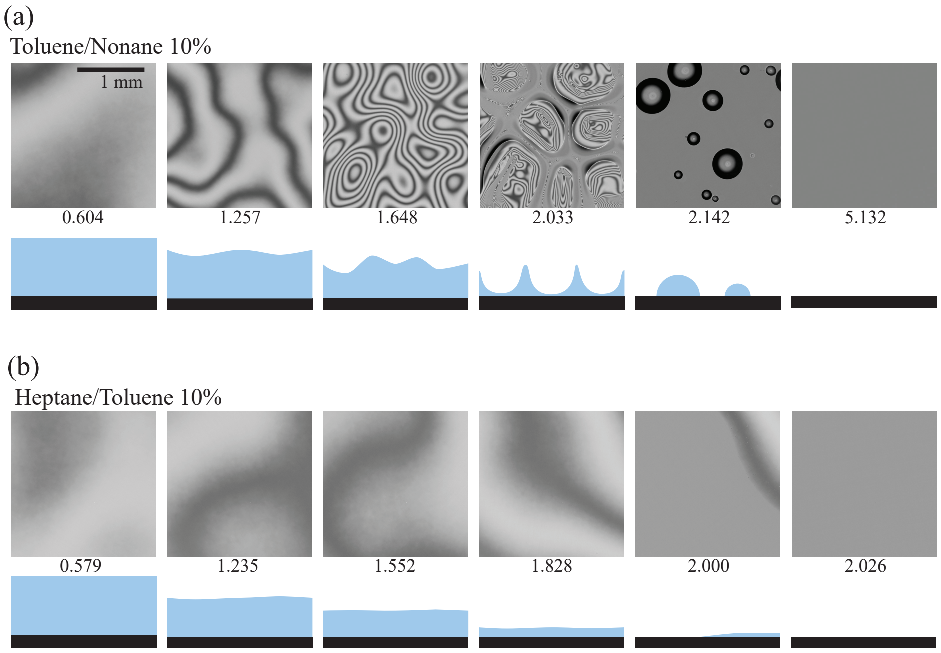

FIGURE 10.1: (a) Time sequence of optical microscopy imaging of a binary mixture of 10% nonane and 90%toluene ($\Delta\gamma^{\text{Tol, Non}} = +5.7\text{mN/m}$). Below each frame, a proposed cross section of the film topography is shown. (b) dito with 10% toluene in 90% heptane ($\Delta\gamma^{\text{Non, Hepp}} = -8.4\text{mN/m}$).

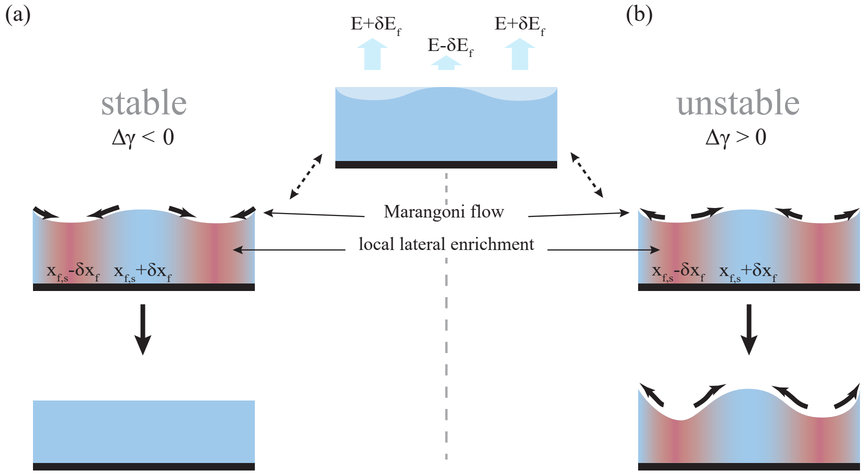

FIGURE 10.2: Proposed mechanism for the stabilization/destabilization of evaporative thinning films.

Films of binary mixtures of volatile liquids with a $\Delta\gamma < 0$ remain flat and stable during evaporative thinning. With $\Delta\gamma > 0$, the thinning films may or may not remain flat/stable. This depends on the composition x_0. In general, the undulation wavelength λ decreases with time (with decreasing film thickness). It is open the definition of λ in term of the system parameters.

Appendix A

Chemical and Physical Properties

A.1 Liquid Physicochemical Properties

TABLE A.1: Physicochemical properties of typical solvents in liquid state at normal conditions. In general the data was taken from Ref. [189]. With the following exceptions: ∗ Ref. [190], ∗∗ Ref. [191], † Ref. [95], † Ref. [192], ! Ref. [193], § Ref. [194], $ Ref. [195].

Solvent	ρ_L $[kg/m^3]$	M_a $[g/mol]$	P^* $[kPa]$	D_{ab} $[m^2/s10^{-6}]$	ν $[m^2/s10^{-7}]$
Water	1000	18	3.37	25.1 **	8.93
Toluene	867	92	3.79	8.03 †	6.34
Ethyl acetate	902	88	12.6	8.61 †	4.72
Chloroform	1483	119	26.2	8.88 †	3.65
Tetrahydrofuran	889	72	21.6	11.1 §	5.17
Dimethylformamide	944	73	0.502	9.73 †	8.5
n-Heptane	684	100	6.11	7.05 !	5.5
n-Octane	703	114	1.86	6.16 †	7.25
n-Nonane	718	128	0.572	6.43 !	8.65
n-Decane	730	174	0.22	5.74 !	11.8
Methylcyclohexane	770	98	6.05*	6.15 $	8.7
Ethanol	789	46	7.86	0.11 †	13.9
I-propanol	786	60	5.79	0.084 †	25.6

Appendix B

Final deposit

Deposited particles

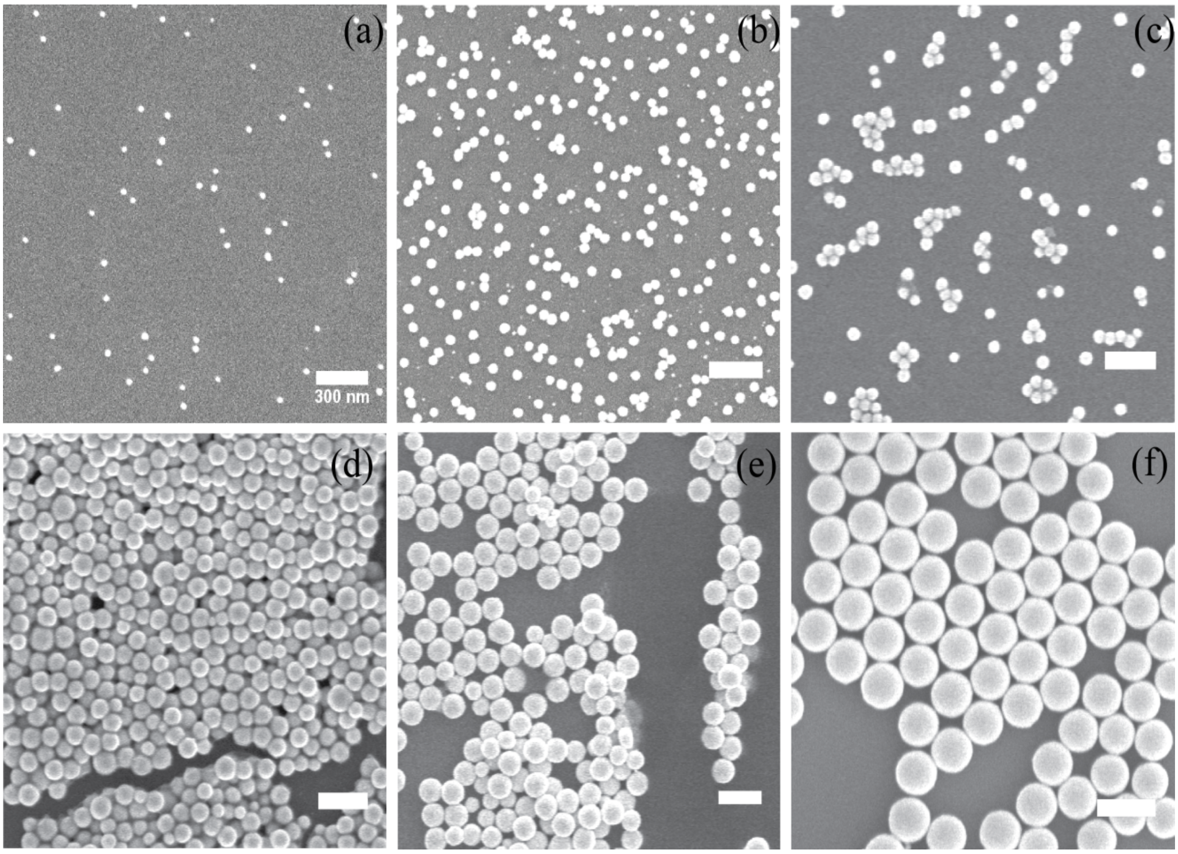

FIGURE B.1: SEM images of different diameters of Pt nanospheres: (a) 23 nm (seeds); (b) 50 nm; (c) 70 nm; (d) 100 nm; (e) 140 nm; (f) 200 nm. Scale bar: 300 nm.

Figure B.1 presents the SEM images of the synthesized Pt NPs with mean diameters of 23, 50, 70, 100, 140, and 200 nm. The particles appear spherical in shape, homogeneous in size and with smooth surfaces.

Fig.-S B.2 compares the final coverage at the substrate centre and near the edge of the substrate. Fig.-S B.2 (A-B) presents polystyrene particles (PS) $1000\,\mathrm{nm}$ deposited from aqueous dispersions of $x_0 \sim 1 \times 10^{-4}\,\mathrm{w/w}$. Fig.-S B.2 (C-D) shows polystyrene particles (PS) $1000\,\mathrm{nm}$ deposited from aqueous dispersions of $x_0 \sim 1 \times 10^{-2}\,\mathrm{w/w}$. The images of the left column where taken at the centre of the sample, the images of the right column where

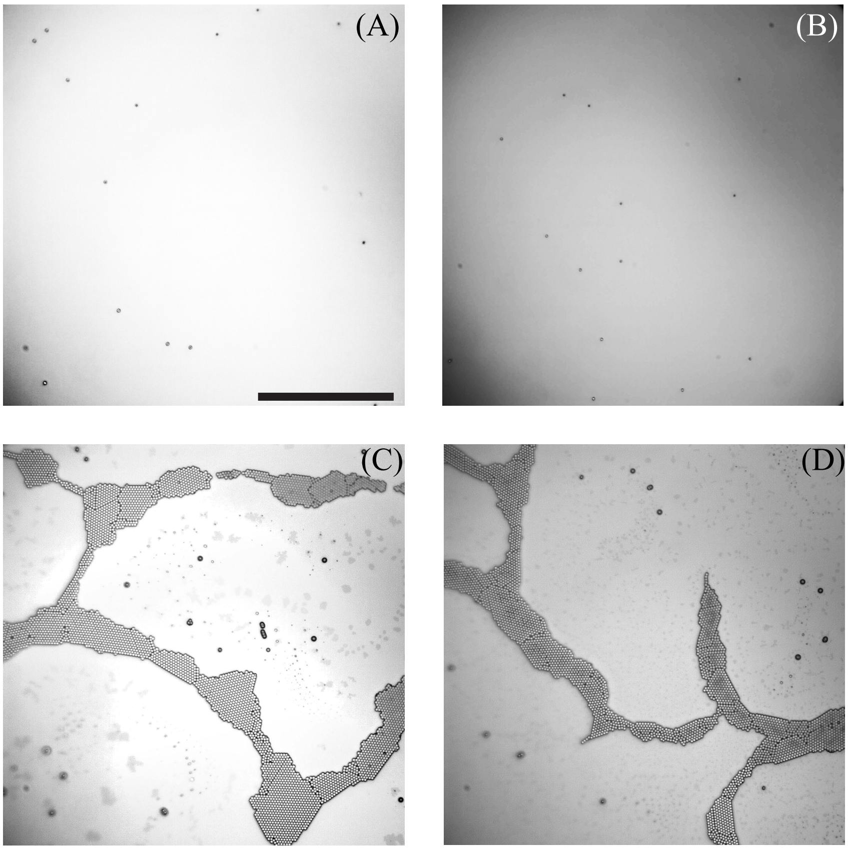

FIGURE B.2: Polystyrene particles (PS) $1000\,\mathrm{nm}$ deposited from aqueous dispersions of $x_0 \sim 1 \times 10^{-4}\,\mathrm{w/w}$ (A-B), and $x_0 \sim 1 \times 10^{-2}\,\mathrm{w/w}$ (C-D). The images in the left column where taken at the center of the sample. The images in the right column where taken within a radius of $8\,\mathrm{mm}$ from the center. In both cases $\omega = 1000\,\mathrm{rpm}$.

taken within a distance of $8\,\mathrm{mm}$ from the center. In both cases the rotational speed was $\omega = 1000\,\mathrm{rpm}$.

Fig.-S B.3 depicts calcium carbonate particles $CaCO_3$ as deposited from ethanol ($x_0 \sim 0.001\,\mathrm{w/w}$) with a mean $d_p = 2.6\,\mathrm{\mu m}$. Several areas were analyzed to obtain the particle size distribution from a sample of 100 particle observed.

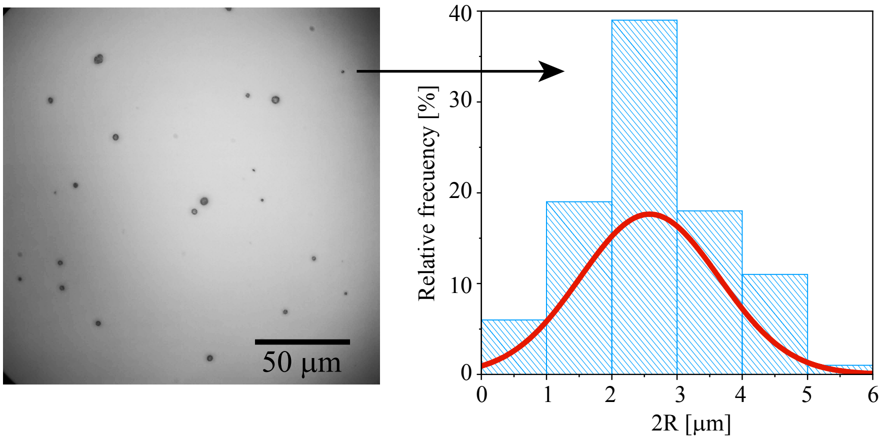

FIGURE B.3: (Left) Calcium carbonate particles $CaCO_3$ deposited from ethanol ($x_0 \sim 0.001\,\mathrm{w/w}$, $\omega = 1000\,\mathrm{rpm}$). The mean $d_p = 2.6\,\mu\mathrm{m}$. (Right) Details of the particle size distribution.

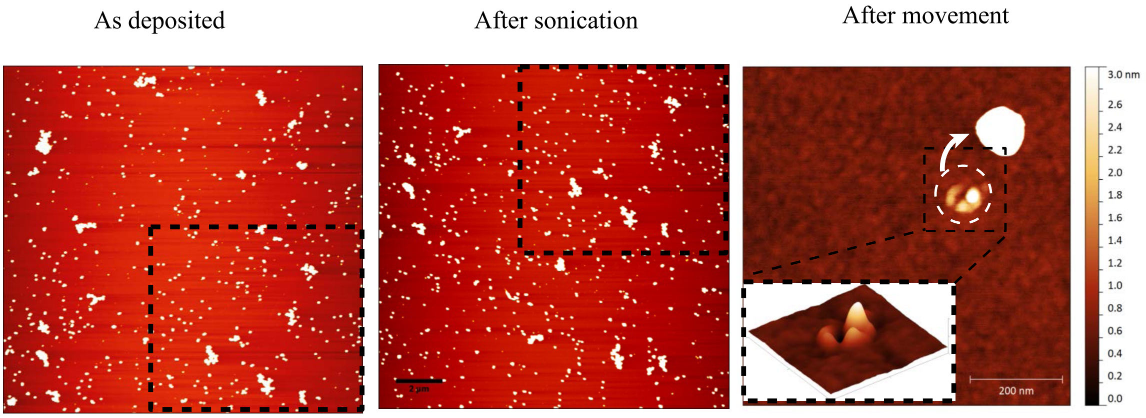

FIGURE B.4: Comparison of silica surfaces coated with Au nanoparticles following the deposition sequence $NP - APTES$ (left), after (middle) $30\,\mathrm{min}$ of sonication. The footprint area after moving individual nanoparticle (right). The black boxes mark the same substrate surface area.

Appendix C

Analytics and Calculations

C.1 Reflective Value according to Fresnel Equations

Following code was used to calculate the reflective response of toluene and water, using the Mathematica version of the program code by Steve Byrnes[83]:

$$\begin{aligned} dList1[dinnm\_] &= \{\infty, dinnm \text{ nm}, 48 \text{ nm}, \infty\};\\ nList1 &= \{1.0003, 1.3334, 1.4656, 4.7302\};\\ dList2[dinnm\_] &= \{\infty, dinnm \text{ nm}, 48 \text{ nm}, \infty\};\\ nList2 &= \{1.0003, 1.5057, 1.4656, 4.7302\}; \end{aligned}$$

The reflectivity as function of the thickness d for toluene and water:

$$R_{toluene}(d) = 1 + \frac{3.56438 + 1.11022 \cdot 10^{-16} \cdot \cos[0.0425195 \cdot d]}{-5.23357 + 0.477467 \cdot \cos[0.0425195 \cdot d] + \sin[0.0425195 \cdot d]}$$

$$R_{water}(d) = 1 + \frac{16.1709}{-22.5775 + \cos[0.0376539 \cdot d] + 3.14435 \cdot \sin[0.0376539 \cdot d]}$$

Appendix D

Reprinting license

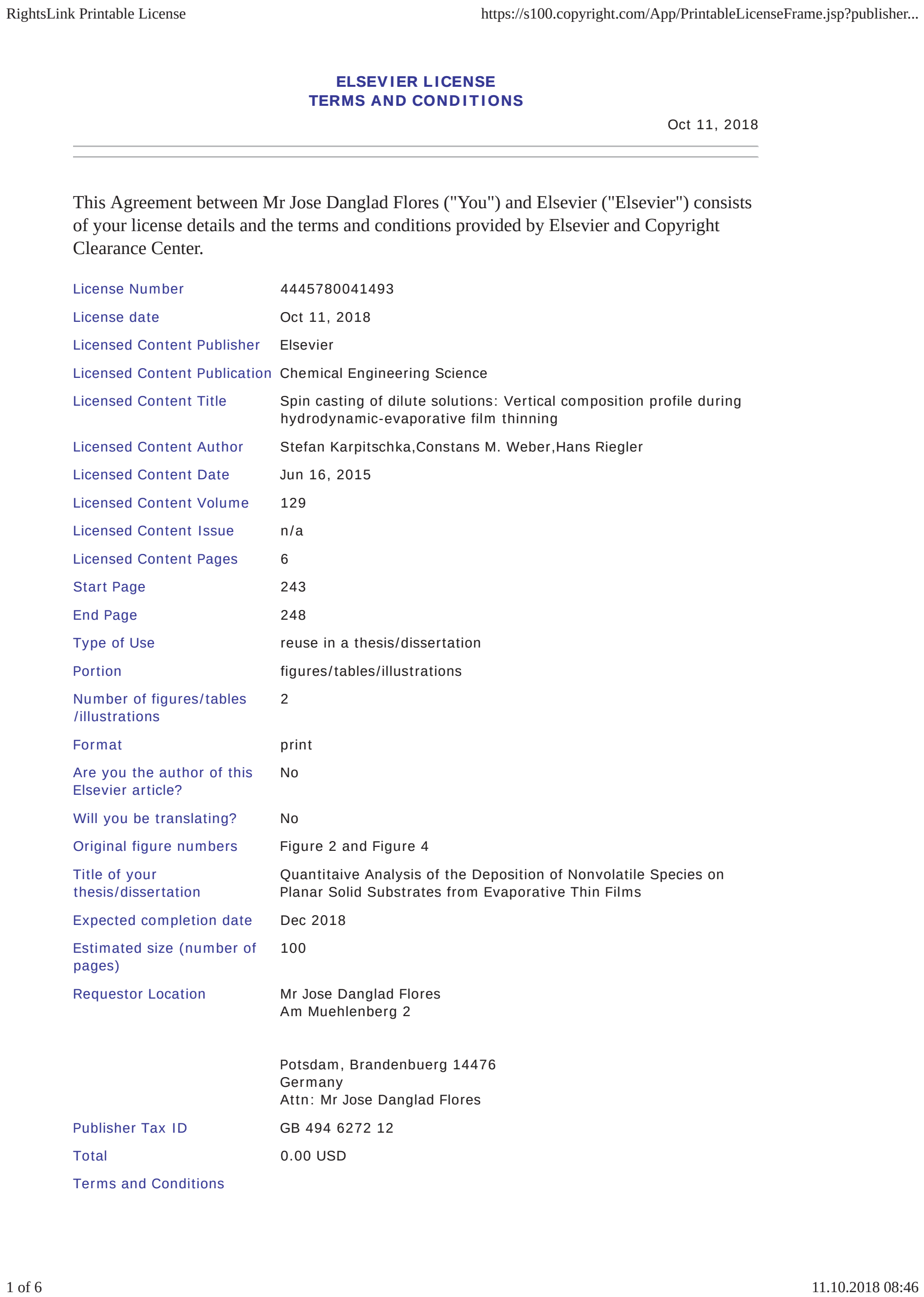

RightsLink Printable License https://s100.copyright.com/App/PrintableLicenseFrame.jsp?publisher...

ELSEVIER LICENSE
TERMS AND CONDITIONS

Oct 11, 2018

This Agreement between Mr Jose Danglad Flores ("You") and Elsevier ("Elsevier") consists of your license details and the terms and conditions provided by Elsevier and Copyright Clearance Center.

License Number	4445780041493
License date	Oct 11, 2018
Licensed Content Publisher	Elsevier
Licensed Content Publication	Chemical Engineering Science
Licensed Content Title	Spin casting of dilute solutions: Vertical composition profile during hydrodynamic-evaporative film thinning
Licensed Content Author	Stefan Karpitschka,Constans M. Weber,Hans Riegler
Licensed Content Date	Jun 16, 2015
Licensed Content Volume	129
Licensed Content Issue	n/a
Licensed Content Pages	6
Start Page	243
End Page	248
Type of Use	reuse in a thesis/dissertation
Portion	figures/tables/illustrations
Number of figures/tables /illustrations	2
Format	print
Are you the author of this Elsevier article?	No
Will you be translating?	No
Original figure numbers	Figure 2 and Figure 4
Title of your thesis/dissertation	Quantitaive Analysis of the Deposition of Nonvolatile Species on Planar Solid Substrates from Evaporative Thin Films
Expected completion date	Dec 2018
Estimated size (number of pages)	100
Requestor Location	Mr Jose Danglad Flores Am Muehlenberg 2 Potsdam, Brandenbuerg 14476 Germany Attn: Mr Jose Danglad Flores
Publisher Tax ID	GB 494 6272 12
Total	0.00 USD
Terms and Conditions	

1 of 6 11.10.2018 08:46

FIGURE D.1: Reprinting license Karpitschka et al. 2015.

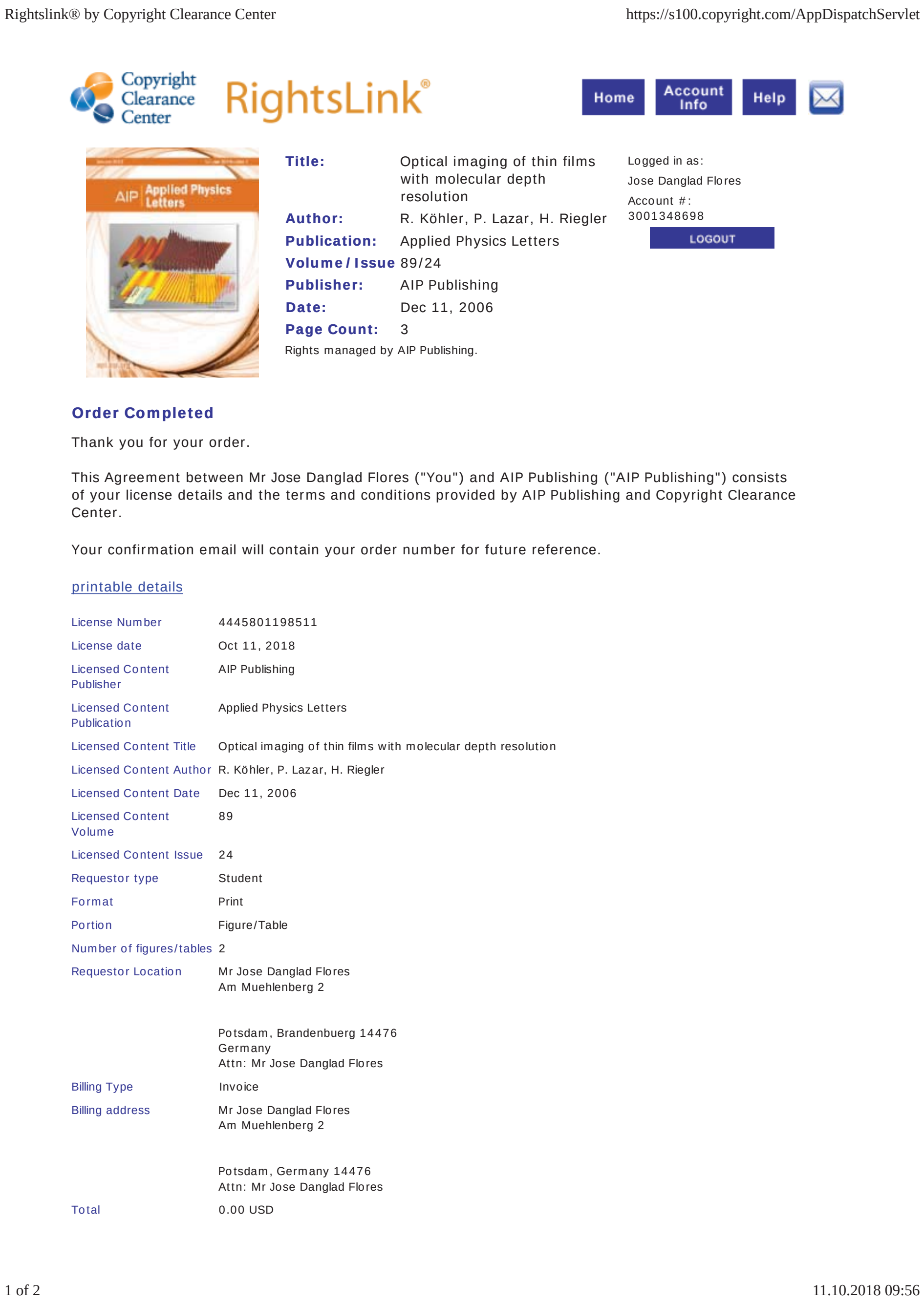

Rightslink® by Copyright Clearance Center https://s100.copyright.com/AppDispatchServlet

Title: Optical imaging of thin films with molecular depth resolution
Author: R. Köhler, P. Lazar, H. Riegler
Publication: Applied Physics Letters
Volume / Issue 89/24
Publisher: AIP Publishing
Date: Dec 11, 2006
Page Count: 3
Rights managed by AIP Publishing.

Logged in as:
Jose Danglad Flores
Account #:
3001348698

Order Completed

Thank you for your order.

This Agreement between Mr Jose Danglad Flores ("You") and AIP Publishing ("AIP Publishing") consists of your license details and the terms and conditions provided by AIP Publishing and Copyright Clearance Center.

Your confirmation email will contain your order number for future reference.

printable details

License Number	4445801198511
License date	Oct 11, 2018
Licensed Content Publisher	AIP Publishing
Licensed Content Publication	Applied Physics Letters
Licensed Content Title	Optical imaging of thin films with molecular depth resolution
Licensed Content Author	R. Köhler, P. Lazar, H. Riegler
Licensed Content Date	Dec 11, 2006
Licensed Content Volume	89
Licensed Content Issue	24
Requestor type	Student
Format	Print
Portion	Figure/Table
Number of figures/tables	2
Requestor Location	Mr Jose Danglad Flores Am Muehlenberg 2 Potsdam, Brandenbuerg 14476 Germany Attn: Mr Jose Danglad Flores
Billing Type	Invoice
Billing address	Mr Jose Danglad Flores Am Muehlenberg 2 Potsdam, Germany 14476 Attn: Mr Jose Danglad Flores
Total	0.00 USD

1 of 2 11.10.2018 09:56

FIGURE D.2: Reprinting license Köhler et al. 2006.

Bibliography

[1] Frank J Holly. “Formation and rupture of the tear film”. In: *Experimental eye research* 15.5 (1973), pp. 515–525.

[2] Jacques Emile Proust, Slavka Dorsimova Tchaliovska, and Lisbeth Ter-Minassian-Saraga. “Mucin thin film as a model of the tear film rupture”. In: *Journal of colloid and interface science* 98.2 (1984), pp. 319–328.

[3] Jeremy I Prydal et al. “Study of human precorneal tear film thickness and structure using laser interferometry.” In: *Investigative ophthalmology & visual science* 33.6 (1992), pp. 2006–2011.

[4] Michael R Knowles and Richard C Boucher. “Mucus clearance as a primary innate defense mechanism for mammalian airways”. In: *The Journal of clinical investigation* 109.5 (2002), pp. 571–577.

[5] Ivan Ivanov. *Thin liquid films*. Vol. 29. CRC Press, 1988.

[6] Virginie Soulie et al. “The evaporation behavior of sessile droplets from aqueous saline solutions”. In: *Phys.Chem.Chem.Phys.* 17 (2015), pp. 22296–22303.

[7] Stefan Karpitschka, Ferenc Liebig, and Hans Riegler. “Marangoni Contraction of Evaporating Sessile Droplets of Binary Mixtures”. In: *Langmuir* 33.19 (2017), pp. 4682–4687.

[8] Edward Lansing Cussler. *Diffusion: mass transfer in fluid systems*. Cambridge university press, 2009.

[9] Jacob N Israelachvili, Patricia M McGuiggan, and Andrew M Homola. “Dynamic properties of molecularly thin liquid films”. In: *Science* 240.4849 (1988), pp. 189–191.

[10] Alexander Sidorenko, Tom Krupenkin, and Joanna Aizenberg. “Controlled switching of the wetting behavior of biomimetic surfaces with hydrogel-supported nanostructures”. In: *Journal of Materials Chemistry* 18.32 (2008), pp. 3841–3846.

[11] V Bergeron and CJ Radke. “Equilibrium measurements of oscillatory disjoining pressures in aqueous foam films”. In: *Langmuir* 8.12 (1992), pp. 3020–3026.

[12] Tak-Sing Wong et al. “Bioinspired self-repairing slippery surfaces with pressure-stable omniphobicity”. In: *Nature* 477.7365 (2011), p. 443.

[13] Xi Yao et al. “Adaptive fluid-infused porous films with tunable transparency and wettability”. In: *Nature materials* 12.6 (2013), p. 529.

[14] Stephan Eickelmann and Hans Riegler. “Rupture of ultrathin solution films on planar solid substrates induced by solute crystallization”. In: *Journal of colloid and interface science* 528 (2018), pp. 63–69.

[15] Per Axel Clausen. “Emission of volatile and semivolatile organic compounds from waterborne paints–the effect of the film thickness”. In: *Indoor Air* 3.4 (1993), pp. 269–275.

[16] LE Sparks et al. “Volatile organic compound emissions from latex paint–Part 1. Chamber experiments and source model development”. In: *Indoor Air* 9.1 (1999), pp. 10–17.

[17] Vladislav Dolník, Shaorong Liu, and Stevan Jovanovich. “Capillary electrophoresis on microchip”. In: *ELECTROPHORESIS: An International Journal* 21.1 (2000), pp. 41–54.

[18] PA Hammond and DRS Cumming. “Encapsulation of a liquid-sensing microchip using SU-8 photoresist”. In: *Microelectronic Engineering* 73 (2004), pp. 893–897.

[19] Changchun Liu et al. “A rigid poly (dimethylsiloxane) sandwich electrophoresis microchip based on thin-casting method”. In: *Electrophoresis* 27.14 (2006), pp. 2917–2923.

[20] Kyung-In Jang et al. “Self-assembled three dimensional network designs for soft electronics”. In: *Nature Communications* 8 (2017), p. 15894.

[21] Tohru Mogami. “Challenges for sub-10 nm CMOS devices”. In: *Solid-State and Integrated Circuit Technology, 2006. ICSICT’06. 8th International Conference on*. IEEE. 2006, pp. 23–26.

[22] James H Stathis et al. “Reliability challenges for the 10nm node and beyond”. In: *Electron Devices Meeting (IEDM), 2014 IEEE International*. IEEE. 2014, pp. 20–6.

[23] Regina Luttge. *Nano-and Microfabrication for Industrial and Biomedical Applications*. William Andrew, 2016.

[24] Ronald G. Larson and Timothy J. Rehg. “Spin Coating”. In: *Liquid Film Coating: Scientific principles and their technological implications*. Ed. by Stephan F. Kistler and Peter M. Schweizer. Dordrecht: Springer Netherlands, 1997, pp. 709–734.

[25] A.S.H. Makhlouf. “1 - Current and advanced coating technologies for industrial applications”. In: *Nanocoatings and Ultra-Thin Films*. Ed. by Abdel Salam Hamdy Makhlouf and Ion Tiginyanu. Woodhead Publishing Series in Metals and Surface Engineering. Woodhead Publishing, 2011, pp. 3 –23. ISBN: 978-1-84569-812-6. DOI: `https://doi.org/10.1533/9780857094902.1.3`. URL: `http://www.sciencedirect.com/science/article/pii/B9781845698126500014`.

[26] Nam-Trung Nguyen. “Chapter 4 - Fabrication technologies”. In: *Micromixers (Second Edition)*. Ed. by Nam-Trung Nguyen. Second Edition. Micro and Nano Technologies. Oxford: William Andrew Publishing, 2012, pp. 113 –161. ISBN: 978-1-4377-3520-8. DOI: `https://doi.org/10.1016/B978-1-4377-3520-8.00004-8`. URL: `http://www.sciencedirect.com/science/article/pii/B9781437735208000048`.

[27] Richard Smith, Hiroshi Inomata, and Cor Peters. “Chapter 4 - Historical Background and Applications”. In: *Introduction to Supercritical Fluids*. Ed. by Richard Smith, Hiroshi Inomata, and Cor Peters. Vol. 4. Supercritical Fluid Science and Technology. Elsevier, 2013, pp. 175 –273. DOI: `https://doi.org/10.1016/B978-0-444-52215-3.00004-0`. URL: `http://www.sciencedirect.com/science/article/pii/B9780444522153000040`.

[28] Sami Franssila and Santeri Tuomikoski. “Chapter 20 - MEMS Lithography”. In: *Handbook of Silicon Based MEMS Materials and Technologies (Second Edition)*. Ed. by Markku Tilli et al. Second Edition. Micro and Nano Technologies. Boston: William Andrew Publishing, 2015, pp. 427 –443. ISBN: 978-0-323-29965-7. DOI: `https://doi.org/10.1016/B978-0-323-29965-7.00020-8`. URL: `http://www.sciencedirect.com/science/article/pii/B9780323299657000208`.

[29] Stefan Karpitschka, Constans M Weber, and Hans Riegler. “Spin casting of dilute solutions: Vertical composition profile during hydrodynamic-evaporative film thinning”. In: *Chemical Engineering Science* 129 (2015), pp. 243–248.

[30] Alfred G Emslie, Francis T Bonner, and Leslie G Peck. “Flow of a viscous liquid on a rotating disk”. In: *Journal of Applied Physics* 29.5 (1958), pp. 858–862.

[31] Dietrich Meyerhofer. “Characteristics of resist films produced by spinning”. In: *Journal of Applied Physics* 49.7 (1978), pp. 3993–3997.

[32] José Danglad-Flores, Stephan Eickelmann, and Hans Riegler. “Deposition of polymer films by spin casting: A quantitative analysis”. In: *Chemical Engineering Science* 179 (2018), pp. 257 –264.

[33] José Danglad-Flores et al. “Controlled Deposition of Nano- and Micron-Size Particles by Spin Casting”. In: *Submmited to Langmuir* (2018).

[34] Stephen Ebbens et al. “InSitu Imaging and Height Reconstruction of Phase Separation Processes in Polymer Blends during Spin Coating”. In: (2011).

[35] Stefan Karpitschka et al. “Nonintrusive optical visualization of surface nanobubbles”. In: *Physical review letters* 109.6 (2012), p. 066102.

[36] Daniel TW Toolan and Jonathan R Howse. “Development of in situ studies of spin coated polymer films”. In: *Journal of Materials Chemistry C* 1.4 (2013), pp. 603–616.

[37] Daniel TW Toolan et al. “Direct observation of morphological development during the spin-coating of polystyrene–poly (methyl methacrylate) polymer blends”. In: *Journal of Polymer Science Part B: Polymer Physics* 51.11 (2013), pp. 875–881.

[38] Daniel TW Toolan et al. “On the mechanisms of colloidal self-assembly during spin-coating”. In: *Soft Matter* 10.44 (2014), pp. 8804–8812.

[39] Daniel TW Toolan. “Straightforward technique for in situ imaging of spin-coated thin films”. In: *Optical Engineering* 54.2 (2015), p. 024109.

[40] Hans Riegler and Ralf Köhler. “How pre-melting on surrounding interfaces broadens solid–liquid phase transitions”. In: *Nature physics* 3.12 (2007), pp. 890–894.

[41] R Köhler, Paul Lazar, and H Riegler. “Optical imaging of thin films with molecular depth resolution”. In: *Applied physics letters* 89.24 (2006), p. 241906.

[42] Drew Myers. *Surfaces, interfaces, and colloids: principles and applications*. Vol. 2. Wiley Online Library, 1999.

[43] Arthur W Adamson, Alice Petry Gast, et al. “Physical chemistry of surfaces”. In: (1967).

[44] Stanley Middleman. *Modeling axisymmetric flows: dynamics of films, jets, and drops*. Academic Press, 1995.

[45] Gary F Teletzke, H Ted Davis, and LE Scriven. “Wetting hydrodynamics”. In: *Revue de Physique Appliquee* 23.6 (1988), pp. 989–1007.

[46] BV Derjaguin and NV Churaev. “Structural component of disjoining pressure”. In: *Journal of Colloid and Interface Science* 49.2 (1974), pp. 249–255.

[47] Stanley Middleman. “The effect of induced air-flow on the spin coating of viscous liquids”. In: *Journal of applied physics* 62.6 (1987), pp. 2530–2532.

[48] Hans-Jürgen Butt and Michael Kappl. *Surface and interfacial forces*. John Wiley & Sons, 2018.

[49] PG De Gennes, F Brochard-Wyart, and D Quéré. *Capillarity and Wetting Phenomena, 2004*.

[50] NB Vargaftik, BN Volkov, and LD Voljak. “International tables of the surface tension of water”. In: *Journal of Physical and Chemical Reference Data* 12.3 (1983), pp. 817–820.

[51] F Keith, JH Taylor, and JP Chong. *Heat and mass transfer from a rotating disk*. Tech. rep. DTIC Document, 1958.

[52] RJ Goldstein, EM Sparrow, and DC Jones. “Natural convection mass transfer adjacent to horizontal plates”. In: *International Journal of Heat and Mass Transfer* 16.5 (1973), pp. 1025–1035.

[53] DE Bornside, CW Macosko, and LE Scriven. “Spin coating of a PMMA/chlorobenzene solution”. In: *Journal of the Electrochemical Society* 138.1 (1991), pp. 317–320.

[54] David E Bornside et al. “The effects of gas phase convection on mass transfer in spin coating”. In: *Journal of Applied Physics* 73.2 (1993), pp. 585–600.

[55] N Gregory, John Trevor Stuart, and WS Walker. “On the stability of three-dimensional boundary layers with application to the flow due to a rotating disk”. In: *Phil. Trans. R. Soc. Lond. A* 248.943 (1955), pp. 155–199.

[56] DE Bornside, CW Macosko, and LE Scriven. “Spin coating: One-dimensional model”. In: *Journal of Applied Physics* 66.11 (1989), pp. 5185–5193.

[57] CW Frank et al. “Structure in thin and ultrathin spin-cast polymer films”. In: *Science* 273.5277 (1996), p. 912.

[58] K Norrman, A Ghanbari-Siahkali, and NB Larsen. “6 Studies of spin-coated polymer films”. In: *Annual Reports Section" C"(Physical Chemistry)* 101 (2005), pp. 174–201.

[59] A Acrivos, MJ Shah, and EE Petersen. “On the Flow of a Non-Newtonian Liquid on a Rotating Disk”. In: *Journal of Applied Physics* 31.6 (1960), pp. 963–968.

[60] Sadao Shimoji. “A new analytical model for spin coating process with solvent evaporation”. In: *Japanese journal of applied physics* 26.6A (1987), p. L905.

[61] Samson A Jenekhe. “Effects of solvent mass transfer on flow of polymer solutions on a flat rotating disk”. In: *Industrial and engineering chemistry fundamentals* 23.4 (1984), pp. 425–432.

[62] CJ Lawrence. “The mechanics of spin coating of polymer films”. In: *Physics of Fluids (1958-1988)* 31.10 (1988), pp. 2786–2795.

[63] Bell Hess Flackr Soong. “A mathematical model for spin coating of polymer resists”. In: *Journal of Applied Physics* 56.4 (1984), pp. 1199–1206.

[64] Taku Ohara, Yoichiro Matsumoto, and Hideo Ohashi. “The film formation dynamics in spin coating”. In: *Physics of Fluids A: Fluid Dynamics (1989-1993)* 1.12 (1989), pp. 1949–1959.

[65] CJ Lawrence. “Spin coating with slow evaporation”. In: *Physics of Fluids A: Fluid Dynamics (1989-1993)* 2.3 (1990), pp. 453–456.

[66] B Reisfeld, SG Bankoff, and SH Davis. “The dynamics and stability of thin liquid films during spin coating. I. Films with constant rates of evaporation or absorption”. In: *Journal of applied physics* 70.10 (1991), pp. 5258–5266.

[67] B Reisfeld, SG Bankoff, and SH Davis. “The dynamics and stability of thin liquid films during spin coating. II. Films with unit-order and large Peclet numbers”. In: *Journal of applied physics* 70.10 (1991), pp. 5267–5277.

[68] Sadao Shimoji. “Numerical analysis of the spin-coating process”. In: *Journal of Applied Physics* 66.6 (1989), pp. 2712–2718.

[69] Peter C Sukanek. “Dependence of film thickness on speed in spin coating”. In: *Journal of The Electrochemical Society* 138.6 (1991), pp. 1712–1719.

[70] Dylan E Haas et al. “Effect of solvent evaporation rate on skin formation during spin coating of complex solutions”. In: *Sol-Gel Optics V* 3943 (2000), pp. 280–284.

[71] Tohru Okuzono, Kin'ya Ozawa, and Masao Doi. "Simple model of skin formation caused by solvent evaporation in polymer solutions". In: *Physical review letters* 97.13 (2006), p. 136103.

[72] Ralf Köhler, Paul Lazar, and Hans Riegler. "Optical imaging of thin films with molecular depth resolution". In: *Applied Physics Letters* 89 (2006), p. 241906.

[73] Chenyu Jin. *Theoretical and Experimental Study ofCapillary Effect on Melting*. Potsdam, Germany, 2014.

[74] Augustin Fresnel. *Sur la loi des modifications imprimées à la lumière polarisée par sa réflexion totale dans l'intérieur des corps transparents*. 1823.

[75] Bogdan V Parakhonskiy et al. "Colloidal micro-and nano-particles as templates for polyelectrolyte multilayer capsules". In: *Advances in colloid and interface science* 207 (2014), pp. 253–264.

[76] Nadja C Bigall et al. "Monodisperse platinum nanospheres with adjustable diameters from 10 to 100 nm: synthesis and distinct optical properties". In: *Nano letters* 8.12 (2008), pp. 4588–4592.

[77] G Frens. "Controlled nucleation for the regulation of the particle size in monodisperse gold suspensions". In: *Nature physical science* 241.105 (1973), p. 20.

[78] "Meniscus shape around nanoparticles embedded in molecularly thin liquid films". In: *Langmuir* 34.38 (2018), pp. 11364–11373.

[79] LM Peurrung and DB Graves. "Film thickness profiles over topography in spin coating". In: *Journal of the electrochemical society* 138.7 (1991), pp. 2115–2124.

[80] Paul C Jukes et al. "Time-resolved light scattering studies of phase separation in thin film semiconducting polymer blends during spin-coating". In: *Macromolecules* 38.6 (2005), pp. 2030–2032.

[81] William Henry Bragg, William Lawrence Bragg, et al. "The reflection of X-rays by crystals". In: *Proc. R. Soc. Lond. A* 88.605 (1913), pp. 428–438.

[82] Inc. Filmetrics. *Reflectance Calculator*. 2018. URL: `https://filmetrics.com/reflectance-calculator` (visited on 10/04/2018).

[83] Steven J Byrnes. "Multilayer optical calculations". In: *arXiv preprint arXiv:1603.02720* (2016).

[84] AK Baker and PE Dyer. "Refractive-index modification of polymethylmethacrylate (PMMA) thin films by KrF-laser irradiation". In: *Applied Physics A* 57.6 (1993), pp. 543–544.

[85] Feridun Ay et al. "Prism coupling technique investigation of elasto-optical properties of thin polymer films". In: *Journal of applied physics* 96.12 (2004), pp. 7147–7153.

[86] Caitlin McDowell et al. "Solvent Additives: Key Morphology-Directing Agents for Solution-Processed Organic Solar Cells". In: *Advanced Materials* (2018), p. 1707114.

[87] Jacobus J Van Franeker et al. "A real-time study of the benefits of co-solvents in polymer solar cell processing". In: *Nature communications* 6 (2015), p. 6229.

[88] Wi Hyoung Lee et al. "The Influence of the Solvent Evaporation Rate on the Phase Separation and Electrical Performances of Soluble Acene-Polymer Blend Semiconductors". In: *Advanced Functional Materials* 22.2 (2012), pp. 267–281.

[89] Yan Yao et al. "Effects of solvent mixtures on the nanoscale phase separation in polymer solar cells". In: *Advanced Functional Materials* 18.12 (2008), pp. 1783–1789.

[90] Dean M DeLongchamp et al. “Variations in semiconducting polymer microstructure and hole mobility with spin-coating speed”. In: *Chemistry of materials* 17.23 (2005), pp. 5610–5612.

[91] Kenneth E Strawhecker et al. “The critical role of solvent evaporation on the roughness of spin-cast polymer films”. In: *Macromolecules* 34.14 (2001), pp. 4669–4672.

[92] Y Chang, WC Wu, and WC Chen. “Theoretical analysis on spin coating of polyimide precursor solutions”. In: *Journal of The Electrochemical Society* 148.4 (2001), F77–F81.

[93] Jacobus J van Franeker et al. “Controlling the Dominant Length Scale of Liquid–Liquid Phase Separation in Spin-coated Organic Semiconductor Films”. In: *Advanced Functional Materials* 25.6 (2015), pp. 855–863.

[94] WG Cochran. “The flow due to a rotating disc”. In: *Mathematical Proceedings of the Cambridge Philosophical Society*. Vol. 30. 3. Cambridge University Press. 1934, pp. 365–375.

[95] H Yildirim Erbil and Yonca Avci. “Simultaneous determination of toluene diffusion coefficient in air from thin tube evaporation and sessile drop evaporation on a solid surface”. In: *Langmuir* 18.13 (2002), pp. 5113–5119.

[96] Pierre Gilles De Gennes. “Solvent evaporation of spin cast films:"crust" effects”. In: *The European Physical Journal E: Soft Matter and Biological Physics* 7.1 (2002), pp. 31–34.

[97] RG Picknett and R Bexon. “The Evaporation of Sessile or Pendant Drops in Still Air”. In: *Journal of Colloid and Interface Science* 61.2 (1977), pp. 336–350.

[98] KS Birdi, DT Vu, and A Winter. “A study of the Evaporation Rates of Small Water Drops Placed on a Solid Surface”. In: *The Journal of Physical Chemistry* 93 (1989), pp. 3702–3703.

[99] Chong Meng Kok and Alfred Rudin. “Prediction of Flory–Huggins interaction parameters from intrinsic viscosities”. In: *Journal of applied polymer science* 27.2 (1982), pp. 353–362.

[100] C Mathew Mate and VJ Novotny. “Molecular conformation and disjoining pressure of polymeric liquid films”. In: *The Journal of chemical physics* 94.12 (1991), pp. 8420–8427.

[101] George DJ Phillies. “Hydrodynamic scaling of viscosity and viscoelasticity of polymer solutions, including chain architecture and solvent quality effects”. In: *Macromolecules* 28.24 (1995), pp. 8198–8208.

[102] Beatrice Guerrier et al. “Drying kinetics of polymer films”. In: *AIChE Journal* 44.4 (1998), pp. 791–798.

[103] MORIO OKAZAKI et al. “Drying mechanism of coated film of polymer solution”. In: *Journal of Chemical Engineering of Japan* 7.2 (1974), pp. 99–105.

[104] BD Washo. “Rheology and modeling of the spin coating process”. In: *IBM Journal of Research and Development* 21.2 (1977), pp. 190–198.

[105] JJ Hernandez et al. “Structure and morphology of thin films of linear aliphatic polyesters prepared by spin-coating”. In: *Langmuir* 26.13 (2010), pp. 10731–10737.

[106] A Weill and E Dechenaux. “The spin-coating process mechanism related to polymer solution properties”. In: *Polymer Engineering & Science* 28.15 (1988), pp. 945–948.

[107] Sasha Y Heriot and Richard AL Jones. “An interfacial instability in a transient wetting layer leads to lateral phase separation in thin spin-cast polymer-blend films”. In: *Nature materials* 4.10 (2005), pp. 782–786.

[108] Paul C Jukes et al. “Time-resolved light scattering studies of phase separation in thin film semiconducting polymer blends during spin-coating”. In: *Macromolecules* 38.6 (2005), pp. 2030–2032.

[109] P Mokarian-Tabari et al. “Quantitative evaluation of evaporation rate during spin-coating of polymer blend films: Control of film structure through defined-atmosphere solvent-casting”. In: *The European Physical Journal E* 33.4 (2010), pp. 283–289.

[110] BT Chen. “Investigation of the solvent-evaporation effect on spin coating of thin films”. In: *Polymer Engineering & Science* 23.7 (1983), pp. 399–403.

[111] David B Hall, Patrick Underhill, and John M Torkelson. “Spin coating of thin and ultrathin polymer films”. In: *Polymer Engineering & Science* 38.12 (1998), pp. 2039–2045.

[112] Seth B Darling et al. “Self-Organization of FePt Nanoparticles on Photochemically Modified Diblock Copolymer Templates”. In: *Advanced Materials* 17.20 (2005), pp. 2446–2450.

[113] Jun Sun et al. “Uniform and reproducible plasmon-enhanced fluorescence substrate based on PMMA-coated, large-area Au@ Ag nanorod arrays”. In: *Nano Research* 11.2 (2018), pp. 953–965.

[114] Jamileh Shojaeiarani, Dilpreet S Bajwa, and Nicole M Stark. “Spin-coating: A new approach for improving dispersion of cellulose nanocrystals and mechanical properties of poly (lactic acid) composites”. In: *Carbohydrate polymers* 190 (2018), pp. 139–147.

[115] Sander J Tans et al. “Individual single-wall carbon nanotubes as quantum wires”. In: *Nature* 386.6624 (1997), p. 474.

[116] Aaron C Johnston-Peck, Junwei Wang, and Joseph B Tracy. “Formation and grain analysis of spin-cast magnetic nanoparticle monolayers”. In: *Langmuir* 27.8 (2011), pp. 5040–5046.

[117] Seth Coe-Sullivan et al. “Large-Area Ordered Quantum-Dot Monolayers via Phase Separation During Spin-Casting”. In: *Advanced Functional Materials* 15.7 (2005), pp. 1117–1124.

[118] Peng Jiang et al. “Two-dimensional nonclose-packed colloidal crystals formed by spincoating”. In: *Applied Physics Letters* 89.1 (2006), p. 011908.

[119] Peng Jiang and Michael J McFarland. “Large-scale fabrication of wafer-size colloidal crystals, macroporous polymers and nanocomposites by spin-coating”. In: *Journal of the American Chemical Society* 126.42 (2004), pp. 13778–13786.

[120] Dayang Wang and Helmuth Möhwald. “Rapid fabrication of binary colloidal crystals by stepwise spin-coating”. In: *Advanced Materials* 16.3 (2004), pp. 244–247.

[121] L Ajith DeSilva et al. “Reflectivity of 88% for four-period hybrid Bragg mirror from spin coating process”. In: *Optik-International Journal for Light and Electron Optics* 157 (2018), pp. 360–364.

[122] L. Ajith DeSilva et al. “Synthesis of dense TiO2 nanoparticle multilayers using spin coating technique”. In: *Applied Physics A* 124.4 (2018), p. 314.

[123] Young-Kyu Hong et al. “Controlled two-dimensional distribution of nanoparticles by spin-coating method”. In: *Applied Physics Letters* 80.5 (2002), pp. 844–846.

[124] Robert H Davis and Andreas Acrivos. “Sedimentation of noncolloidal particles at low Reynolds numbers”. In: *Annual Review of Fluid Mechanics* 17.1 (1985), pp. 91–118.

[125] Stefan Tenzer et al. “Rapid formation of plasma protein corona critically affects nanoparticle pathophysiology”. In: *Nature nanotechnology* 8.10 (2013), p. 772.

[126] Fangang Meng et al. "Fouling in membrane bioreactors: an updated review". In: *Water research* 114 (2017), pp. 151–180.

[127] Zhiya Sheng and Yang Liu. "Effects of silver nanoparticles on wastewater biofilms". In: *Water Research* 45.18 (2011), pp. 6039–6050.

[128] Amir H Bahrami et al. "Wrapping of nanoparticles by membranes". In: *Advances in colloid and interface science* 208 (2014), pp. 214–224.

[129] Li Shang, Karin Nienhaus, and Gerd Ulrich Nienhaus. "Engineered nanoparticles interacting with cells: size matters". In: *J Nanobiotechnol* 12.5 (2014), b26.

[130] Wen Jiang et al. "Nanoparticle-mediated cellular response is size-dependent". In: *Nature nanotechnology* 3.3 (2008), p. 145.

[131] Ralph Weissleder, Matthias Nahrendorf, and Mikael J Pittet. "Imaging macrophages with nanoparticles". In: *Nature materials* 13.2 (2014), p. 125.

[132] Rachelle M Choueiri et al. "Surface patterning of nanoparticles with polymer patches". In: *Nature* 538.7623 (2016), p. 79.

[133] Anna C Balazs, Todd Emrick, and Thomas P Russell. "Nanoparticle polymer composites: where two small worlds meet". In: *Science* 314.5802 (2006), pp. 1107–1110.

[134] Terry P Bigioni et al. "Kinetically driven self assembly of highly ordered nanoparticle monolayers". In: *Nature materials* 5.4 (2006), p. 265.

[135] Marek Grzelczak et al. "Directed self-assembly of nanoparticles". In: *ACS nano* 4.7 (2010), pp. 3591–3605.

[136] Peter J Yunker et al. "Suppression of the coffee-ring effect by shape-dependent capillary interactions". In: *Nature* 476.7360 (2011), p. 308.

[137] PH Lizotte et al. "In situ vaccination with cowpea mosaic virus nanoparticles suppresses metastatic cancer". In: *Nature nanotechnology* 11.3 (2016), p. 295.

[138] Mohammad J Hajipour et al. "Antibacterial properties of nanoparticles". In: *Trends in biotechnology* 30.10 (2012), pp. 499–511.

[139] Michael R Yeaman. "Platelets in defense against bacterial pathogens". In: *Cellular and molecular life sciences* 67.4 (2010), pp. 525–544.

[140] Juan Peng et al. "Formation of regular hole pattern in polymer films". In: *Macromolecular Chemistry and Physics* 204.1 (2003), pp. 125–130.

[141] Deuk Ju Kim, Min Jae Jo, and Sang Yong Nam. "A review of polymer–nanocomposite electrolyte membranes for fuel cell application". In: *Journal of Industrial and Engineering Chemistry* 21 (2015), pp. 36–52.

[142] P. A. Kralchevsky et al. "Capillary Meniscus Interaction between Colloidal Particles Attachewd to a Liquid-Fluid INterface". In: *Journal of Colloid and lnterface Science* 151.1 (1992), p. 79.

[143] Peter A Kralchevsky and Kuniaki Nagayamaa. "Capillary interactions between particles bound to interfaces, liquid films and biomembranes". In: *Advances in Colloid and Interface Science* 85 (2000), pp. 145–192.

[144] Jennifer Fiegel et al. "Wetting of a particle in a thin film". In: *Journal of Colloid and Interface Science* 291.2 (2005), pp. 507–514.

[145] Martin Tress et al. "Shape of a sessile drop on a flat surface covered with a liquid film". In: *Soft matter* 13.20 (2017), pp. 3760–3767.

[146] Yahachi Saito. "Q Nanoparticles and Nanocapsules". In: *Carbon Nanotubes: Preparation and Properties* (1996), p. 249.

[147] Jiwen Zheng et al. "Nanopatterned assembling of colloidal gold nanoparticles on silicon". In: *Langmuir* 16.10 (2000), pp. 4409–4412.

[148] Rongchao Jin, Justin E Jureller, and Norbert F Scherer. "Precise localization and correlation of single nanoparticle optical responses and morphology". In: *Applied physics letters* 88.26 (2006), p. 263111.

[149] Luca Costa et al. "Real Space Imaging of Nanoparticle Assembly at Liquid–Liquid Interfaces with Nanoscale Resolution". In: *Nano Letters* 16.9 (2016), pp. 5463–5468.

[150] Yugang Sun and Younan Xia. "Shape-controlled synthesis of gold and silver nanoparticles". In: *Science* 298.5601 (2002), pp. 2176–2179.

[151] Maria Dienerowitz, Michael Mazilu, and Kishan Dholakia. "Optical manipulation of nanoparticles: a review". In: *Journal of Nanophotonics* 2.1 (2008), pp. 021875–021875.

[152] Li Li et al. "Single nanoparticle-based heteronanojunction as a plasmon ruler for measuring dielectric thin films". In: *The journal of physical chemistry letters* 6.12 (2015), pp. 2282–2286.

[153] Qingshan Wei et al. "Fluorescent imaging of single nanoparticles and viruses on a smart phone". In: *ACS nano* 7.10 (2013), p. 9147.

[154] GG Daaboul et al. "High-throughput detection and sizing of individual low-index nanoparticles and viruses for pathogen identification". In: *Nano letters* 10.11 (2010), pp. 4727–4731.

[155] Steven M Scherr et al. "Real-time capture and visualization of individual viruses in complex media". In: *ACS nano* 10.2 (2016), p. 2827.

[156] Weihua Zhang et al. "Trapping and sensing 10 nm metal nanoparticles using plasmonic dipole antennas". In: *Nano letters* 10.3 (2010), pp. 1006–1011.

[157] Yue Liu and Cheng Zhi Huang. "Real-time dark-field scattering microscopic monitoring of the in situ growth of single Ag@ Hg nanoalloys". In: *ACS nano* 7.12 (2013), pp. 11026–11034.

[158] Lord Rayleigh. "XX. On the equilibrium of liquid conducting masses charged with electricity". In: *The London, Edinburgh, and Dublin Philosophical Magazine and Journal of Science* 14.87 (1882), pp. 184–186.

[159] Yves Hennequin et al. "Optical Detection and Sizing of Single Nanoparticles Using Continuous Wetting Films". In: *ACS Nano* 7 (2013), 7601—7609.

[160] Eann A Patterson and Maurice P Whelan. "Optical signatures of small nanoparticles in a conventional microscope". In: *Small* 4.10 (2008), pp. 1703–1706.

[161] Eann A Patterson and Maurice P Whelan. "Tracking nanoparticles in an optical microscope using caustics". In: *Nanotechnology* 19.10 (2008), p. 105502.

[162] J-M GINESTE et al. "Three-dimensional automated nanoparticle tracking using Mie scattering in an optical microscope". In: *Journal of microscopy* 243.2 (2011), pp. 172–178.

[163] Ravikiran Attota et al. "Nanoparticle size determination using optical microscopes". In: *Applied Physics Letters* 105.16 (2014), p. 163105.

[164] Onur Mudanyali et al. "Wide-field optical detection of nanoparticles using on-chip microscopy and self-assembled nanolenses". In: *Nature photonics* 7.3 (2013), nphoton–2012.

[165] Guoxiang Chen et al. "Capillary-Enhanced Immobilization of Nanoparticles". In: *The Journal of Physical Chemistry Letters* 8.24 (2017), pp. 6094–6098.

[166] Tomoya Taguchi, Katsuhiro Isozaki, and Kazushi Miki. "Enhanced catalytic activity of self-assembled-monolayer-capped gold nanoparticles". In: *Advanced Materials* 24.48 (2012), pp. 6462–6467.

[167] Meikun Fan, Gustavo FS Andrade, and Alexandre G Brolo. "A review on the fabrication of substrates for surface enhanced Raman spectroscopy and their applications in analytical chemistry". In: *Analytica chimica acta* 693.1-2 (2011), pp. 7–25.

[168] Qun Fu et al. "Highly reproducible and sensitive SERS substrates with Ag inter-nanoparticle gaps of 5 nm fabricated by ultrathin aluminum mask technique". In: *ACS applied materials & interfaces* 7.24 (2015), pp. 13322–13328.

[169] Michael Riskin et al. "Ultrasensitive surface plasmon resonance detection of trinitrotoluene by a bis-aniline-cross-linked Au nanoparticles composite". In: *Journal of the American Chemical Society* 131.21 (2009), pp. 7368–7378.

[170] Royce W Murray. "Nanoelectrochemistry: metal nanoparticles, nanoelectrodes, and nanopores". In: *Chemical reviews* 108.7 (2008), pp. 2688–2720.

[171] Antoine Moreau et al. "Controlled-reflectance surfaces with film-coupled colloidal nanoantennas". In: *Nature* 492.7427 (2012), p. 86.

[172] Jiwoong Yang et al. "Designed assembly and integration of colloidal nanocrystals for device applications". In: *Advanced Materials* 28.6 (2016), pp. 1176–1207.

[173] Cherie R Kagan et al. "Building devices from colloidal quantum dots". In: *Science* 353.6302 (2016), aac5523.

[174] Binbin Jin and Junhui He. "Self-Templated Fabrication of Robust Moth-Eye-Like Nanostructures with Broadband and Quasi-Omnidirectional Antireflection Properties". In: *ACS Photonics* 4.1 (2016), pp. 188–196.

[175] Tanya Karakouz et al. "Stabilization of gold nanoparticle films on glass by thermal embedding". In: *ACS applied materials & interfaces* 3.4 (2011), pp. 978–987.

[176] Troy D Gould et al. "Stabilizing Ni catalysts by molecular layer deposition for harsh, dry reforming conditions". In: *Acs Catalysis* 4.8 (2014), pp. 2714–2717.

[177] Brandon J O'Neill et al. "Catalyst design with atomic layer deposition". In: *Acs Catalysis* 5.3 (2015), pp. 1804–1825.

[178] Yu Liu, Valery N Khabashesku, and Naomi J Halas. "Fluorinated nanodiamond as a wet chemistry precursor for diamond coatings covalently bonded to glass surface". In: *Journal of the American Chemical Society* 127.11 (2005), pp. 3712–3713.

[179] Myoung-Hwan Park et al. "Nanoparticle immobilization on surfaces via activatable heterobifunctional dithiocarbamate bond formation". In: *Advanced Materials* 20.21 (2008), pp. 4185–4188.

[180] Yun Xia et al. "Immobilization of recombinant vault nanoparticles on solid substrates". In: *ACS nano* 4.3 (2010), pp. 1417–1424.

[181] Christian Pick et al. "Micropatterned charge heterogeneities via vapor deposition of aminosilanes". In: *Langmuir* 31.39 (2015), pp. 10725–10733.

[182] Stefan Karpitschka et al. "Coalescence and noncoalescence of sessile drops: impact of surface forces". In: *Langmuir* 30.23 (2014), pp. 6826–6830.

[183] Sophie E Williams et al. "Controlling the nanoscale patterning of AuNPs on silicon surfaces". In: *Nanomaterials* 3.1 (2013), pp. 192–203.

[184] John K Berg, Constans M Weber, and Hans Riegler. "Impact of negative line tension on the shape of nanometer-size sessile droplets". In: *Physical review letters* 105.7 (2010), p. 076103.

[185] Rodrigo Perez-Garcia and Hans Riegler. “Controlled Self-Organized Positioning of Small Aggregates by Patterns of (Sub) nanosized Active Sites”. In: *Crystal Growth & Design* 17.4 (2017), pp. 1870–1875.

[186] Hans-Jürgen Butt and Michael Kappl. “Normal capillary forces”. In: *Advances in colloid and interface science* 146.1-2 (2009), pp. 48–60.

[187] A Blanco, F Gallego-Gómez, and C López. “Nanoscale morphology of water in silica colloidal crystals”. In: *The journal of physical chemistry letters* 4.7 (2013), pp. 1136–1142.

[188] Sung-Soo Yoon and Dahl-Young Khang. “Room-temperature chemical welding and sintering of metallic nanostructures by capillary condensation”. In: *Nano letters* 16.6 (2016), pp. 3550–3556.

[189] Ian Smallwood. *Handbook of organic solvent properties*. Butterworth-Heinemann, 2012.

[190] Richard M Felder, Ronald W Rousseau, and Lisa G Bullard. *Elementary Principles of Chemical Processes*. Wiley Global Education, 2015.

[191] Thomas Raphael Marrero and Edward Allen Mason. “Gaseous diffusion coefficients”. In: *Journal of Physical and Chemical Reference Data* 1.1 (1972), pp. 3–118.

[192] GA Lugg. “Diffusion coefficients of some organic and other vapors in air”. In: *Analytical Chemistry* 40.7 (1968), pp. 1072–1077.

[193] Warren J Lyman, William F Reehl, and David Hirsch Rosenblatt. “Handbook of chemical property estimation methods: environmental behavior of organic compounds”. In: (1990).

[194] Julio L Bueno et al. “Binary gaseous diffusion coefficients. Air with furan derivatives”. In: *Journal of Chemical and Engineering Data* 25.1 (1980), pp. 27–28.

[195] AN Berezhnoi and AV Semenov. *Binary diffusion coefficients of liquid vapors in gases*. Begell House New York, 1997.

Declaration of Authorship

The content of this thesis has be partially published and it is based on the following publications:

- **Chapter 5: Deposition of Molecules from and Evaporative Thin Film**
  José Danglad-Flores, Stephan Eickelmann, and Hans Riegler. "Deposition of polymer films by spin casting: A quantitative analysis". In: *Chemical Engineering Science* 179 (2018), pp. 257 –264.
  Authorship statement: This publication is the result of my own work in collaboration with Stephan Eickelmann, and the support of Dr. Hans Riegler.

- **Chapter 6: Deposition of Particles from and Evaporative Thin Film**
  Controlled Deposition of Nano- and Micron-Size Particles by Spin Casting. J. Danglad-Flores, K. Eftekhari, A. Skirtach, and R. Riegler, Submitted to: Langmuir
  Authorship statement: This publication is the result of my own work in collaboration with Karaneh Eftekhari, Dr. Andre Skirtach and the support of Dr. Hans Riegler.

- **Chapter 7: Liquid Thin Film Shape Around Nanoparticles**
  "Meniscus shape around nanoparticles embedded in molecularly thin liquid films". In: *Langmuir* 34.38 (2018), pp. 11364–11373.
  Authorship statement: Stephan Eickelmann, José Danglad-Flores, Guoxiang Chen share the first authorship, We worked in collaboration with Dr. Markus Miettinen and the support of Dr. Hans Riegler.

- **Chapter 8: Liquid Thin Film Shape Around Nanoparticles**
  Guoxiang Chen, Rodrigo Perez-Garcia, José Danglad-Flores, and Hans Riegler. "Capillary-Enhanced Immobilization of Nanoparticles". In: *The Journal of Physical Chemistry Letters* 8.24 (2017), pp. 6094–6098.
  Authorship statement: My contributions focused on the polymer particle experiment and nano particles manipulation by AFM.

The author hereby declares, that he completed this work without assistance from any third party and without using other references, sources or aids than the cited ones. The author certifies that this thesis has not been submitted in the same or similar form to any other examination office and has not been accepted as an examination part. The author herewith confirms that he possesses the copyright rights to all parts of the scientific work, and that the publication will not violate the rights of third parties, in particular any copyright and personal rights of third parties.

Signed:

Date: